

AD_____

Award Number: W81XWH-05-1-0280

TITLE: Design, Implementation, and Characterization of a Dedicated Breast Computed Mammo Tomography System for Enhanced Lesion Imaging

PRINCIPAL INVESTIGATOR: Randolph L. McKinley, Ph.D.

CONTRACTING ORGANIZATION: Duke University
Durham NC 27710

REPORT DATE: March 2007

TYPE OF REPORT: Annual Summary

PREPARED FOR: U.S. Army Medical Research and Materiel Command
Fort Detrick, Maryland 21702-5012

DISTRIBUTION STATEMENT: Approved for Public Release;
Distribution Unlimited

The views, opinions and/or findings contained in this report are those of the author(s) and should not be construed as an official Department of the Army position, policy or decision unless so designated by other documentation.

REPORT DOCUMENTATION PAGE				Form Approved OMB No. 0704-0188	
Public reporting burden for this collection of information is estimated to average 1 hour per response, including the time for reviewing instructions, searching existing data sources, gathering and maintaining the data needed, and completing and reviewing this collection of information. Send comments regarding this burden estimate or any other aspect of this collection of information, including suggestions for reducing this burden to Department of Defense, Washington Headquarters Services, Directorate for Information Operations and Reports (0704-0188), 1215 Jefferson Davis Highway, Suite 1204, Arlington, VA 22202-4302. Respondents should be aware that notwithstanding any other provision of law, no person shall be subject to any penalty for failing to comply with a collection of information if it does not display a currently valid OMB control number. PLEASE DO NOT RETURN YOUR FORM TO THE ABOVE ADDRESS.					
1. REPORT DATE (DD-MM-YYYY) 01-03-2007		2. REPORT TYPE Annual Summary		3. DATES COVERED (From - To) 01 Mar 06 – 28 Feb 07	
4. TITLE AND SUBTITLE Design, Implementation, and Characterization of a Dedicated Breast Computed Mammo Tomography System for Enhanced Lesion Imaging				5a. CONTRACT NUMBER	
				5b. GRANT NUMBER W81XWH-05-1-0280	
				5c. PROGRAM ELEMENT NUMBER	
6. AUTHOR(S) Randolph L. McKinley, Ph.D. E-Mail: rlm15@duke.edu				5d. PROJECT NUMBER	
				5e. TASK NUMBER	
				5f. WORK UNIT NUMBER	
7. PERFORMING ORGANIZATION NAME(S) AND ADDRESS(ES) Duke University Durham NC 27710				8. PERFORMING ORGANIZATION REPORT NUMBER	
9. SPONSORING / MONITORING AGENCY NAME(S) AND ADDRESS(ES) U.S. Army Medical Research and Materiel Command Fort Detrick, Maryland 21702-5012				10. SPONSOR/MONITOR'S ACRONYM(S)	
				11. SPONSOR/MONITOR'S REPORT NUMBER(S)	
12. DISTRIBUTION / AVAILABILITY STATEMENT Approved for Public Release; Distribution Unlimited					
13. SUPPLEMENTARY NOTES					
14. ABSTRACT: The overall goal of this work is to design, implement, and characterize a novel dedicated mammotomography system for enhanced lesion detection. This novel system will allow fully 3-D imaging of a pendant, uncompressed breast using novel 3-D complex orbit capabilities. The system has been characterized in terms of dose efficiency and contrast sensitivity indicating the potential for sub-dual-view-dose imaging. The 2D and 3D MTFs have been determined. Observer studies have been performed to determine the lower limits of detectability and a comparison with dual view mammography indicates mammotomography can detect significantly smaller lesions in the presence of overlying structure. Patient bed optimization has also been investigated and a prototype patient bed designed and tilt angles evaluated for optimization of chest wall imaging and patient comfort. Future studies for the remaining phase (Year 3) of project will focus on feasibility of vertical patient bed motion, and evaluation of breast sizes.					
15. SUBJECT TERMS Dedicated Tomographic Breast Imaging, X-Ray Imaging, Computed Tomography					
16. SECURITY CLASSIFICATION OF:			17. LIMITATION OF ABSTRACT	18. NUMBER OF PAGES	19a. NAME OF RESPONSIBLE PERSON
a. REPORT	b. ABSTRACT	c. THIS PAGE			USAMRMC
U	U	U	UU	96	19b. TELEPHONE NUMBER (include area code)

Table of Contents

Cover.....	1
SF298	2
Table of Contents.....	3
Introduction.....	4
Body	4
Key Research Accomplishments	12
Reportable Outcomes.....	12
Conclusions.....	13
References.....	15
Appendices.....	17
Appendix A.....	18
Appendix B	19
Appendix C	30
Appendix D.....	39
Appendix E	50
Appendix F	61
Appendix G.....	74
Appendix H.....	85

Introduction

In the USA, breast cancer in women is one of the leading causes of malignancy and the second leading cause of death due to cancer (after lung cancer); in addition, from 2000 – 2004, its incidence rose at about 4% per year.¹ Thus, early detection of a primary cancer is of paramount importance, because treatment of a small tumor allows for more limited surgery with breast conservation and significantly reduces morbidity and mortality. Limitations in mammography have led to the progressive emergence of complementary imaging techniques. The dedicated breast Computed mammoTomography (CmT) solution we are proposing²⁻¹⁰ has several potential benefits, including: (1) improved detection and characterization of breast lesions, especially in radiographically dense breasts,^{2,11-13} through the removal of contrast-reducing overlying tissue; (2) *uncompressed* breast imaging for greater patient comfort with an associated potential increase in participation rates; (3) breast dose equal to or less than that of current dual view mammography with anticipated increased image contrast; and (4) expectedly improved positive predictive value, especially for radiographically dense breasts. The main goal of this work is to design, develop, implement, and characterize a novel, dedicated computed mammotomography system using cone-beam imaging geometry, having novel degrees of freedom of movement with a unique offset geometry, and using iterative reconstruction techniques. It is hoped that this research and development will lead to *in vivo* tissue differentiation resulting in an improvement in the detection and diagnosis of breast cancer.

Body

Task 2 was comprised of 3 parts and was originally scheduled to fill year 2. This key task had the overall goal of design and evaluation of unique acquisition geometries. Subtasks (a) and (c) have been completed. Subtask (b) was deferred to year 3 and other year 3 items were advanced to and completed in year 2. It should be noted that several of the studies completed for this proposal were done in conjunction with other junior members of the Multi-Modality Imaging Laboratory, some of whom became first authors on the appropriate conference proceeding. This was done for two reasons: (1) to give more junior members an opportunity to share in the studies as a learning experience as well as provide the opportunity to the author to practice skills in guiding junior members of the lab, and (2) the author focused on a September dissertation which was successfully completed and so some delegation was necessary to stay on schedule. Specific sub-task details and progress are provided below.

Task 2(a). The first key subtask was specifically to investigate unique 3D cone-beam orientations and tilt angles for optimal orientation relative to the longitudinally oriented patient chest wall. The current iteration of our system has the digital detector and X-ray mounted on a computer controlled goniometer (model BGM200PE, *Newport Corp.*) and rotation stage (model RV350, *Newport Corp.*, Irvine, CA) to allow polar and azimuthal movements.¹⁴⁻¹⁶ The system is fully automated after having implemented computer controlled synchronization between rotation stage motor, gantry motor, anode rotor, X-ray generator, and detector controller (Figure.1). The band within which the gantry can swing is illustrated in Figure.2.

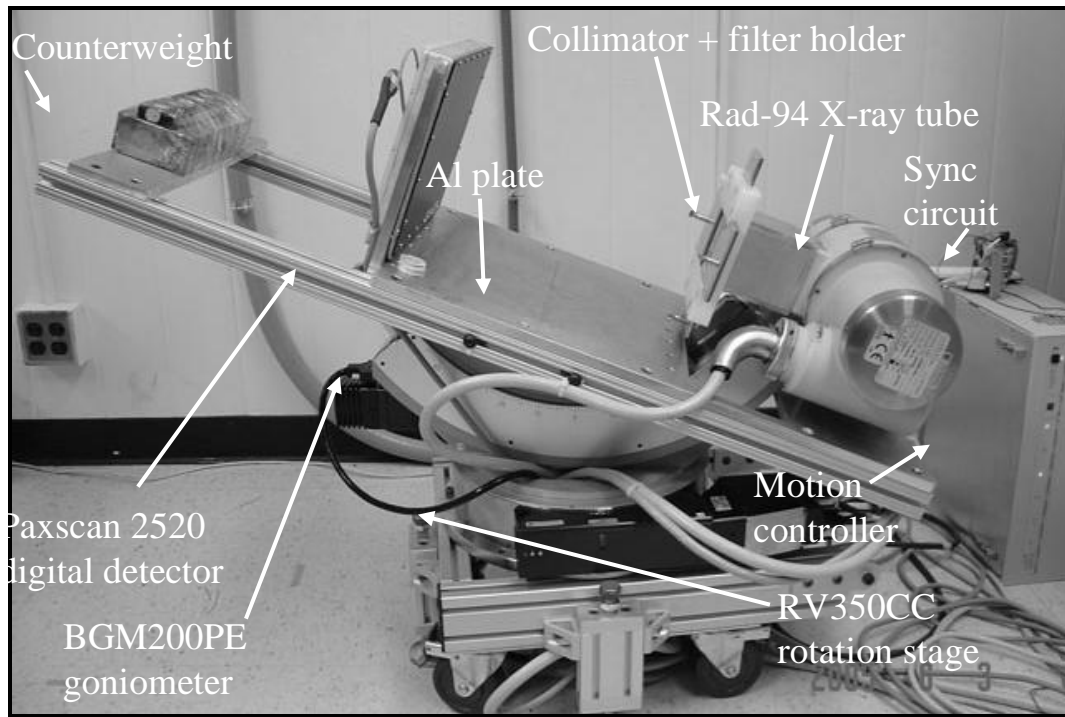


Figure.1 System setup denoting components that have been integrated in a functioning prototype. Components include the BGM200PE goniometer and RV350CC rotation stage, the Varian Rad-94 tungsten X-ray tube and Varian Paxscan 2520 digital X-ray detector, the Al mounting plate, and the synchronization circuit.

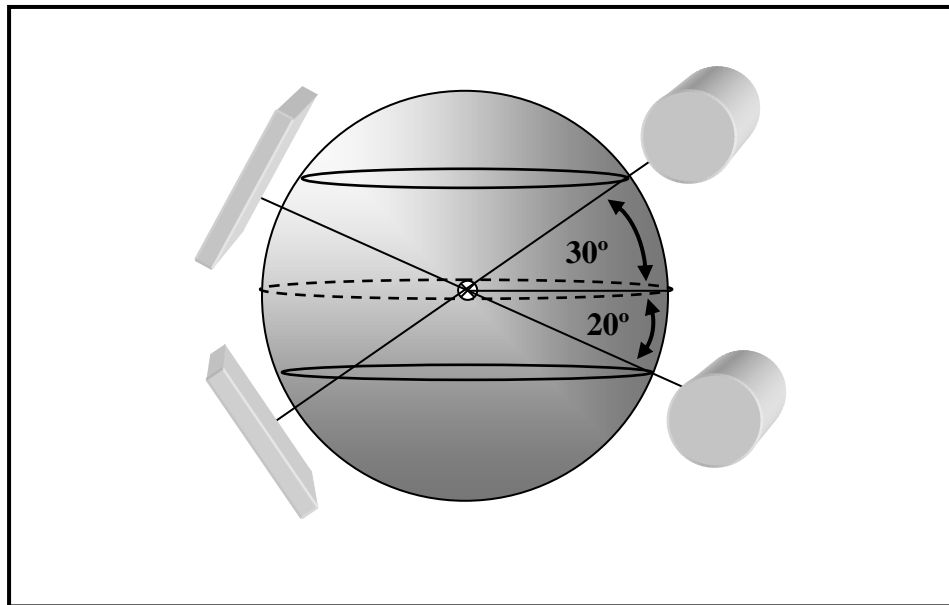


Figure.2 Schematic illustrating band within which arbitrary and complex orbits can be acquired with the gantry. The tube down limit is imposed when the tube cathode and anode plug ports impinge upon the goniometer cradle. The tube up limit is imposed when the top of the detector touches the inside of the goniometer cradle.

Associated with the development of a new bed design (see Specific Aim 1c), it became apparent that a fixed tilt CmT system was required and therefore it became necessary to investigate trade-offs

associated with fixed tilts as well as optimal fixed tilts for maximal chest wall inclusion. Details of the study are provided in Appendix F.

Task 1(c). The next sub-task was to modify patient bed materials and breast opening size as well as bed contour to maximize curvature (and comfort) of patient chest for full volumetric sampling, including chest wall. Using computer-aided design as an initial approach, several geometrical parameters were altered (Figure.3) to determine an optimal design for overcoming geometrical limitations of the detector and tube we were working with.

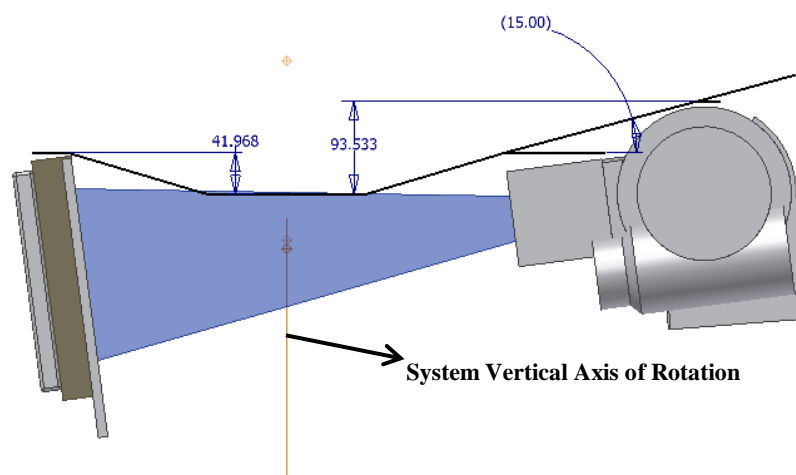


Figure.3 CAD modeled bed design of a 60cm SID and a 15° bed angle. Superimposed on the schematic is the outline of the bed, tailored to allow the source (at left) and detector (at right) to rotate about the noted vertical axis of rotation.

The optimal design was determined to have a 60cm SID, magnification factor of ~1.5, and patient bed angled at ~15° relative to horizontal (Figure.4). Full details of the study can be found in Appendix E. Once the bed design optimization was completed, a prototype bed was constructed (Figure.5).

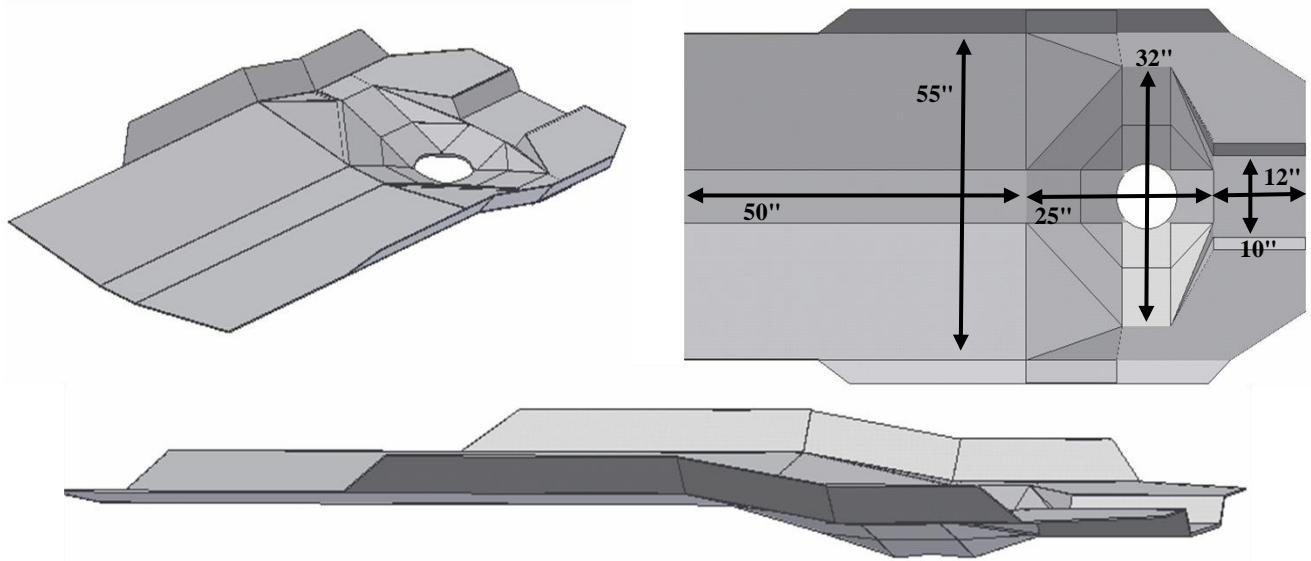


Figure.4 CAD model images of the designed bed from a (TOP LEFT) superior caudal oblique, (TOP RIGHT) superior, and (BOTTOM) lateral oblique perspectives. Notable is the angled octagon in the torso center, and the extended side panels. The bed is close to 55” wide, accommodating a wide variety of patient body types.

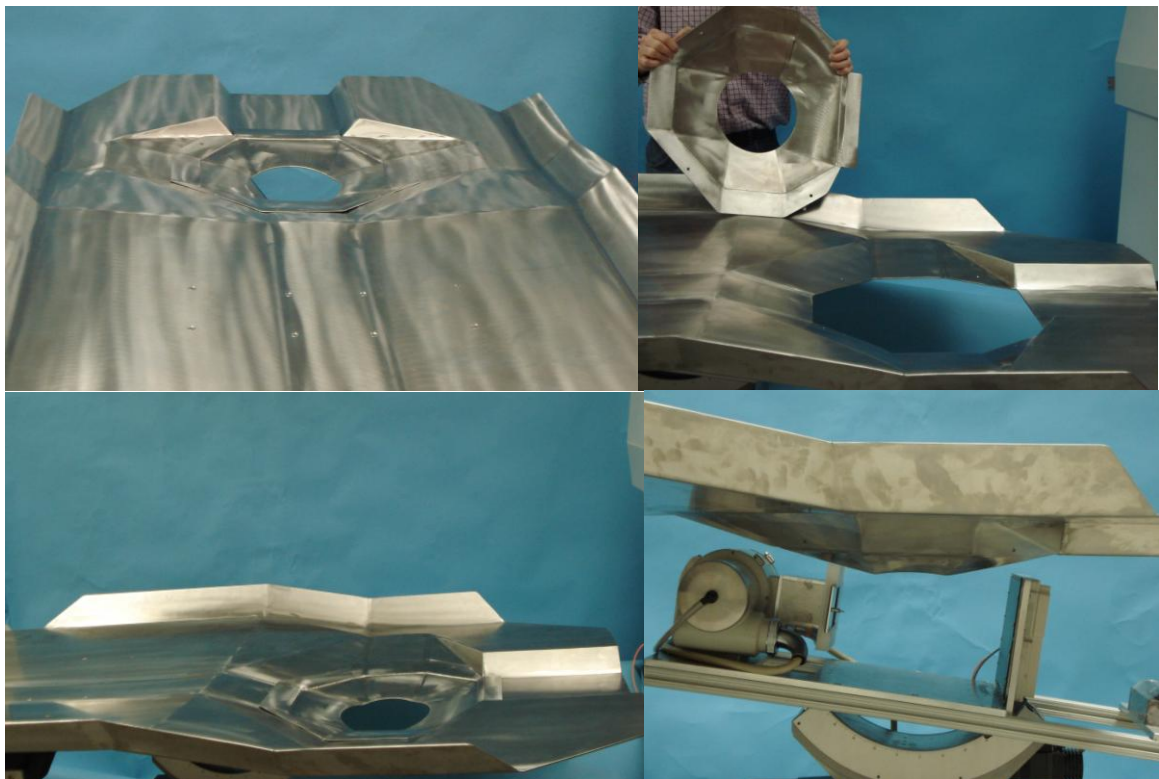


Figure.5 Photographs of the manufactured stainless steel bed from various perspectives. The multi-faceted nature of the bed is readily observed. Note also the (TOP, RIGHT) removable insert that can be replaced by a radiolucent material.

Task 3 was originally scheduled to fill year 3 but has been moved to year 2 in place of sub-task 2(b). Year 3 will be comprised of completing 2(b) as well as additional work on 3(a) and 3(b) which were partially completed in Year 2 (see details below). This key task had the overall goal of evaluating various breast sizes, compositions, lesion sizes, microcalcifications. Subtask 3(c) was already completed in Year 1 and included in that update report. Subtasks (a) and (b) have been approximately 70% completed. Specific subtask details and progress are provided below.

Task 3(a). This subtask was to evaluate different breast sizes, compositions, lesion sizes, microcalcifications to determine upper and lower detection limits as well as effect on breast volume sampling. An observer study was carried out to evaluate the detection limits for various lesion sizes and breast compositions and, in addition, a comparison was done between the CmT system performance and a commercial FFDM system. CmT was shown to significantly outperform FFDM in detection tasks where overlying structure was present (Figure.6).

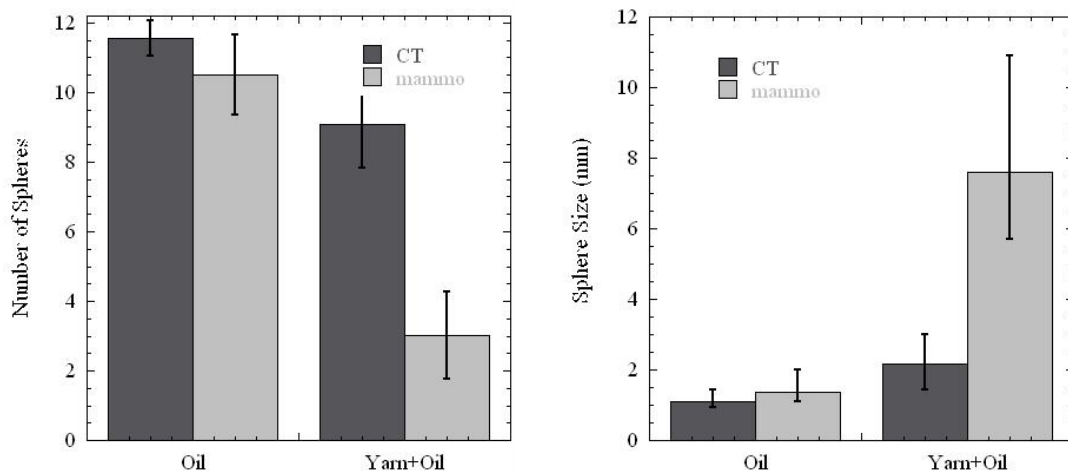


Figure.6 Results for observer studies indicating mean and standard deviation for (left) number of spheres detected and (right) sphere size detected for CmT and FFDM for (from left to right in each plot) oil only, and oil/yarn. Statistically significant differences between means were determined with a Student t-test for $p < 0.05$, and significantly different results were found in all cases.

The median smallest detectable spheres for oil only (high contrast with no overlying structure representing a breast with high adipose content) was 1.0mm and for water background with overlying yarn structure (representing the most difficult detection task with a low contrast lesion in a very dense breast) was 4.0mm. Details of the study are provided in Appendix B. Breast sizes and microcalcifications have yet to be evaluated and will be scheduled for Year 3.

Chest wall proximity evaluation was performed beginning with development of a phantom for this purpose (Figure.7).

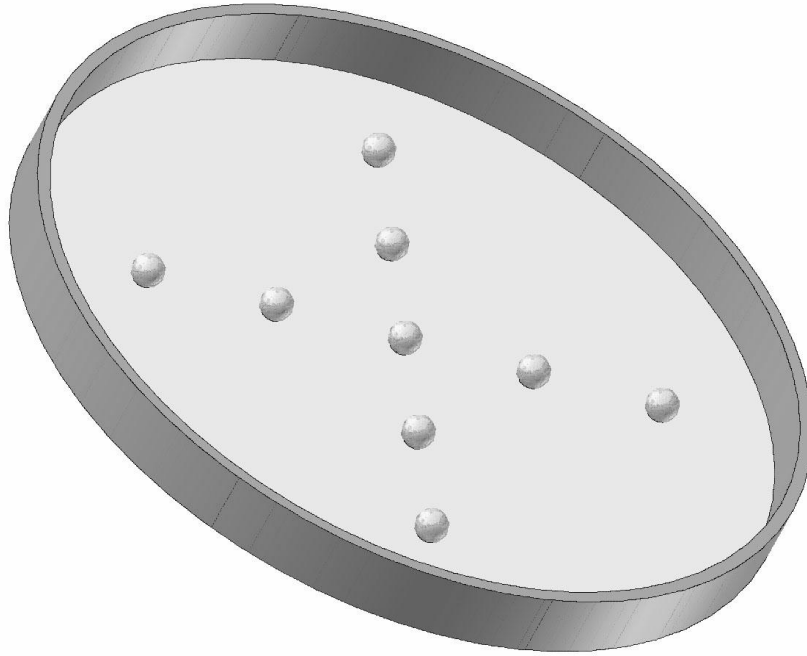


Figure.7 Schematic of cross phantom with 5mm acrylic spheres arranged in a cross pattern and glued to the surface of a thin plastic sheet. This sheet is then glue to a wooden frame. Spheres are placed approximately 2cm apart and a total of 9 spheres are placed on the sheet (graphic is courtesy of Priti Madhav).

Cross phantom studies showed that lesion information may be obtained in areas otherwise outside of the FOV (Figure.8), although imaged quality, in terms of SNR and distortion, is significantly affected. Details of this study can be found in Appendix C Dissertation Excerpt 1.

Task 3(b). This sub-task was to evaluate system and acquisition methodologies for effects on image quality including signal to noise ratio, dose efficiency, contrast sensitivity, resolution metrics (2D and 3D MTF, NPS, DQE), artifacts, and attenuation coefficient (quantitation) accuracy. Several pieces of this sub-task have been included in the results for other sub-tasks. We have measured the NPS and MTF of our current device, and the resulting DQE was determined at calibrated exposures to be 75% and 28% at 0.15 and 2.5 cycles/mm, respectively. These DQE values were measured with our quasi-monochromatic x-ray energy spectrum and are similar to others' previous measurements of similar *Varian* devices. A phantom was developed specifically for the measurement of 3D MTF, NPS, and resulting DQE (Figure.9).

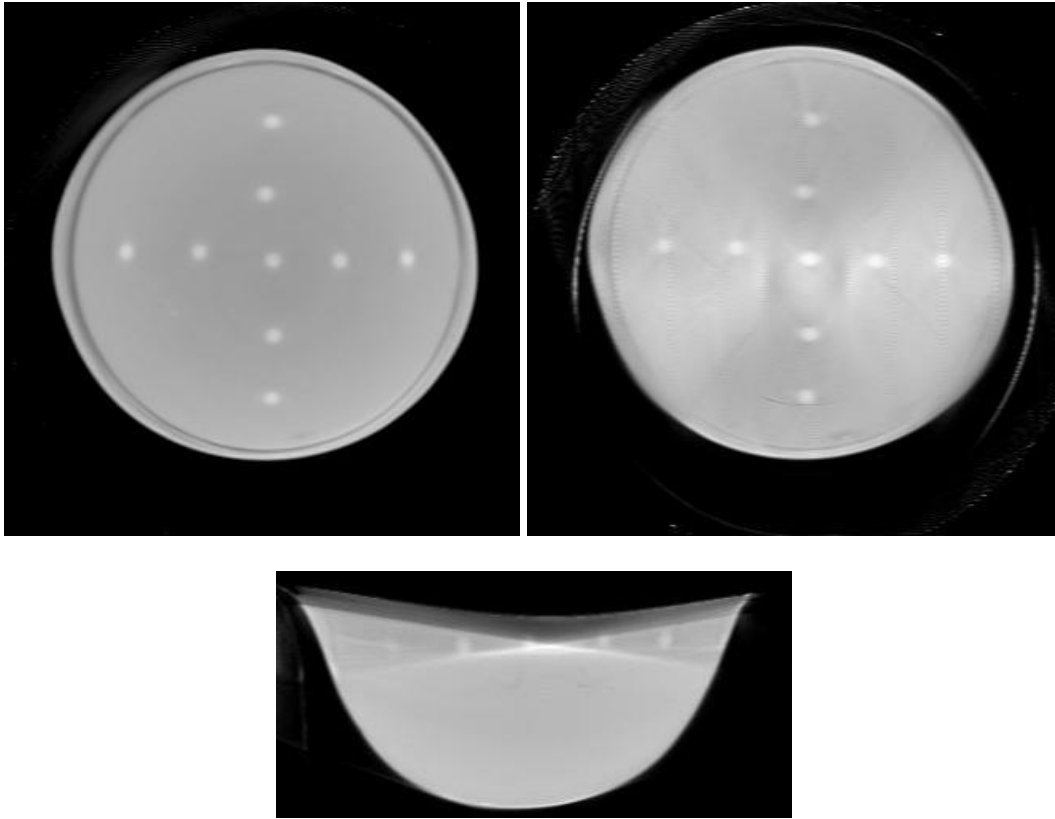


Figure.8 (top row) Coronal views of acrylic cross phantom in oil (10 iterations, 8 subsets, 4x4 binned projections) acquired with (top left) VAOR orbit and spheres fully within field of view, and (top right) Saddle orbit where spheres were not in field of view when system was horizontal without tilt. (bottom) Sagittal view for Saddle orbit indicates additional volume sampled and visibility of spheres even though they were out of FOV initially without tilt.

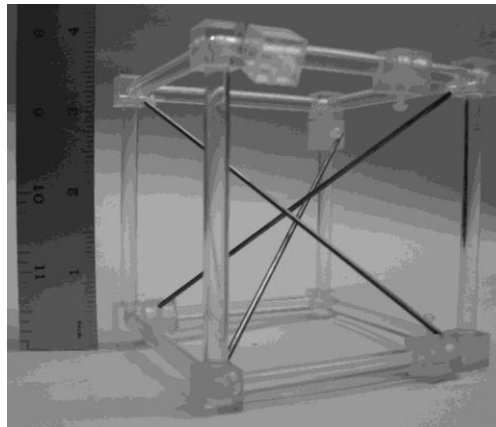


Figure.9: Photograph of acrylic phantom frame with three brass rods used in place of tungsten wires to clearly illustrate the positions of each cord. Cords are visibly separable in their positions such that they do not touch each other near the center.

The 3D MTF was measured for a variety of simple and complex orbits (Figure.10). Various reconstruction parameters and media were also evaluated.

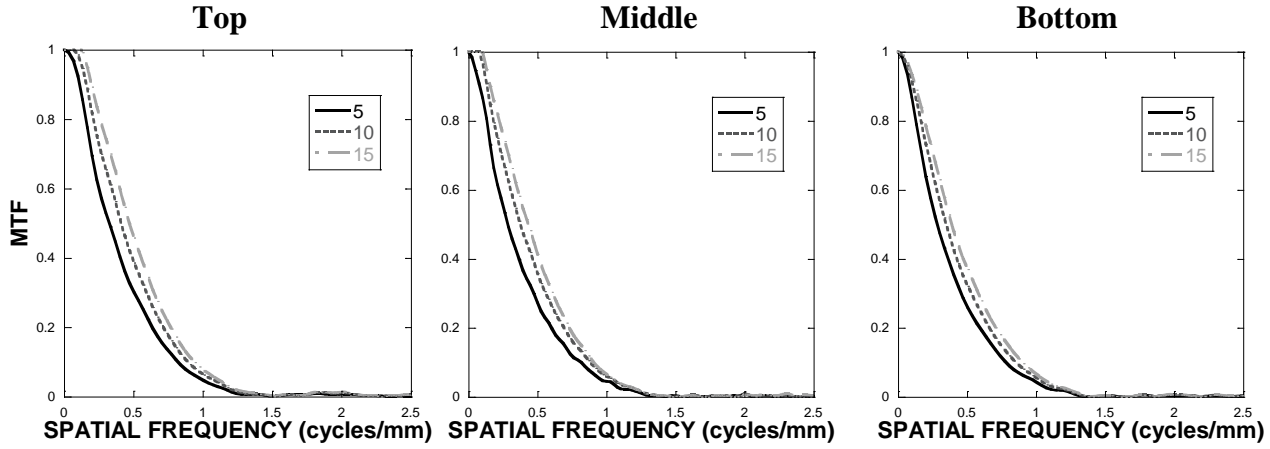


Figure.10: MTF evaluated at different positions along the length of the wire obtained from reconstructed images of a Saddle trajectory acquisition. Very slight variation among the different locations for each line is seen.

Results show that both VAOR and Saddle orbits do not yield large differences in resolution in a $\sim 8 \times 8 \times 8 \text{ cm}^3$ volume. The MTF can improve with increased reconstruction iterations but reaches an optimal point where there is no great change in resolution and contrast. The MTFs of a 50.8micron W-wire measured from the 3D reconstructed data also indicate uniformity in the reconstructed volume. Full details of this study can be found in Appendix D.

Key Research Accomplishments

Summary:

Task 1 (a through e) and Task 3c from the Statement of Work (SOW) (included as Appendix A) were completed in Year 1. Tasks 2a and 2c were completed in their entirety with the completion of a prototype bed as well as evaluation of system orientation and tilts. Evaluation of different breast compositions and lesion sizes has been completed (Task 3a) and upper and lower detection limits as well as effect on breast volume sampling determined. Microcalcification and breast size evaluation for Task 2a remain to be completed. System and acquisition methodologies were evaluated for their effects on resolution metrics (2D and 3D MTF, NPS, DQE) (Task 3b). Artifacts and attenuation coefficient (quantitation) accuracy remain to be evaluated. In summary, Year 3 will be comprised of Task 2b as well as the remainder of Tasks 3a and 3b.

Accomplishments:

1. We continue to evaluate and improve the world's first dedicated tomographic breast imaging device that is capable of 3-dimensionally complex orbits.
2. We have performed the first ever observer study comparing mammotomography and FFDM using realistic breast phantoms and have shown mammotomography to have significant advantages over FFDM, especially for dense breasts.
3. We have designed, developed, and produced a custom bed that will allow imaging closer to the chest wall, the last major challenge of dedicated breast CT.
4. Observer studies have confirmed that we can image at doses lower than dual view mammography while maintaining the ability to detect sub-cm lesions in a dense background.

Reportable Outcomes

Peer-reviewed:

CN Brzymialkiewicz, MP Tornai, **RL McKinley**, SJ Cutler, JE Bowsher, "Performance of dedicated emission mammotomography for various breast shapes and sizes," *Phys. Med. Biol.* **51**: 5051-5064, 2006.

DJ Crotty, **RL McKinley**, MP Tornai, "Experimental spectral measurements of heavy K-edge filtered beams for X-ray computed mammotomography," *Proc. Phys. Med. Biol.* **52**: 603-616, 2007.

Conference Proceedings:

DJ Crotty, **RL McKinley**, MP Tornai, "Experimental spectral measurements of heavy K-edge filtered beams for X-ray computed mammotomography," *Proc. SPIE: Physics of Medical Imaging* **6142**: 664-674, 2006.

DJ Crotty, CN Brzymialkiewicz, **RL McKinley**, MP Tornai, "Investigation of emission contamination in the transmission image in a dual modality computed mammotomography system," *Proc. SPIE: Physics of Medical Imaging* **6142**: 1088-1098, 2006.

P Madhav, **RL McKinley**, E Samei, JE Bowsher, MP Tornai, “A novel method to characterize the MTF in 3D for computed mammotomography,” *Proc. SPIE: Physics of Medical Imaging* **6142**: 697-706, 2006.

RL McKinley, MP Tornai, “Preliminary investigation of dose for a dedicated computed mammotomography system,” *Proc. SPIE: Physics of Medical Imaging* **6142**: 60-70, 2006.

P Madhav, DJ Crotty, **RL McKinley**, MP Tornai, “Initial development of a dual-modality SPECT-CT system for dedicated mammotomography,” Presented at the *2006 IEEE Medical Imaging Conference*, November, 2006 and submitted to *IEEE Conf. Rec. NSS/MIC*.

RL McKinley, MP Tornai, CE Floyd, E Samei, “A contrast-detail comparison of computed mammotomography and digital mammography,” Presented at *SPIE 2007 Medical Imaging Conference*, San Diego, CA, 17-2 Feb. 2007, and submitted to *Proc. SPIE: Physics of Medical Imaging*.

DJ Crotty, P Madhav, **RL McKinley**, MP Tornai, “Investigating novel patient bed designs for use in a hybrid dual modality dedicated 3D breast imaging system,” Presented at *SPIE 2007 Medical Imaging Conference*, San Diego, CA, 17-2 Feb. 2007, and submitted to *Proc. SPIE: Physics of Medical Imaging*.

P Madhav, DJ Crotty, **RL McKinley**, MP Tornai, “Evaluation of lesion distortion of various CT system tilts in the development of a hybrid system for dedicated mammotomography,” Presented at *SPIE 2007 Medical Imaging Conference*, San Diego, CA, 17-2 Feb. 2007, and submitted to *Proc. SPIE: Physics of Medical Imaging*.

Dissertation:

RL McKinley, “Development and Characterization of a Dedicated Computed Mammotomography System”, Duke University, Durham, NC, September 2006.

Awards:

2007 *IEEE Nuclear and Plasma Sciences Society* Graduate Student Award

Conclusions

With our fully synchronized and automated system capable of complex orbits, measurements and observer studies have indicated that we can perform mammotomography scans at a fraction of the dose of dual view mammography and that mammotomography significantly outperforms FFDM through the removal of overlying structure and is most significant in dense breasts. 3D MTF phantoms have been developed and used to show that our system is spatially invariant with respect

to MTF. A prototype bed has been designed and developed and is ready for further phantom evaluation and eventual patient scanning (outside the present scope of the grant). This system shows high promise as a diagnostic tool for women having suspicious mammograms, especially those with dense breasts. Ultimately, it may replace current standard mammography. Future work will include evaluation of performance for different breast sizes, evaluation of microcalcification detection, and evaluation of the feasibility of using vertical bed motion during the scan to get in closer proximity to the chest wall. Chest wall proximity imaging remains the last major hurdle to overcome before clinical introduction of this scanner.

References

- [1] American Cancer Society, "Cancer Facts and Figures," www.cancer.org, 4 (2005).
- [2] M.L. Bradshaw, R.L. McKinley, E. Samei et al., "Initial x-ray design considerations for application specific emission and transmission tomography (ASETT) of the breast," *J. Nucl. Med.* **44** (5), 287P (2003).
- [3] R.L. McKinley, M.P. Tornai, C.N. Brzymialkiewicz et al., "Analysis of a novel offset cone-beam computed mammotomography imaging system for attenuation correction of SPECT in a proposed dual modality dedicated breast mammotomography system," *Presented at the 2004 Workshop on the Nuclear Radiology of the Breast, Rome, Italy and submitted to Physics Medica (In Press)* (2004).
- [4] R.L. McKinley, M.P. Tornai, E. Samei et al., "Development of an optimal x-ray beam for dual-mode emission and transmission mammotomography," *Nucl. Instr. Meth. Phys. Res. A* **527**, 102-109 (2003).
- [5] R.L. McKinley, M.P. Tornai, E. Samei et al., "Initial study of quasi-monochromatic beam performance for x-ray computed mammotomography," *IEEE MIC* **4**, 2999-3003 (2003).
- [6] R.L. McKinley, M.P. Tornai, E. Samei et al., "Initial study of quasi-monochromatic beam performance for x-ray computed mammotomography," *IEEE Trans. Nucl. Sci.* (**In Press**) (2005).
- [7] M.P. Tornai, J.E. Bowsher, C.N. Archer et al., "Feasibility of Application Specific Emission and Transmission Tomography (ASETT) of the breast," *J. Nucl. Med.* **43** (5), 12 (2002).
- [8] M.P. Tornai, J.E. Bowsher, C.N. Archer et al., "A Compact Dedicated Device for Dual Modality Radionuclide Imaging of the Breast with an Application Specific Emission and Transmission Tomograph (ASETT)," *Radiology* **221P**, 555 (2001).
- [9] M.P. Tornai, C.N. Brzymialkiewicz, R.L. McKinley et al., "Development of Dedicated 3D Molecular Mammothomography with SPECT and Quasi-Monochromatic X-ray Computed Mammothomography," presented at the *Workshop on Alternatives to Mammography*, Winnipeg, Manitoba, 2004 (unpublished).
- [10] M.P. Tornai, Y.C. Tai, and R.L. McKinley, "Initial design considerations of a dedicated hybrid mammothomograph for fully 3D x-ray CT and high resolution PET using object magnification," presented at the *Society of Nuclear Medicine Annual Meeting*, Toronto, ON, 2005 (unpublished).
- [11] R.L. McKinley, E. Samei, C.N. Brzymialkiewicz et al., "Measurements of an Optimized Beam for X-ray Computed Mammothomography," *Proc. SPIE: Phys. of Med. Imag.* **5368**, 311-319 (2004).
- [12] R.L. McKinley, M.P. Tornai, E. Samei et al., "Simulation Study of a Quasi-Monochromatic Beam for x-ray Computed Mammothomography," *Med. Phys.* **31** (4), 800-813 (2004).
- [13] R.L. McKinley, M.P. Tornai, E. Samei et al., "Optimizing Beam Quality for x-ray Computed Mammothomography (CmT)," *Proc. SPIE* **5030**, 575-584 (2003).
- [14] M.P. Tornai, C.N. Archer, J.E. Bowsher et al., "Transmission imaging with a compact gamma camera: initial results for mammothomography," *IEEE Nucl. Sci. Symp. and Med. Imag. Conf. Rec.* **3**, 1597-1601 (2002).
- [15] NCRP Report, "Quality of Mammography Committee Recommendation," **SC-72** (2002).
- [16] J.M. Boone, N. Shah, and T.R. Nelson, "A comprehensive analysis of DgNCT coefficients for pendant-geometry cone-beam breast computed tomography," *Med. Phys.* **31** (2), 226-235 (2002).
- [17] J.M. Boone and J.A. Seibert, "A comparison of mono- and poly-energetic x-ray beam performance for radiographic and fluoroscopic imaging," *Med. Phys.* **21**, 1853-1863 (1994).
- [18] J.T. Dobbins, E. Samei, H.G. Chotas et al., "Chest Radiography: Optimization of x-ray spectrum for cesium iodide-amorphous silicon flat-panel detector," *Radiology* **226** (1), 221-230 (2002).

- [19] J.M. Boone, T.R. Nelson, K.K. Lindfors et al., "Dedicated Breast CT: Radiation Dose and Image Quality Evaluation," *Radiology* **221**, 657-667 (2001).
- [20] B. Chen and R. Ning, "Cone-beam volume CT mammographic imaging: feasibility study," *Med. Phys.* **29**, 755-770 (2002).
- [21] A.A. Vedula and S.J. Glick, "Computer simulations of CT mammography using a flat panel imager," *Proc. SPIE* **5030**, 349-360 (2003).
- [22] M.P. Tornai, J.E. Bowsher, C.N. Archer et al., "A 3D Gantry Single Photon Emission Tomograph with Hemispherical Coverage for Dedicated Breast Imaging," *Nucl. Instr. Meth. Phys. Res. A* **497**, 157-167 (2003).
- [23] R.L. McKinley, M.P. Tornai, C.N. Archer et al., "Quasi-monochromatic beam measurements for dedicated cone-beam mammotomography of an uncompressed breast," presented at the 7th *International Workshop on Digital Mammography*, Durham, NC, 2004 (unpublished).
- [24] M.P. Tornai, R.L. McKinley, M.L. Bradshaw et al., "Effects of uncompressed breast composition and thickness on image quality using a quasi-monochromatic beam for computed mammotomography," presented at the 7th *Int. Workshop on Digital Mammography*, Durham, NC, 2004 (unpublished).
- [25] R. Ning, B. Chen, D. Conover et al., "Flat panel detector-based cone beam volume CT mammography imaging: preliminary phantom study," *Proc. SPIE* **4320**, 601-610 (2001).
- [26] J.M. Boone, A.L.C. Kwan, J.A. Seibert et al., "Technique factors and their relationship to radiation dose in pendant geometry breast CT," *Med. Phys.* **32** (12), 3767-3776 (2005).
- [27] R.L. McKinley, C.N. Brzymialkiewicz, P. Madhav et al., "Investigation of cone-beam acquisitions implemented using a novel dedicated mammotomography system with unique arbitrary orbit capability," *Proc. SPIE: Phys. of Med. Imag.* **5745**, 609-617 (2005).

Appendices

Appendix A

STATEMENT OF WORK

Task 1 Implement prototype system for unique acquisition capabilities (Months 1-12)

- a. Implement mounting system for X-ray source and detector for flexible acquisitions involving azimuthal rotation and polar tilt (Months 1-2)
- b. Automate data acquisition sequence, synchronizing detector readout in software with gantry control and generator exposure initiation (Months 2-3)
- c. Perform initial phantom measurements using Catphan and other 3D geometric frequency/resolution phantoms to optimize cone-beam reconstruction, utilizing ordered subsets based iterative transmission reconstruction techniques for 3D cone-beam acquisition (Months 4-6)
- d. Using simple acquisition geometries, optimize image gain, offset, and line correction algorithms to maximize projection image quality and noise reduction (Months 5-7)
- e. Design and evaluate offset half cone-beam using 360 degree acquisition as well as horizontal versus vertical positioning of detector for maximizing range of uncompressed breasts accommodated (Months 8-12)

Task 2 Design and evaluate unique acquisition geometries (Months 13-26)

- a. Investigate unique 3D cone-beam orientations and tilt angles for optimal orientation relative to the longitudinally oriented patient chest wall (Months 13-18)
- b. Evaluate feasibility of utilization of patient bed motion versus camera system motion to provide vertical displacements *during* a scan at specific azimuthal and polar acquisition angles, to circumvent the physical limitations of the patient's torso by exploiting the unhindered spaces along the sides of the patient (Months 19-23)
- c. Modify patient bed materials and breast opening size as well as bed contour to maximize curvature (and comfort) of patient chest for full volumetric sampling, including chest wall (Months 23-26)

Task 3 Evaluate various breast sizes, compositions, lesion sizes, microcalcifications (Months 27-36)

- a. Evaluate different breast sizes, compositions, lesion sizes, microcalcifications to determine upper and lower detection limits as well as effect on breast volume sampling (Months 27-31)
- b. Evaluate system and acquisition methodologies for effects on image quality including signal to noise ratio, dose efficiency, contrast sensitivity, resolution metrics (2D and 3D MTF, NPS, DQE), artifacts, and attenuation coefficient (quantitation) accuracy (Months 32-36)
- c. Determine normalized glandular dose coefficients for CmT acquisitions for dose determination in preparation for clinical trials (Months 32-36)

Appendix B

SPIE 2007 Medical Imaging Conference – presented San Diego, February, 2007.

A Contrast-Detail Comparison of Computed Mammotomography and Digital Mammography

Randolph L. McKinley,^{1,2} Martin P. Tornai,^{1,2,4} Carey E. Floyd^{1,2}, Ehsan Samei,^{1,2,3,4}

¹ Department of Radiology, Duke University Medical Center, Durham, NC

² Department of Biomedical Engineering, Duke University, Durham, NC

³ Department of Physics, Duke University, Durham, NC

⁴ Medical Physics Graduate Program, Duke University, Durham, NC

ABSTRACT

We use a contrast-detail observer study to compare performance of a novel 3D computed mammotomography (CmT) system with a commercially developed full-field digital mammography (FFDM) system. A contrast-detail phantom comprised of uniform acrylic spheres of various diameters was developed and placed in a variety of mediums including uniform water (simulating low contrast lesions within a uniform background), water and acrylic yarn (simulating low contrast lesions with over/under-lying structure), oil only (simulating higher contrast lesions in a uniform background), and oil and acrylic yarn (simulating higher contrast lesions with over/under-lying structure). For CmT, the phantom was placed in a 14.6 cm diameter uncompressed breast phantom and projections acquired using a simple circular orbit, W-target tube, 60 kVp tube potential, 0.05 cm Ce filtration, 4 mAs per projection, and a CsI(Tl) digital x-ray detector. Reconstructions used an iterative OSTR algorithm. For FFDM, the phantom was placed in a 5.3-cm-thick compressed breast phantom. Single CC-view mammograms were acquired using a clinical W-target tube with 50 um Rh filtration, 28 kVp, photo-timed mAs per our clinical mammography operation, and a Selenium-based flat-panel detector (Mammomat Novation, Siemens). Six observers evaluated the images in terms of the number of detectable spheres. FFDM performed significantly better for the low contrast lesions in uniform water background ($p < 0.05$). However, CmT performed significantly better for all other cases ($p < 0.05$). Results indicate that CmT shows significant advantage in soft tissue detection over FFDM in otherwise low contrast dense breasts.

Keywords: X-ray computed mammotomography, contrast-detail, breast imaging, cone-beam, CT, FFDM.

INTRODUCTION

Observer studies are used for evaluating imaging system capabilities and have been commonly used for tomography.¹⁻³ Breast CT is an emerging technology being developed by several groups⁴⁻⁸ and has only recently been introduced into clinical trials. A recent comprehensive study comparing dedicated breast CT with digital mammography was undertaken by use of computer simulated data.⁹ That study also examined breast tomosynthesis performance. Their receiver operator characteristic (ROC) study findings indicated statistically significantly higher detection confidence for a 5mm lesion for both tomosynthesis and breast CT as compared to digital mammography. Differences in lesion detection between tomosynthesis and breast CT were not significant, although breast CT was higher in detection confidence.

In this study, our goal was to compare CmT versus digital mammography using an experimental 3-dimensional (3D) breast phantom. We have developed a complex 3D phantom to allow evaluation and comparison of the prototype CmT system with an existing commercial full field digital mammography (FFDM) system. This comparison is important in order to gain confidence in the relative merit of CmT compared to more conventional mammography.

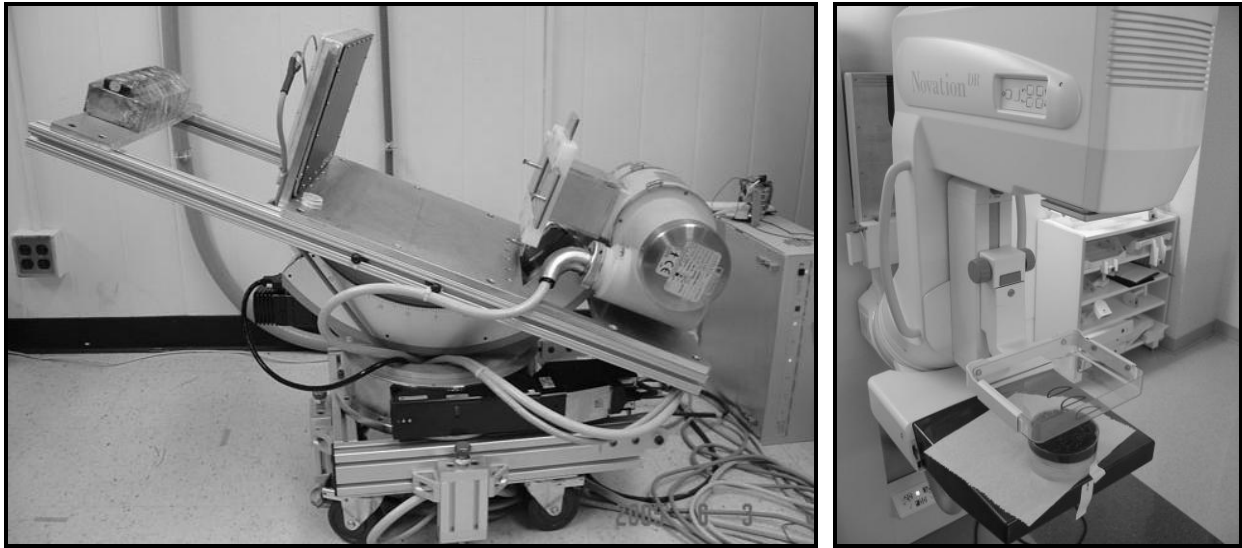


Figure 11. Photos illustrating (left) CmT apparatus with Varian Rad-94 W target x-ray tube, Varian Paxscan 2520 digital x-ray detector, Newport BGM200PE goniometer for polar motion (below platform), and Newport RV350CC rotation stage for azimuthal motion (bottom) to allow for arbitrary complex orbits; and (right) Siemens Mammomat Novation FFDM system with a phantom in the field of view..

MATERIALS AND METHODS

CmT Apparatus Description and Experimental Techniques

The CmT system is composed of a Varian Rad-94 W target x-ray source and Varian Paxscan 2520 (Varian Medical Systems, Salt Lake City, UT) CsI(Tl) amorphous silicon digital x-ray detector (127 micron pixels) mounted on a Newport BGM200PE goniometer for polar motion and Newport RV350CC rotation stage (*Newport Corp.*, Irvine, CA) for azimuthal motion (Figure 1). This system has been described previously in detail.^{7,10} For CmT, the sphere phantom was placed in a 14.6 cm medial-to-lateral uncompressed breast phantom (20 cm superior-to-inferior, 7.4 cm nipple-to-chest) containing ~700mL fluid (Figure 11, right), suspended into the cone-beam field of view (FOV), and projections acquired using a simple circular orbit. Scans were acquired using a 60 kVp tube potential, 0.05 cm Ce filtration, and 4 mAs per projection. Reconstructions used 240 4x4 binned projections, 8 subsets, and 20 iterations with 0.125 mm³ voxels. The water only and oil only configurations were scanned three times each. The yarn configuration with water or oil media was scanned five times, with the yarn being randomly altered by hand between each of the five scans. This was done to vary the structural background, so that no one sphere would be intentionally hidden or masked in some unknown way or due to imperfections in the yarn or its placement.

Phantoms

Many evaluation phantoms are currently available for mammography¹¹ and CT.³ However, these phantoms are designed for a single modality evaluation and are specifically developed that way. Given the drastic differences between uncompressed breast CT and compressed breast mammography, a phantom suitable for both modalities had to be custom developed since no such phantom is currently available to suit both purposes.

In addition, a fair comparison of mammography and breast CT should include structural “noise” in the form of structure overlying, if not completely surrounding, the “signal” of interest. Thus, a contrast-detail phantom was developed for this comparison. The “signals” of interest consisted of 12 acrylic spheres (density: 1.19 g/cm³) ranging in size from 1.0 to 14.3 mm diameter (*Engineering Laboratories, Inc.*, Oakland, NJ), arranged in decreasing size at approximate clock number positions around a circle (Figure 12). Acrylic yarn (100% acrylic) was selected to provide the overlying structural component simulating connective breast tissue in those test cases involving structured backgrounds. The spheres were glued using an ethyl cyanoacrylate based glue (Krazy Glue, *Elmer's Products, Inc.*, Columbus, OH) to a heat shrinkable woven polyester modeling airplane “skin” (Coverite, *Great Planes Model Distributors*, Champaign, IL) stretched and glued to a circular wooden frame ring.

The sphere phantom was placed in a variety of mediums including uniform water (to simulate low contrast lesions within a uniform, high density (1.0 g/cm³) breast background), water with acrylic yarn (to simulate low contrast lesions with over/under-lying structure), oil only (to simulate higher contrast lesions in a lower breast density of 0.93 g/cm³),¹² , and oil with acrylic yarn (to simulate higher contrast lesions with over/under-lying structure) (Figure 12).

The amount of yarn to use was initially determined by filling the oil-filled breast phantom container with the spheres and yarn for FFDM and then removing amounts of yarn until some of the spheres became clearly visible.

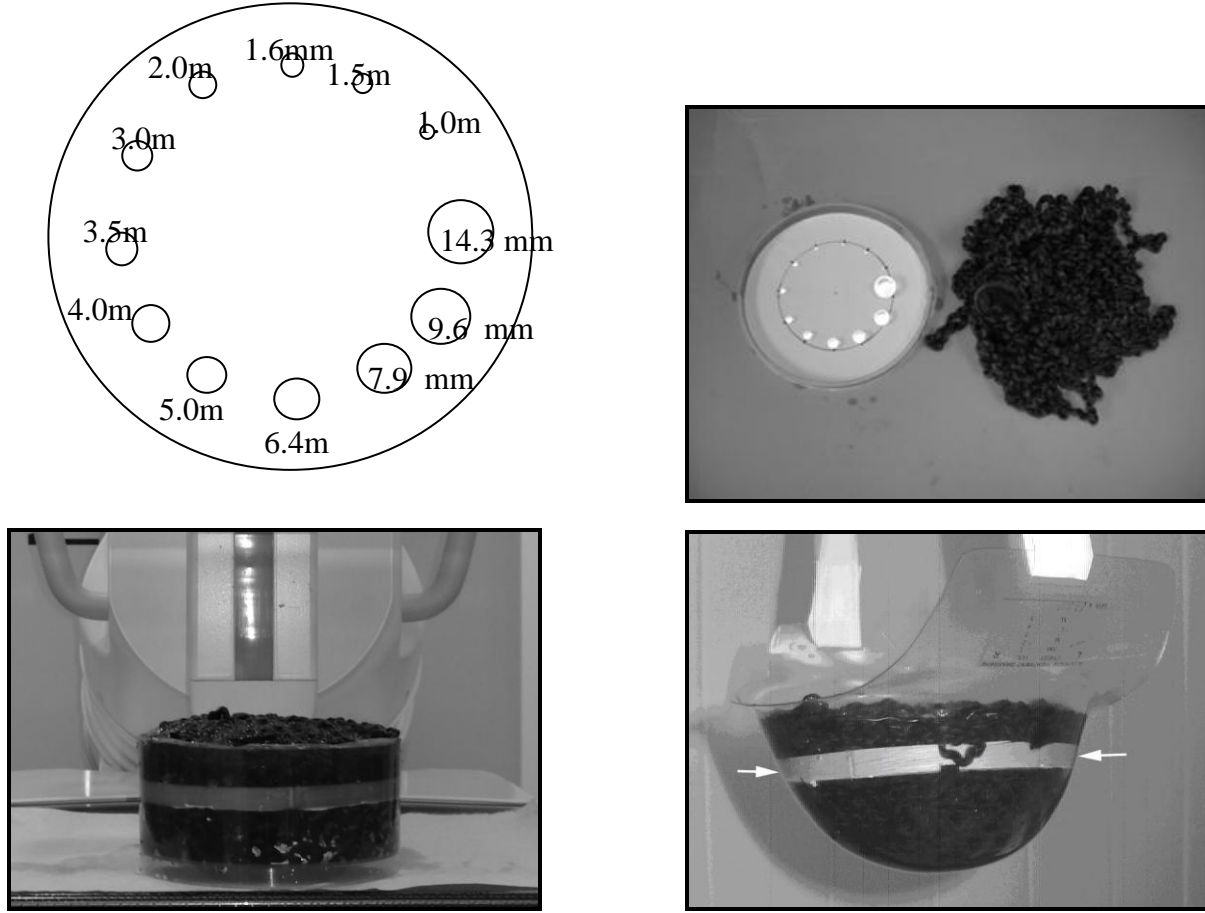


Figure 12. (Top left) schematic of contrast-detail phantom (approx. 15cm in diameter) indicating decreasing size of acrylic spheres; (top right) photograph of phantom and yarn that was surrounded the phantom; (bottom) photographs of the 700mL 3D phantoms in (left) “compressed” mode on the FFDM detector, and (right) in fully “uncompressed” mode in the CmT FOV. Note that the wooden frame (indicated by arrows) is concave up, with the spheres inside it, so that the spheres are completely covered and surrounded by yarn.

Digital Mammography and Experimental Techniques

For FFDM, the sphere phantom was placed in a 5.3-cm-thick, 15 cm diameter cylindrical “compressed breast” phantom containing the same spherical and yarn objects and the same volume of medium added as for the uncompressed breast (Figure 12, left), and placed entirely in the FOV of the system. The appropriate thickness for the compressed breast corresponding to the uncompressed breast was determined from a linear relationship derived from empirical observations and measurements of women’s breasts,⁵ and expressed as:

$$CBT = \frac{BD - 5.84}{1.66} \quad (1)$$

where CBT is the compressed breast thickness and BD is the uncompressed breast diameter (14.6 cm for the CmT breast phantom used above).

Single CC-view mammograms were acquired using a clinical FFDM mammography device (Mammomat Novation, Siemens, Malvern, PA). The Mammomat Novation has a W-target tube, 65 cm SID, and a 2560x3328 pixel Selenium-based flat-panel detector with 70 micron pixel pitch. It was operated with 50 micron Rh filtration (Figure 11), 28 kVp, photo-timed mAs per our clinical mammography operation. Uniform and structured background images were acquired 3

and 5 times each, respectively, for water and oil media, with the yarn being moved around 3-dimensionally for each different acquisition. This was done to vary the structural background, so that no one sphere would be intentionally hidden or masked in some unknown way or due to imperfections in the yarn or its placement.

Observer Image Preparation

CmT image preparation for the observer study was performed using *ImageJ* image display and manipulation software (<http://rsb.info.nih.gov/ij/>). The 20th iteration stack of 384 coronal slices was smoothed with 2-pixel width Gaussian filter across orthogonal planes. The stack was windowed and leveled by placing an ROI on the largest lesion, using auto window, then back-stepping 10 steps in gray level and resizing the stack by applying a magnification factor of 2. This was done so that the final viewed size of the breast would be displayed at the same size as the FFDM image data, though the CmT intrinsic (binned) pixel size (0.5 mm) was significantly smaller than that of the FFDM images (0.07 mm).

For digital mammography image preparation, the DICOM images were windowed and leveled by placing an ROI around the largest lesion and performing an auto window. The windowed and leveled image was then resized by with a magnification factor of 0.26 (so that the final viewed size of the breast and spheres would be displayed at the same size as the CmT image data. The observers were not able to manipulate the gray level or magnification of the images during the study. These were fixed parameters, obtained as described above.

Image Reading Conditions

All image readings were done in a controlled environment with 0.96 ± 0.02 lux with the head positioned at about a 50 cm distance from the three megapixel monochromatic LCD display screen (model G31, *Eizo Nanao Corp.*, Cypress, CA). The display pixel size was 0.207 mm and it was calibrated to a minimum luminance of 0.75 cd/m^2 and a maximum of 450 cd/m^2 (for a typical mammographic viewing range). Images were resized such that the size of the phantom on the display was identical for both CmT and mammography. Images were viewed in random order, where the order was varied for each observer. Six observers evaluated the images in terms of the number of detectable spheres on randomly presented, interspersed, FFDM and CmT image data sets. The observers were allowed to scroll through the CmT slices to view the entire 3D image data. They determined for themselves where they needed to look for the spheres, though they were given a schematic with instructions as to the layout and general locations of the spheres on a circle. Each reader was given a form to fill in and instructed to indicate how many spheres they saw. Randomly displayed data results were then resorted for subsequent analysis. Resulting data was compared for significance using a Student's t-test at significance level of $p < 0.05$.

RESULTS AND DISCUSSION

Reconstructed CmT coronal views (Figure 13) and FFDM DICOM images (Figure 14) are provided for each of the cases tested. Profiles were drawn through the 5 mm sphere in the water medium (Figure 15) and the oil medium (Figure 16) for mammography images and CmT reconstructed slices. Profiles indicate that: (1) the structural background provided by yarn affects the profile to a much greater degree for mammography than for CmT, especially for the water medium case; and (2) for the high contrast case of oil media, although structural background affects the profile, the sphere is still clearly apparent in the profile, whereas for water, it becomes much more difficult to pick out; (3) while the digital mammography images may have better spatial resolution (though we have sub-sampled the images), their contrast-resolution is severely reduced in the presence of the structural noise due to the yarn.

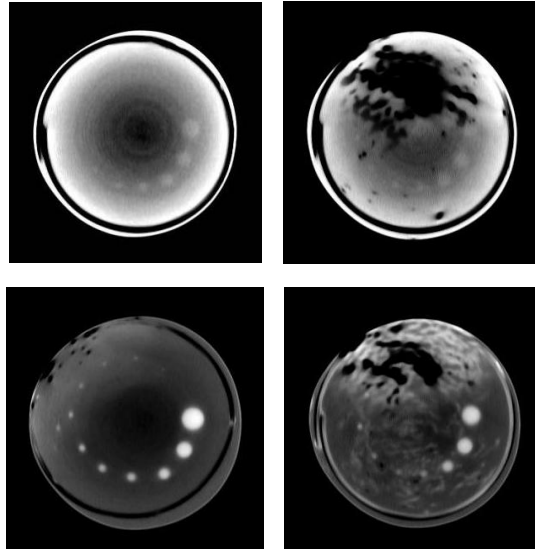


Figure 13. Reconstructed coronal views with fixed window/level of the CmT acquisitions for (top left) water only, (top right) water and yarn, (bottom left) oil only, and (bottom right) oil and yarn. Acquisition and reconstruction parameters included 60 kVp tube potential, 240 projections, 4.0 mAs per projection, 8 subsets, 20 iterations, 350x350x384 grid size. Note that dark black regions at the diameter of the spheres in the yarn cases are a result of air bubbles caught in the fluid-yarn mixture.

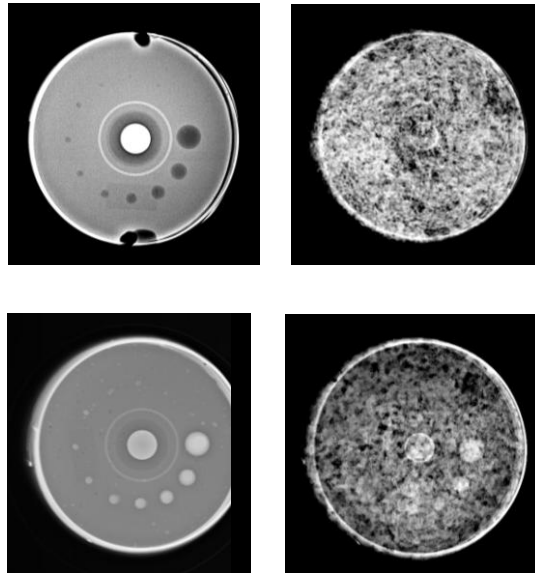


Figure 14. DICOM format images with fixed window/level from the Seimens Mammomat Novation FFDM system for (top left) water only, (top right) water and yarn, (bottom left) oil only, and (bottom right) oil and yarn. Acquisition parameters included W-target tube with 50 um Rh filtration, 28 kVp, photo-timed mAs ranging from a low of 96.3 (oil/yarn) to a high of 256 (water/yarn) per our clinical mammography operation, and a Selenium-based flat-panel detector. Note that central rings and objects in the images at a smaller radius than for the spheres are due to the structure of the compact disk case cylinder used to hold the spheres and yarn.

A transform was obtained between the sphere size and sphere number. The transform was determined by performing a 4th degree polynomial fit of sphere number to sphere size (Figure 17). This plot is then used to determine the asymmetric errors in observer detection with the conversion of sphere number to size.

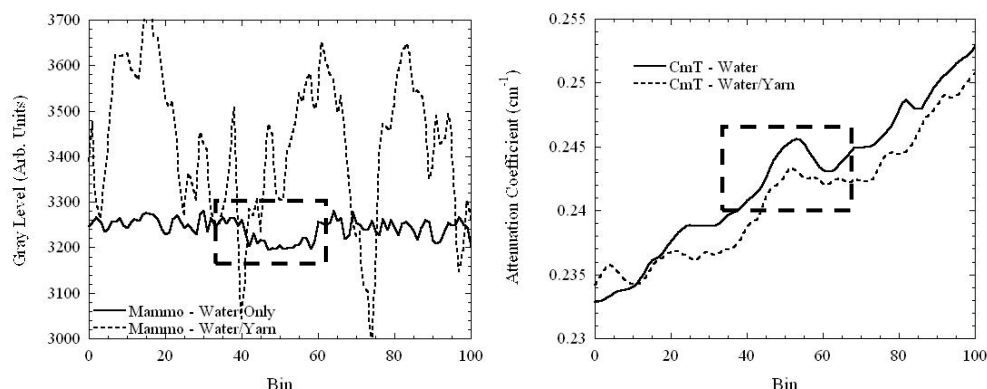


Figure 15. Profiles through 5mm diameter sphere for water only and water/yarn for (left) mammography and (right) CmT. Dashed squares indicate signal location. The slope in the CmT profile is due to the scatter-induced cupping artifact which is noticeable with the extreme windowing on the data. Note the attenuation coefficient range varies by only 5% to either side of the "lesion" signal.

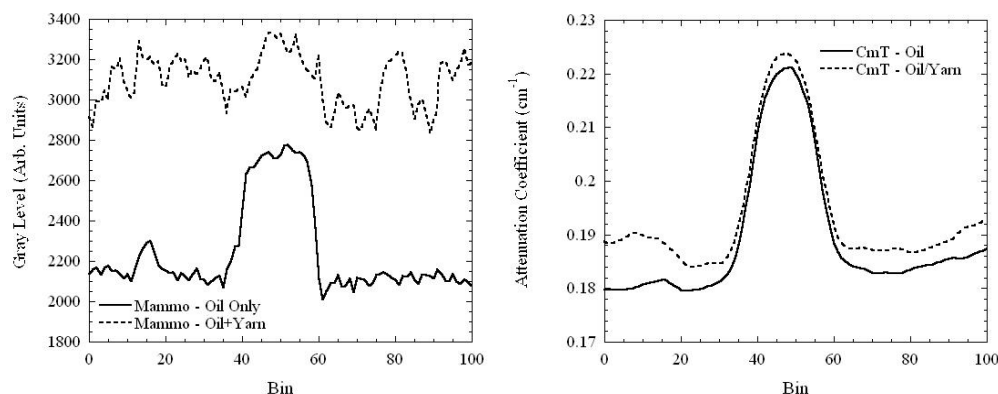


Figure 16. Profiles through 5mm sphere for oil only and oil/yarn for (left) mammography and (right) CmT.

For FFDM, dose calculations were performed using Boone's spectral model and a program (courtesy of Dr. Joseph Lo, Duke University) that allowed input of glandular fraction and compressed breast thickness, and provided a conversion factor in units of mGy/R. Exposure readings in mR were taken at the "skin" entrance point (5.3 cm above the detector plate on the Mammomat Novation) with an ionization chamber (model 1515, *Radcal Corp.*, Monrovia, CA) for three tube mAs settings. Exposures to be used for converting mGy/R to dose was determined by mapping the specific mAs technique, used for each test set, to an exposure (in mR) using the linear curve fit ($R^2=1$). Dose conversion factors from Boone's spectral model were determined using an assumption of 100% glandular for water, 50% glandular for water and yarn, 0% glandular for oil, and 50% glandular for oil and yarn.

For CmT, dose was approximated beginning with 50% adipose/50% glandular conversion tables for a 15 cm uncompressed breast and then adjusting these values based on Boone's coefficient plots for other compositions.¹³

Table 1 provides calculated doses using these assumptions. In the absence of a better method for determining dose (e.g. direct measurement) for the cases with yarn included in the medium, dose was calculated using 50% adipose/50% glandular tables.

Mean and standard deviation in number and size of detected spheres for water (Figure 18) and oil (Figure 19) are illustrated. These resulting data were tested for statistical significance ($p<0.05$). FFDM performed significantly better

than CmT for the low contrast lesions in uniform water background. However, CmT performed significantly better than FFDM for all other cases.

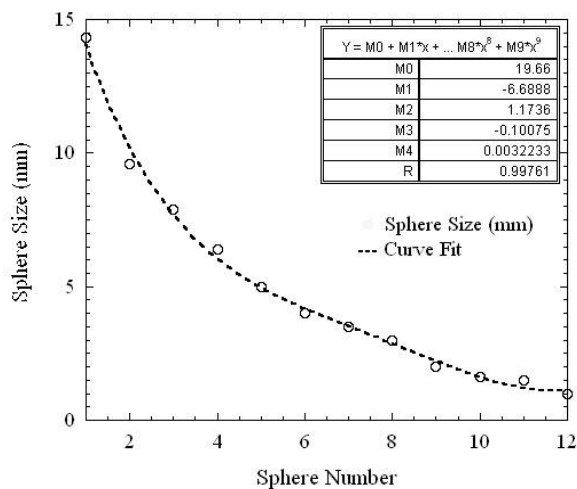


Figure 17. Transform of sphere number to actual sphere size with a 4th order polynomial fit (coefficients provided in legend).

Table 1. Calculated dose for the test cases used in the observer study for single view FFDM and fully 3D CmT.

Test Set	Approximate FFDM Dose (mGy)	Approximate CmT Dose (mGy)
Water only	2.0	5.2
Water and Yarn	2.5	5.9
Oil Only	3.8	6.5
Oil and Yarn	1.2	5.9

Median smallest detectable spheres for CmT/FFDM for water only, water/yarn, oil only, and oil/yarn were 3.5/1.8, 4.0/2.0, 1/1.5, and 1.8/7.9 mm. Ranges for CmT/FFDM for water only, water/yarn, oil only, and oil/yarn were: 3-5/1.5-3, 3-6.4/9.6-20, 1-1.5/1-3, and 1.5-3.5/5-20 mm.

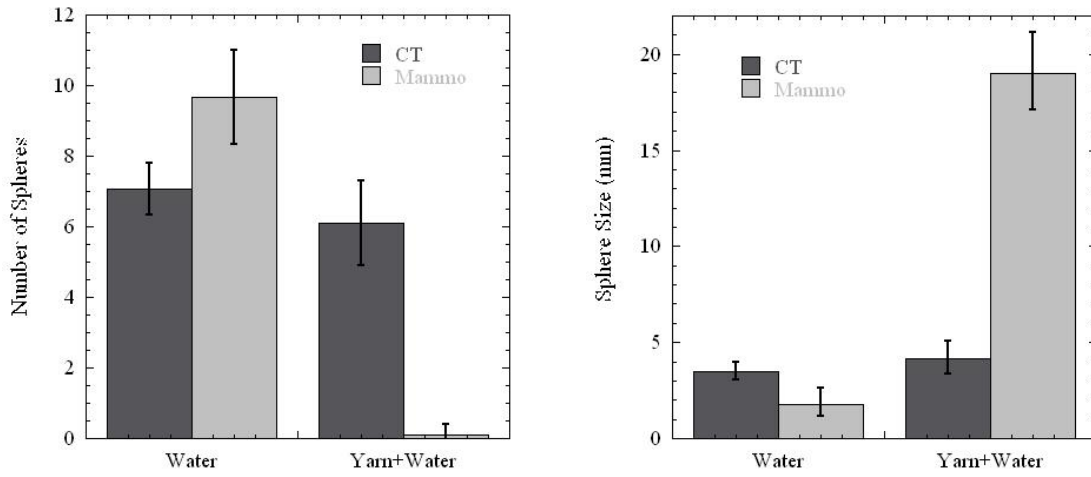


Figure 18. Results for observer studies indicating mean and standard deviation for (left) number of spheres detected and (right) mean sphere size detected for CmT and FFDM for (from left to right in each plot) water only, and water/yarn. Statistically significant differences between means were determined with a Student t-test for $p < 0.05$, and significantly different results were found in all cases.

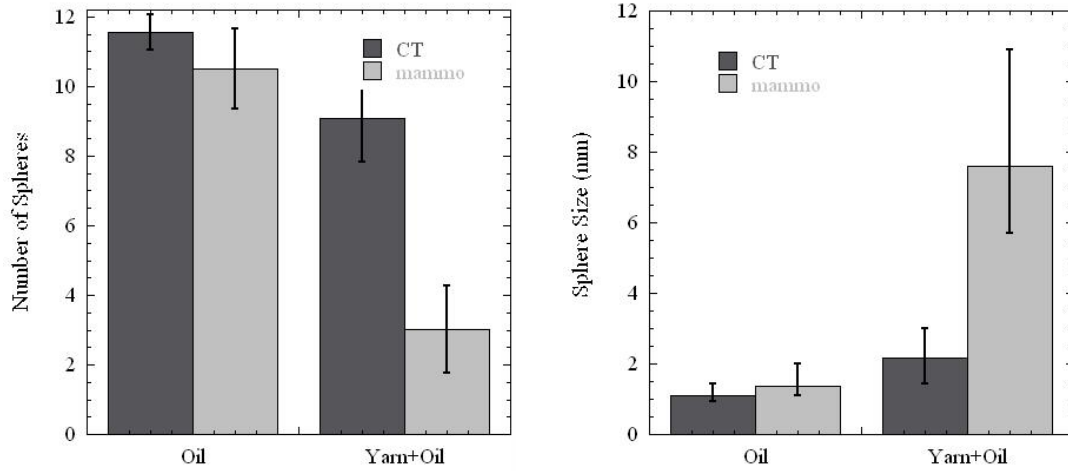


Figure 19. Results for observer studies indicating mean and standard deviation for (left) number of spheres detected and (right) sphere size detected for CmT and FFDM for (from left to right in each plot) oil only, and oil/yarn. Statistically significant differences between means were determined with a Student t-test for $p < 0.05$, and significantly different results were found in all cases.

Notwithstanding the findings of the study, a number of limitations should be acknowledged. Firstly, we are comparing a prototype CmT system from an academic laboratory with a commercially available clinical system from a major imaging equipment manufacturer (*Siemens*). This puts the developed CmT system at a disadvantage for several reasons including:

- 1) Limitations in statistical reconstruction software limit the number of CT projections to approximately 240. This results in an under-sampled data set. Based on Nyquist criteria, sampling should include at least 750 projections; some researchers doing CmT perform 1000 projection acquisitions to reduce noise in the reconstructions.^{4,14}
- 2) The same statistical reconstruction software limitations result in a requirement for 4x4 pixel binning of the projections. This effectively results in 0.51x0.51mm pixel sizes in the projection images for CmT, reducing resolution significantly. This compares to a pixel size of 70 μm (a 52X smaller area) for FFDM.
- 3) Commercial CT systems implement a number of proprietary correction algorithms which have been developed over many years by a large team of engineers. Although we have implemented the basic gain, offset, and defective pixel corrections, many corrections remain to be implemented for the CmT system including scatter correction, beam hardening, image lag correction, and others. Beam hardening is

minimized by use of a quasi-monochromatic x-ray cone beam.^{7,8,12} These corrections, when fully implemented, are expected to significantly improve CmT image quality and system performance.

Mammography in this experiment was not without its own disadvantages. For example, only a single CC view of the phantom was taken. Normally, a radiologist would have a second MLO image to work with as well. This was not possible with the phantom we developed due to the fact that the phantom also required the ability to be used for a completely different modality.

Another drawback to a phantom observer study comparing the two modalities is that the results are dependent on the phantom design. One could have designed a phantom to prove that CmT outperforms mammography when there is overlying structure simply by placing two layers of the same sphere phantom on top of each other, and then asking the observer how many spheres they see. Although this would have proved the point, it would have been less than realistic.

Another related disadvantage for mammography is that the dose per single view image was less than the dose per reconstruction for CmT (Table 1). This was by design. The study was specifically designed to compare standard mammography at standard dose per view (where, in principle, a view would be at half the dose of a dual view image set) with CmT at the standard total dose limit for dual view mammography. Thus, one could argue that some of the differences observed were due to dose differences between the images. While this may be true, it is also supposed that a second view would not have contributed significant additional conformational information, where the first view provides the ideal non-overlapping best case.

CONCLUSIONS

The contrast-detail observer results indicate that, while CmT shows no advantage in cases where lesions are otherwise clearly visible (e.g. in the extremely fatty breast), it may provide significant advantage over FFDM in more difficult cases (e.g. low contrast dense breasts). FFDM performed significantly better than CmT for the low contrast lesions in uniform water background ($p < 0.05$). However, CmT performed significantly better than FFDM for all other cases.

Quantitative observer results have been obtained which indicate potential clinical conditions or indications for computed mammatomography where it may offer significant improvements over the status quo. While it is premature to say that CmT will replace screening mammography, there is certainly the potential that it could. We can say that CmT may provide better visibility in the most difficult cases where low contrast lesions exist in dense breasts which usually contain considerable overlying heterogeneous structure. In addition, CmT has shown the ability to visualize simulated soft tissue lesions on the order of 3 to 4 mm for very difficult cases with low contrast and considerable overlying structure.

ACKNOWLEDGEMENTS

This work is supported by NIH Grant R01-CA096821 and DAMD Grant W81XWH-05-1-0280. The authors thank Dr. Joseph Lo and Nicole Ranger for assistance with the digital mammography acquisitions and mammography dose calculations, and all the study participants and coauthors (Dr. Martin Tornai, Dr. Ehsan Samei, Dr. Carey Floyd, Dr. Sujata Ghate, Priti Madhav, Spencer Cutler, Dominic Crotty, Kristy Perez, Danny Joseph, Swatee Singh).

REFERENCES

- [1] K. Faulkner and B.M. Moores, "Contrast-detail assessment of computed tomographic scanners," *Phys. Med. Biol.* **31** (9), 993-1003 (1986).
- [2] E.C. McCullough, "Specifying and evaluating the performance of computed tomography (CT) scanners," *Med. Phys.* **7** (4), 291-296 (1980).
- [3] F.R. Verdun, A. Denys, J.F. Valley et al., "Detection of low-contrast objects: experimental comparison of single- and multi-detector row CT with a phantom," *Radiology* **223**, 426-431 (2002).
- [4] B. Chen and R. Ning, "Cone-beam volume CT mammographic imaging: feasibility study," *Med. Phys.* **29**, 755-770 (2002).
- [5] J Boone, "Breast CT: Its prospects for breast cancer screening and diagnosis," *RSNA Categorical Course in Diagnostic Radiology Physics*, 165-177 (2004).

- [6] A.A. Vedula and S.J. Glick, "Computer simulations of CT mammography using a flat panel imager," *Proc. SPIE: Phys. of Med. Imag.* **5030**, 349-360 (2003).
- [7] R.L. McKinley, C.N. Brzymialkiewicz, P. Madhav et al., "Investigation of cone-beam acquisitions implemented using a novel dedicated mammotomography system with unique arbitrary orbit capability," *Proc. SPIE: Phys. of Med. Imag.* **5745**, 609-617 (2005).
- [8] R.L. McKinley, M.P. Tornai, E. Samei et al., "Simulation study of a quasi-monochromatic beam for X-ray computed mammotomography," *Med. Phys.* **31** (4), 800-813 (2004).
- [9] X. Gong, S.J. Glick, B. Lui et al., "A computer simulation study comparing lesion detection accuracy with digital mammography, breast tomosynthesis, and cone-beam CT breast imaging," *Med. Phys.* **33** (4), 1041-1052 (2006).
- [10] M.P. Tornai, R.L. McKinley, C.N. Brzymialkiewicz et al., "Design and development of a fully-3D dedicated X-ray computed mammotomography (CmT) system," *Proc. SPIE: Phys. of Med. Imag.* **5745**, 189-197 (2005).
- [11] M. Pachoud, D. Lepori, J.F. Valley et al., "A new test phantom with different breast tissue compositions for image quality assessment in conventional and digital mammography," *Phys. Med. Biol.* **49** (5267-5281) (2004).
- [12] M.P. Tornai, R.L. McKinley, S.J. Cutler et al., "Anthropomorphic breast phantoms for preclinical imaging evaluation with emission or transmission imaging," *Proc. SPIE: Phys. of Med. Imag.* **5746**, 825-834 (2005).
- [13] J.M. Boone, N. Shah, and T.R. Nelson, "A comprehensive analysis of DgNCT coefficients for pendant-geometry cone-beam breast computed tomography," *Med. Phys.* **31** (2), 226-235 (2002).
- [14] A. Kwan, N. Shah, G. Burkett et al., "Progress in the development of a dedicated breast CT scanner," *Proc. SPIE: Phys. of Med. Imag.* **5368**, 304-310 (2004).

Appendix C

Dissertation Excerpts – September 2006

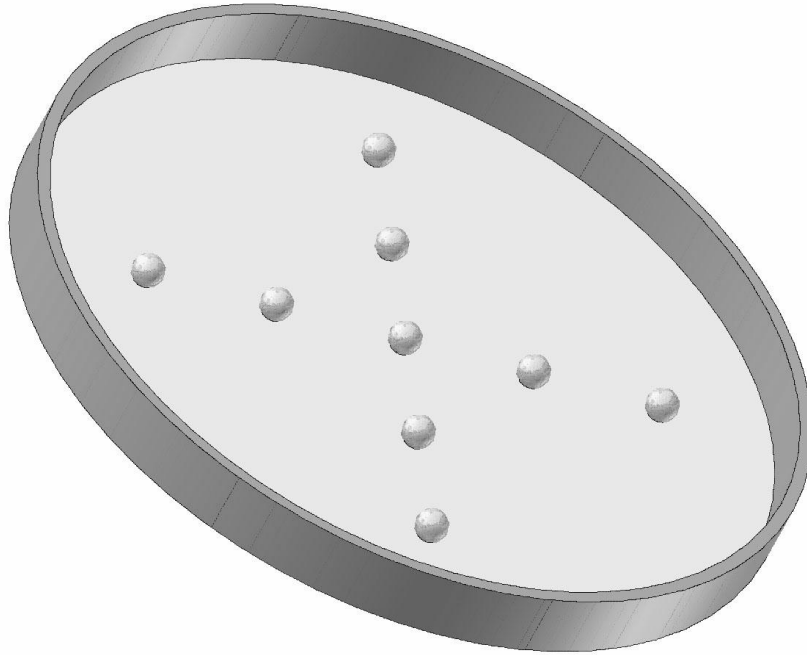


Figure 1 Schematic of cross phantom with 5mm acrylic spheres arranged in a cross pattern and glued to the surface of a thin plastic sheet. This sheet is then glue to a wooden frame. Spheres are placed approximately 2cm apart and a total of 9 spheres are placed on the sheet (graphic is courtesy of Priti Madhav).

The phantom was placed, in the first case, fully within the field of view near the central plane of the cone-beam, as a baseline for image quality for objects within the FOV and an acquisition obtained using a simple circular orbit. Next, the phantom was raised 6.9cm and placed such that the spheres were outside the FOV when the tube-detector pair was positioned such that the top rays of the cone-beam were horizontal. In this case, any information about the spheres can ONLY be obtained through system tilt (i.e. complex orbits). Saddle acquisitions were then performed. Acquisition parameters included: 60kVp tube potential, 100th VL Ce filtration, 240 projections, 4 mAs per projection, 4x4 binning, and 10 iterations. The saddle acquisition used an angle range of $\pm 20^\circ$.

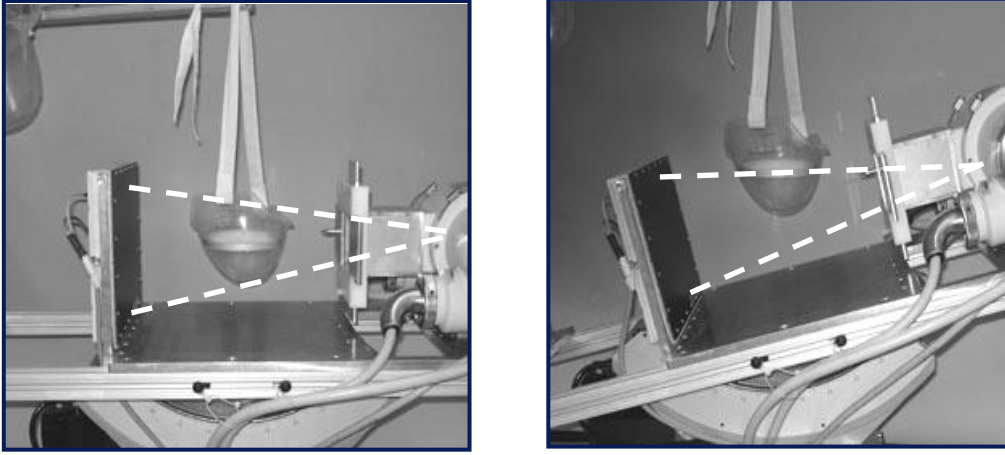


Figure.2 (left) Positioning of cross-phantom fully within the FOV for all projections. In this case, the cross-phantom is centered in the cone-beam when the central ray of the cone-beam is horizontal. (right) Positioning of cross-phantom fully outside the FOV when the top ray of the cone-beam is horizontal. In this case, the cross-phantom is only in the FOV for a subset of the total number of projections.

ROIs were drawn on the outermost spheres as well as the central sphere to determine SNR for each of the respective regions. This was done because it is known that there is a significant difference in image quality between the outside and inside of the reconstructed slice.

Coronal reconstructions are provided in Figure.3. Qualitatively, we can see that the saddle acquisition has both reduced image quality as well as increased distortion in the planes above the horizontal field of view. This can be attributed to the fact that these areas are under-sampled compared to the circular acquisition where the spheres are in the FOV for every projection. It is apparent that artifacts in the under-sampled Saddle reconstructions indicate differences between spheres in a vertical alignment versus spheres in a horizontal alignment. To illustrate this and show it quantitatively, profiles were drawn through lines indicated by hash marks in Figure.3. Horizontal profiles were drawn from center to outer spheres for both the VAOR and Saddle orbits. Figure.4 illustrates a degree of distortion of the spheres. Note that the profile values increase from center to outside for both VAOR and Saddle in the horizontal case. Next, vertical profiles were drawn from the center to outer spheres for both the VAOR and Saddle orbits (Figure.4 bottom). In addition to a

degree of distortion seen qualitatively in the spheres for the Saddle orbit, it is interesting to note that, while the profile values increase from center to outside for VAOR, they decrease for Saddle.

Given the relatively large difference in appearance between spheres in the horizontal direction and spheres in the vertical direction for the Saddle orbit, SNR measurements were obtained by grouping SNRs based on radius and direction. The following groups of spheres were used for SNR measurements: (1) the outer pair of spheres in the horizontal direction; (2) the outer pair of spheres in the vertical direction; (3) the middle pair of spheres in the horizontal direction; (4) the middle pair of spheres in the vertical direction;. These are denoted as (Outer – H), (Outer – V), (Middle – H), and (Middle – V), respectively, in Figure.5. A number of observations can be made from this figure: (1) SNR is reduced for the Saddle orbit versus VAOR in all cases; (2) SNR error bars are generally equal to or larger for Saddle than for VAOR (except for Middle – V). Table.1 provides SNR percent changes for Saddle versus VAOR. SNR for the Saddle orbit is reduced by 30-48% in the outer spheres, and 4 to 55% in the middle spheres. The overall SNR reduction is 34%.

Although SNR is reduced significantly in most cases, results indicate that additional volumes can be obtained closer to the chest wall, with the spheres readily visible where they would not have been at all visible without the complex orbit. This additional volume is complex in shape and dependent on the particular orbit. The maximum additional sampled depth ranges from approximately 5.1cm at the circumference of the breast at maximum tilt to nearly zero near the center of the breast.

It should be noted that a more desirable setup would have been to include multiple cross-phantoms within the breast phantom cup with VAOR and Saddle acquisitions. In this way, the additional breast volume sampled could be more thoroughly evaluated and the SNR effect simply due to Saddle versus VAOR could also be evaluated (Figure.6). Because of having only a single phantom available, the breast cup had to be moved for this investigation. Nevertheless, previous studies in this Chapter have confirmed that Saddle and VAOR, under conditions of no truncation,

perform equally well. Therefore, the SNR reduction experienced in this study can largely be attributed to truncation alone.

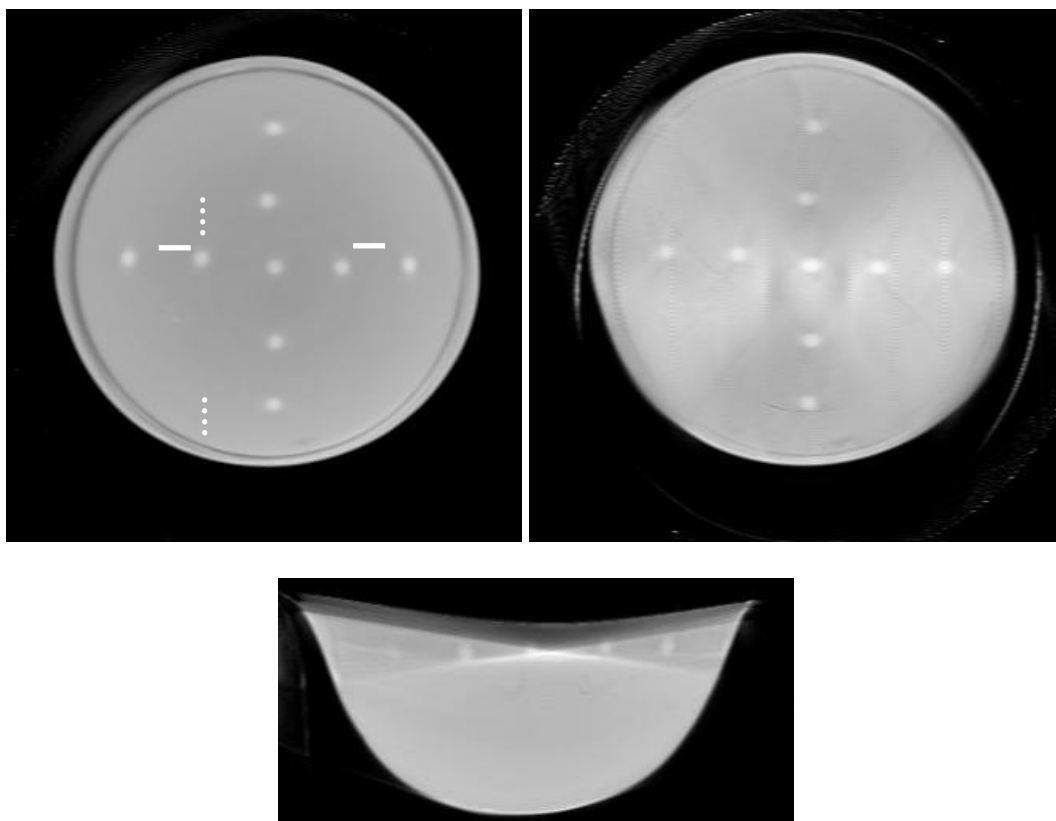


Figure.3 (top row) Coronal views of acrylic cross phantom in oil (10 iterations, 8 subsets, 4x4 binned projections) acquired with (top left) VAOR orbit and spheres fully within field of view, and (top right) Saddle orbit where spheres were not in field of view when system was horizontal without tilt. (bottom) Sagittal view for Saddle orbit indicates additional volume sampled and visibility of spheres even though they were out of FOV initially without tilt. White solid hash marks indicate where horizontal profiles in Figure.4 were obtained and white dashed hash marks indicate where vertical profiles were obtained.

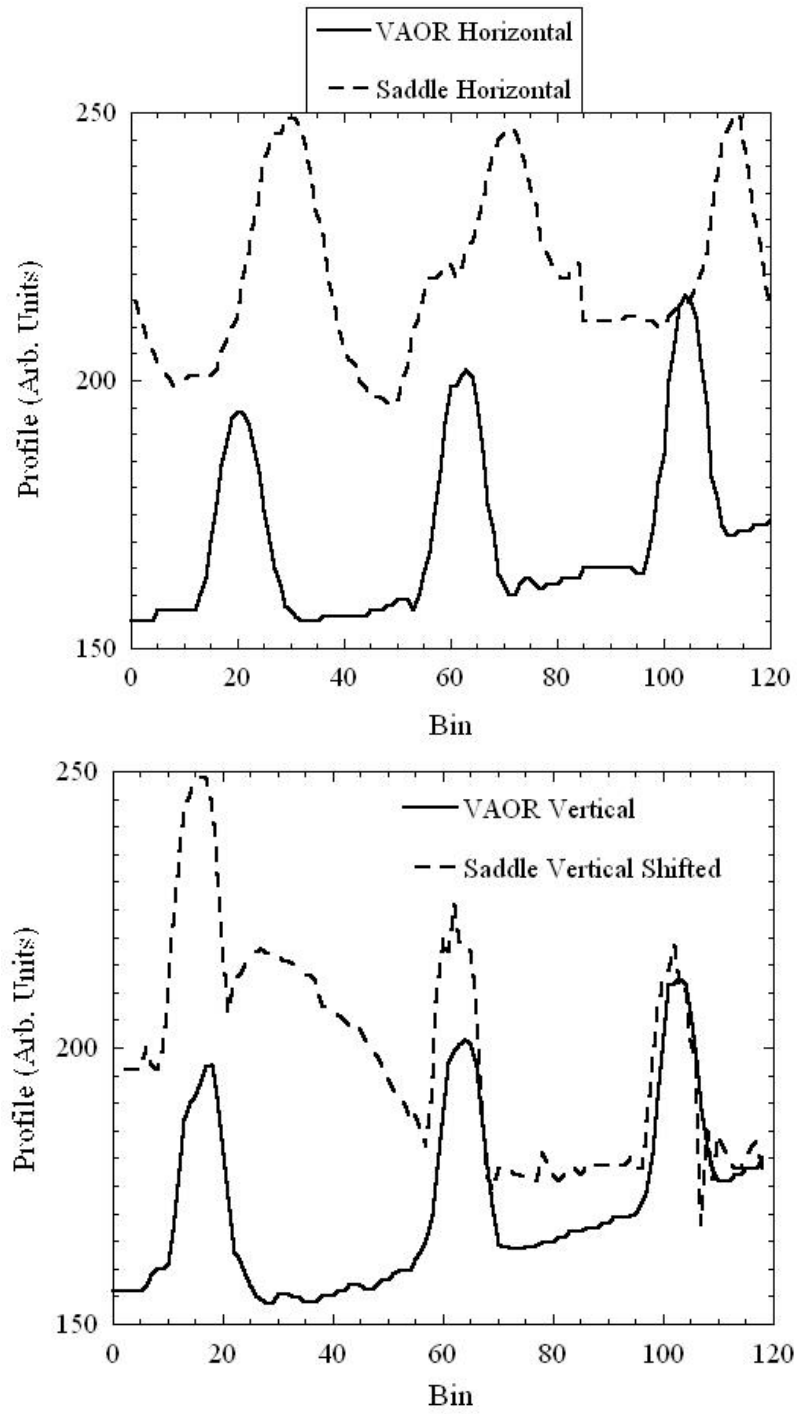


Figure.4. (top) Profile drawn through horizontal line from center to outside sphere for VAOR and Saddle, and (bottom) vertical line from center to outside sphere for VAOR and Saddle. Profiles are drawn through white hash marks indicated in Figure.3.

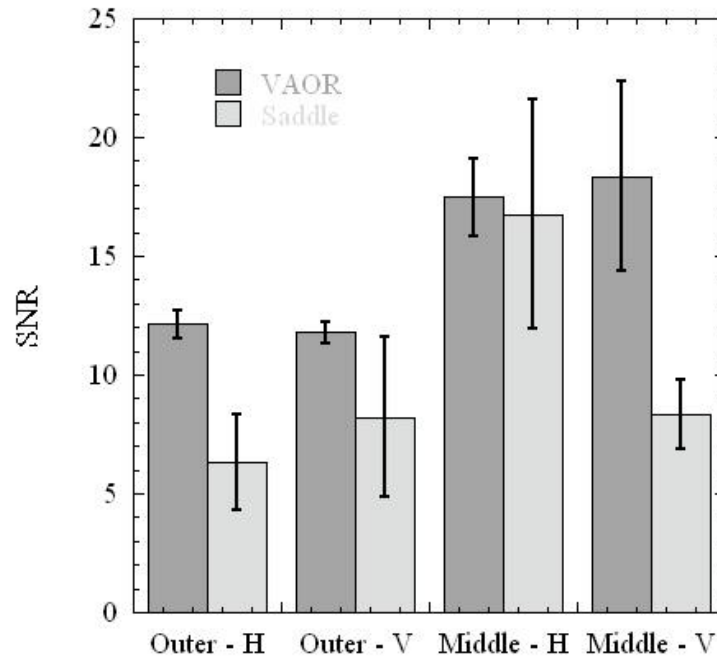


Figure.5. SNR results for VAOR (with the cross phantom entirely within the FOV for all projections) versus Saddle (where the phantom is outside the FOV for the horizontal top ray of the cone-beam) for the outermost horizontal (Outer – H), outermost vertical (Outer – V), middle horizontal (Middle - H), and middle vertical (Middle – V) spheres. Iterative reconstructions of acrylic cross phantom in oil used 10 iterations, 8 subsets, 4x4 binned projections.

Table.1 Percent reduction in SNR for Saddle versus VAOR acquisition.

Set	% change in SNR
Outer – H	-48
Outer – V	-30
Middle – H	-55
Middle – V	-4
Overall	-34

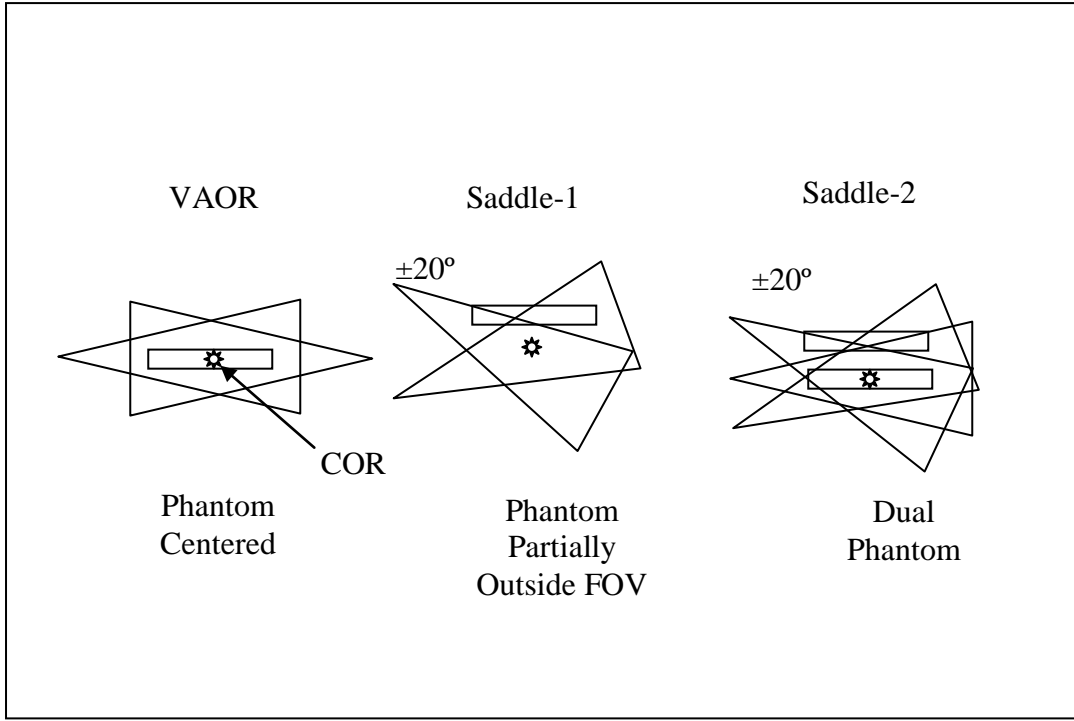


Figure.6. Schematic illustrating (left) placement of cross phantom at COR for VAOR orbit (fully within FOV for all projections), (middle) phantom placed away from COR outside of FOV when top ray of cone-beam is horizontal (and therefore partially within FOV when central ray is horizontal), and (right) ideal placement of dual cross phantom for comparison measurements with a single acquisition.

Discussion and Conclusions

Complex 3D cone-beam orbit acquisitions can be effectively implemented on a novel dedicated transmission computed mammotomography (CmT) system to image relatively large, pendant, uncompressed breasts. Simple circular acquisitions fail to meet Tuy's data sufficiency condition except on the central plane, thus resulting in (severe) object distortion and image artifacts. The complex orbit investigated in this work (Saddle) effectively overcomes that distortion and significantly reduces artifacts. Image results from rods-in-air and air-rods-in-acrylic resolution-frequency phantoms indicate that resolution is not negatively affected by use of complex acquisitions. It may indeed make the resolution more uniform throughout the breast volume. Very recently, this has been validated with detailed 3D MTF measurements of the CmT image volume.⁷⁹ Therefore, the developed CmT system appears to be able to perform complex acquisitions within an

infinite number of possible orbits in a banded region about the sampling sphere that will aid in satisfying Tuy's sampling condition without degradation of resolution.

Breast phantom results indicate that the 3D tilt capability of our system can produce complex orbits that can be used to image closer to the chest wall in dedicated breast imaging, thereby reducing limitations encountered by patient's physical contours and currently unavoidable x-ray tube and digital detector "dead" zones near their edges. Subsequent cross phantom studies show that lesion information may be obtained in areas otherwise outside of the FOV, although imaged quality, in terms of SNR and distortion, is significantly affected. However, it remains to be seen whether this information will be enough to be worthwhile on its own for the low contrast imaging case without additional means of getting in closer proximity to the chest wall. An observer study would be required to find if this is a problem.

Appendix D

Coauthor

SPIE 2006 Medical Imaging Conference – presented by Priti Madhav - San Diego, February, 2006.

A Novel Method to Characterize the MTF in 3D for Computed Mammotomography

Priti Madhav^{1,2}, Randolph L. McKinley^{1,2}, Ehsan Samei^{1,2,3},
James E. Bowsher⁴, Martin P. Tornai^{1,2}

¹ Department of Radiology, Duke University Medical Center, Durham, NC

² Department of Biomedical Engineering, Duke University, Durham, NC

³ Department of Physics, Duke University, Durham NC

⁴ Department of Radiation Oncology, Duke University Medical Center, Durham, NC

ABSTRACT

A novel phantom has been developed to measure the modulation transfer function (MTF) in 3D for x-ray computed tomography. The phantom consists of three tungsten wires, positioned nearly orthogonal to each other. Simultaneous measurements of the MTF are taken at various locations along the three orthogonal reconstructed planes. Our computed mammotomography (CmT) system uses a Varian Paxscan 2520 digital x-ray detector which can be positioned anywhere in $\sim 2\pi$ steradian band and can have arbitrary trajectories. With a half-cone beam geometry and with the phantom positioned near the center of rotation, projection images are acquired over 360 degrees. Various 3D orbits are evaluated including vertical axis of rotation and saddle. Reconstructions were performed using an iterative ordered-subsets transmission algorithm on rebinned projection images, using various numbers of iterations. Rotation of reconstructed slices isolated each wire into its own plane. At various locations along the length of each wire, corresponding MTFs were calculated from 1D line spread functions. Through measurement, accuracy of wire method was verified by comparison of the projection MTFs computed from a wire and a standard edge device. Results indicated minor variations in MTF among the three orthogonal planes, which imply a high degree of uniform sampling in the imaged volume. Findings indicate that the phantom can be used to assess the intrinsic image resolution in 3D as well as potential degradative effects of measurements in various media.

Keywords: modulation transfer function (MTF), resolution, line spread function (LSF), computed tomography, tomography, mammotomography, transmission imaging, orbits, iterative reconstruction

1. INTRODUCTION

The modulation transfer function (MTF) is commonly used to measure the resolution properties of an imaging system^{1,2}. MTF quantifies an imaging device in its ability to transfer detail and contrast characteristics from object to image, as a function of spatial frequency. Analysis of the resolution properties of any imaging system can result in recognizing the limitations and assisting to improve the performance of the system. In 2D imaging systems, such as in x-ray radiography, various methods for measuring MTF have been implemented based on edge^{3,5} or slit techniques^{6,7}. However, these techniques do not immediately transfer to 3D tomographic imaging systems, such as computed tomography (CT), and even positron emission tomography (PET), and single positron emission computed tomography (SPECT).

There have been methods developed to measure MTF in 3D^{8,9}. For this work, another method for measuring resolution in 3D is considered. A device was developed to evaluate the MTF in 3D along any point of the length of three nearly orthogonal axes after a single tomographic emission¹⁰ or transmission acquisition. Measurement of the spatial resolution in three dimensions and at various locations throughout the reconstructed 3D volume can be used to assess any spatially variant blur and degradation in image quality due to the intrinsic acquisition components (i.e. wide cone beam angle, focal spot size, detector response), physical object degradative processes (i.e. scatter), and the reconstruction process. This phantom can also be useful for evaluating tomographic imaging systems capable of 3D-trajectories.

Over the past few years, our group has developed a cone-beam transmission computed mammotomography (CmT) system. With the polar tilt capability of the entire system, non-traditional, non-circular 3D orbits are possible with this system, and some have been implemented and evaluated by imaging other geometric and anthropomorphic phantoms¹¹.

¹³. In this study, we measure the MTF in 3D under near ideal very low scatter, and uniform scatter conditions for a subset of previously implemented orbits. This information can then be used to improve overall image quality by deconvolution of any non-stationary effects.

2. MATERIALS AND METHODS

MTF Phantom

A novel phantom¹⁰ was developed to measure the MTF in 3D (Fig. 1). Twelve acrylic rods (side length of 7.8cm) are connected together to shape a box. Three tungsten wires (length of ~11cm) (*Advent Research Materials Ltd*, Oxford, England and *Scientific Instrument Services, Inc*, Ringoes, NJ) are placed within the boxed frame. Each wire is held from a vertex of the cube to its corresponding opposite end slightly away from the vertex. On its corresponding opposite end, the wire is attached to a sliding support which can be moved to position one end of the wire anywhere along the length of the side-rod. Due to the small diagonal offset, the wires are visibly separable in their positions since they do not touch each other near the center.

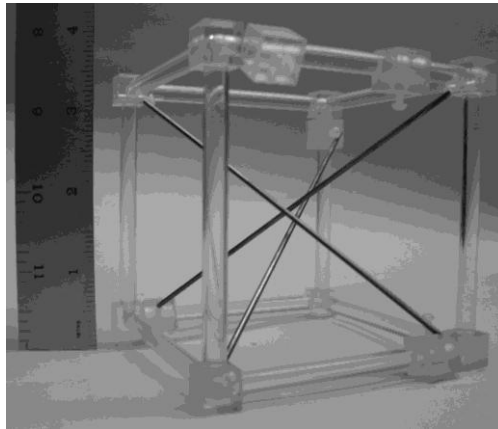


Figure 1: Photograph of acrylic phantom frame with three brass rods used in place of tungsten wires to clearly illustrate the positions of each cord. Cords are visibly separable in their positions such that they do not touch each other near the center.

Data Acquisition

Our dedicated CmT system¹⁴ consists of a rotating tungsten target x-ray source (model Rad-94, 0.4mm focal size, 14° anode angle) (*Varian Medical Systems*, Salt Lake City, UT) and CsI(Tl)-based amorphous silicon digital x-ray detector (*Varian Medical Systems*, Salt Lake City, UT) with grid size of 1920x1536 pixels and 127μpixels. Source and detector are secured to a solid metal plate which is attached to a hemispherical gantry. A Ce ($Z = 58$, $\rho = 6.77\text{g/cm}^3$, K-edge = 40.4keV) (*Santoku America, Inc.*, Tolleson, AZ) 100th value attenuating layer filter was used to produce a quasi-monochromatic beam. The filter was inserted into a custom built collimator attached to the x-ray source. Due to the rotation stage (model RV350CC, *Newport Corp.*, Irvine, CA) and goniometer (model BGM200PE, *Newport Corp.*, Irvine, CA), an infinite number of imaging trajectories can be used such that projection data can be acquired at positions around a pendant uncompressed breast closer to the chest wall than with a simple circular trajectory.

Tube potential was set at 60kVp with a 1.25mAs exposure. Source-to-image distance (SID) used in this set up was 55cm and source-to-object distance (SOD) was 35cm. The phantom was placed near the center of rotation of the unshifted x-ray CmT system. Projection images were collected every 1.5 degrees through a 360 degree azimuthal acquisition for a total of 240 projections. Two orbits were investigated: a simple circular vertical axis of rotation (VAOR), and a saddle with polar tilt ranging from -15° to 15° (Fig. 2). Note that negative polar tilt angle is defined as the x-ray source moving down and detector moving up. These orbits have been used to image some geometric phantoms¹³ but have not been explicitly evaluated for their frequency response characteristics.

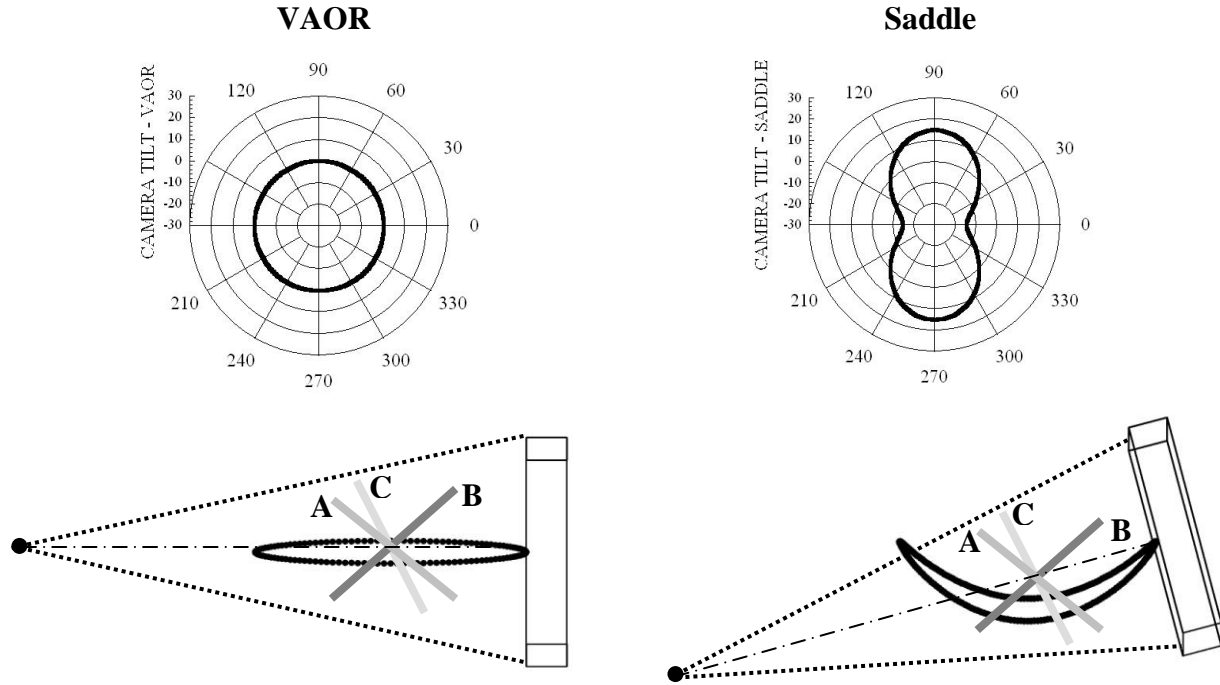


Figure 2: (TOP) Polar plots for VAOR (LEFT) and Saddle (RIGHT) orbits. Polar tilt of the CmT system is defined by the radius of the circle, and azimuth angle is defined around the circumference of the circle. (BOTTOM) 3D setup of the phantom for each orbit. MTF phantom, consisting of three tungsten wires (labeled A, B, C), is suspended and placed near the center of rotation of the system. Black solid line illustrates movement of detector (box) and source (solid circle) for each orbit. Cone-beam boundary is marked by dotted lines and center of rotation is marked by dashed-dotted line.

MTF Phantom Measurements

The MTF was evaluated under (near) ideal conditions by suspending the MTF phantom in air (Fig. 3, LEFT). Tungsten wires, each of a uniform diameter and $\sim 11\text{cm}$ length, were suspended within the boxed frame. Projections of three different wire diameters, $25.4\mu\text{m}$, $50.8\mu\text{m}$, and $125\mu\text{m}$, were acquired. For each imaging condition, the smallest diameter of wire that was observed in the reconstructed images was used to calculate the MTF.

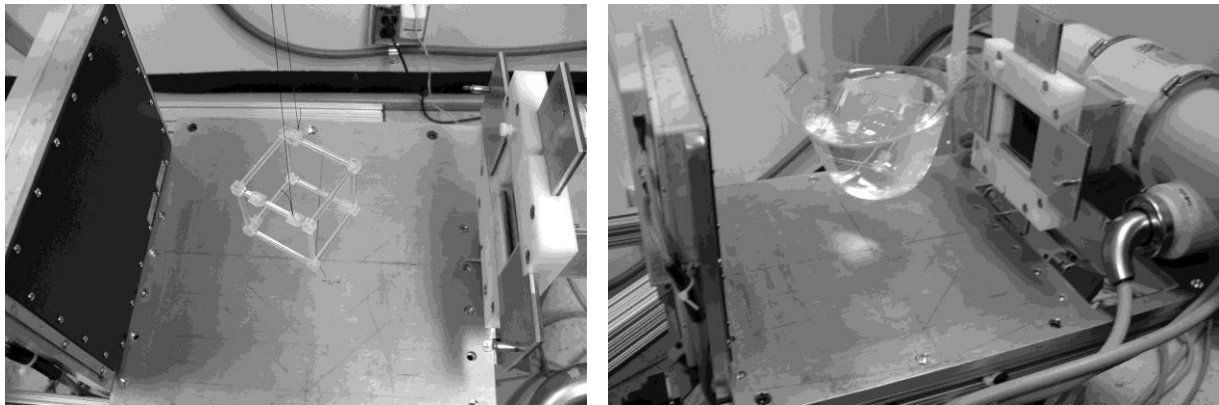


Figure 3: (LEFT) Photograph of the MTF phantom suspended in air to simulate ideal conditions with minimal scatter. (RIGHT) Photograph of the MTF phantom immersed in a non-uniform breast-shaped container with uniform scatter media (mineral oil). In both cases, object is placed near the center of rotation of the CmT system, where the x-ray source is on the right and digital flat panel detector is on the left.

Scatter effects on MTF were also measured by placing the wire-box phantom in a 1350mL uniformly filled breast phantom (nipple-to-chest distance of 11cm, medial-lateral distance of 17cm, and superior-inferior distance of 18cm) (Fig. 3, RIGHT). MTF measurements were done with breast filled separately with mineral oil and water. As in air,

projections of different wire diameters (25.4 μ m, 50.8 μ m, and 125 μ m) were acquired. The smallest diameter of wire that was seen in the reconstructed images was used in calculating the MTF.

Image Reconstruction

Image reconstruction was performed using a ray-driven, iterative ordered-subsets transmission algorithm (OSTR)^{13,14}. Projection images were corrected for gain and offset and binned to 4x4 pixels. Reconstruction parameters were set to 10 iterations (unless otherwise noted), 8 subsets, and 350x350x384 reconstruction grid (unless otherwise noted) yielding a voxel size of 508 μ m³ (unless otherwise noted).

Algorithm to Determine MTF

Reconstructed images were manually rotated to isolate each wire onto its own plane. To determine the MTF, we followed an algorithm presented in a previous paper³, having been successfully applied in 3D SPECT imaging¹⁰. The image of the isolated wire was detected using Sobel edge detection method¹⁵. The Radon transform was applied to the image of the detected line. The point at maximum intensity resulting from this transform determined the final angle and position of the line. The accuracy in estimating the rotation angle is critical to the accuracy of the MTF measurement. Based on the calculated angle, the image was reprojected onto a one-dimensional array perpendicular to the wire and binned into 0.3 subpixel bins to obtain the line spread function (LSF). In order to reduce noise, LSF was smoothed by averaging neighboring pixels within a three pixel moving average window. Corresponding MTFs were calculated by taking the absolute value of a one-dimensional discrete Fourier transform of the LSF and normalizing its value to one at zero spatial frequency.

The accuracy of the wire method was also determined by comparing it to the edge method with a standard edge device. *xSpect* simulation code (developed in the X-ray Imaging Research Laboratory at *Henry Ford Health System*) was used to generate a line profile under ideal absorption and scatter free conditions. These simulation measurements were used to determine the input MTF value and correct the measured MTF of the projection of a wire.

3. RESULTS AND DISCUSSION

Keywords: Comparison of Wire and Edge Technique

The accuracy of the algorithm used in this study is first verified by comparing MTF of a projection of a wire with diameter of 25.4 μ m and a standard edge device. Fig. 4 shows that there is a slight difference between the MTF of wire and edge. The calculated root mean square difference (RMSD) between the two MTF curves is 0.017 and the absolute difference is 0.020 at 2 cycles per mm.

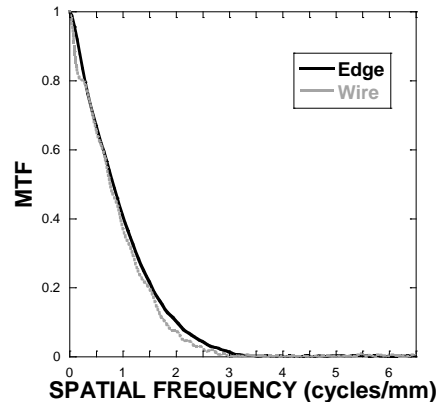


Figure 4: Comparison of MTF between a wire (diameter of 25.4 μ m) and an edge. Similar MTFs were measured for both methods verifying the use of the wire method for quantifying resolution in 3D (RMSD = 0.017).

Note that for a projection of a wire there is magnification, while the edge, being measured on the surface of the detector, has little to no magnification. However, when the cone beam projections are reconstructed, the effect of magnification seen in projection space is removed.

Keywords: MTF Measurement Along Line at Various Locations

Fig. 5 shows a 3D rendered image of the reconstructed MTF phantom suspended in air. Projection images were collected using the VAOR orbit. A wire thickness of $50.8\mu\text{m}$ was the smallest size that could be seen in the reconstructed images. The wires are orthogonal to one another and do not touch each other.

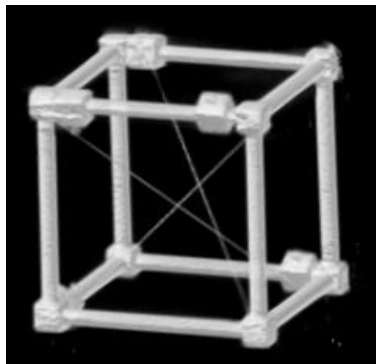


Figure 5: 3D rendered image of phantom with three tungsten wires (diameter of $50.8\mu\text{m}$) suspended in air and acquired using VAOR.

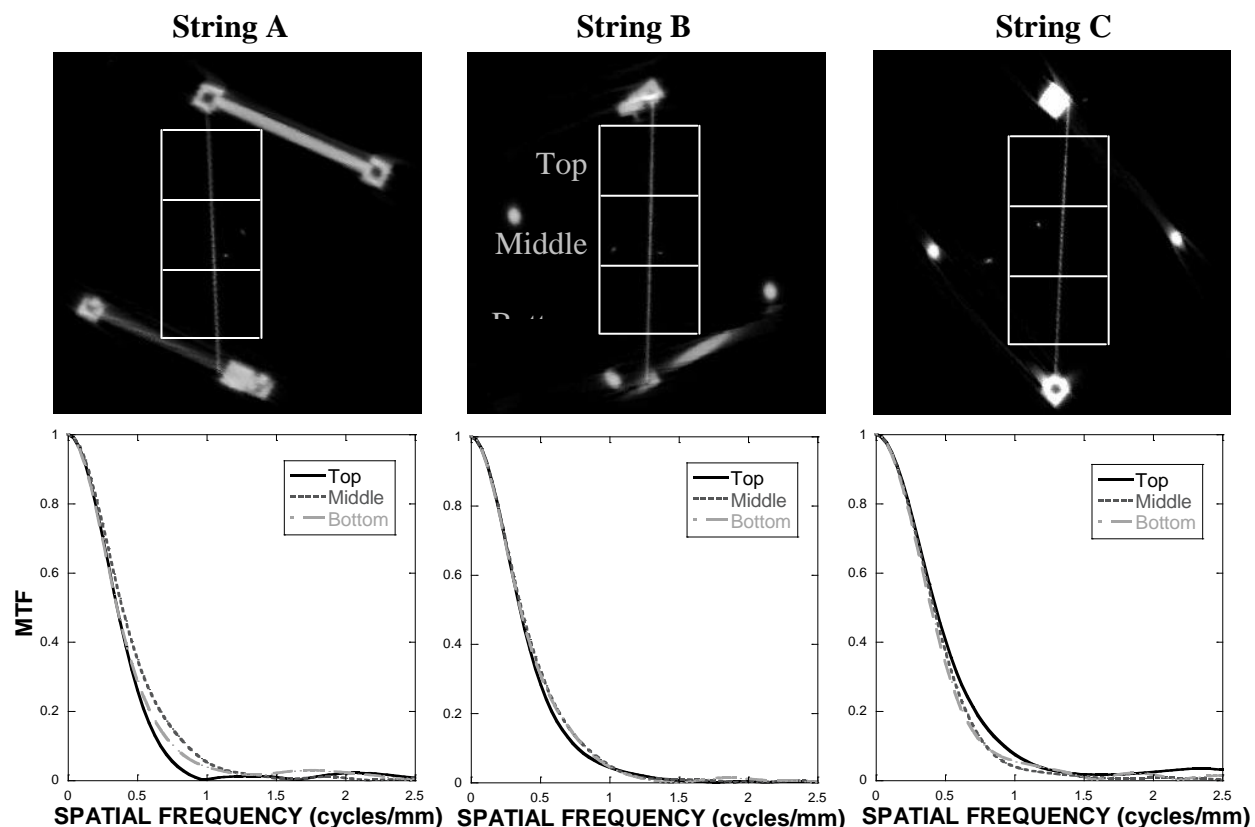


Figure 6: (TOP) Reconstructed image slice of each tungsten wire acquired using VAOR. The angle of the wire, calculated using the Radon transform, was used to reproject the image and obtain the LSF. (BOTTOM) The MTFs were obtained by taking the discrete Fourier transform of the LSF. Results show little variation in MTF measured along the line over a few regions. However, the measured MTF of the top part of Wire A slightly deviates from the other two parts.

The MTF was determined along various portions of each of the three tungsten wires, from images collected of the phantom in air using a VAOR trajectory. Fig. 6 shows minor variation in MTF along different locations of each wire. Wire A shows slightly more variation than the other two wires. The MTF measured at the top part of Wire A appears to have slightly worse resolution than the other two parts. RMSD between the top and middle part is 0.040 while the RMSD between the middle and bottom part is 0.027. At 1 cycle per mm, the absolute difference of the measured MTF between top and middle is 0.051 while between the middle and bottom it is 0.015. An average MTF of all three wires

was also calculated along with the standard deviation to illustrate the small variations and uniform 3D resolution throughout the reconstructed volume (Fig. 7).

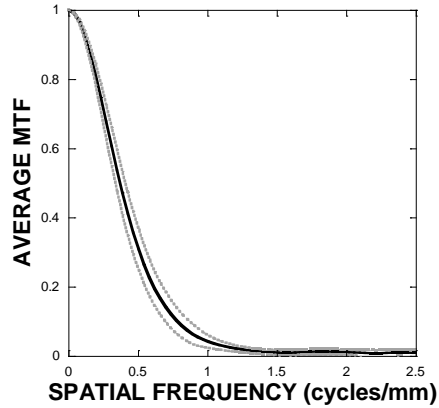


Figure 7: Average MTF (solid line) measured at different locations for all three wires. There is not much variation (dotted line) in MTF throughout the reconstructed measured image volume.

Keywords: MTF Measurement with Complex 3D orbit

Besides VAOR, a Saddle trajectory was also evaluated. Results are shown in Fig. 8. There are small variations in MTF for the Saddle trajectory as well. Fig. 9 shows an average MTF measured for Saddle orbit. Similar to the VAOR orbit, there is not much deviation among the MTF measurements at different segments along all three tungsten wires. This result corroborates our previous qualitative study which also showed no degradation in image resolution between VAOR and Saddle orbits¹³.

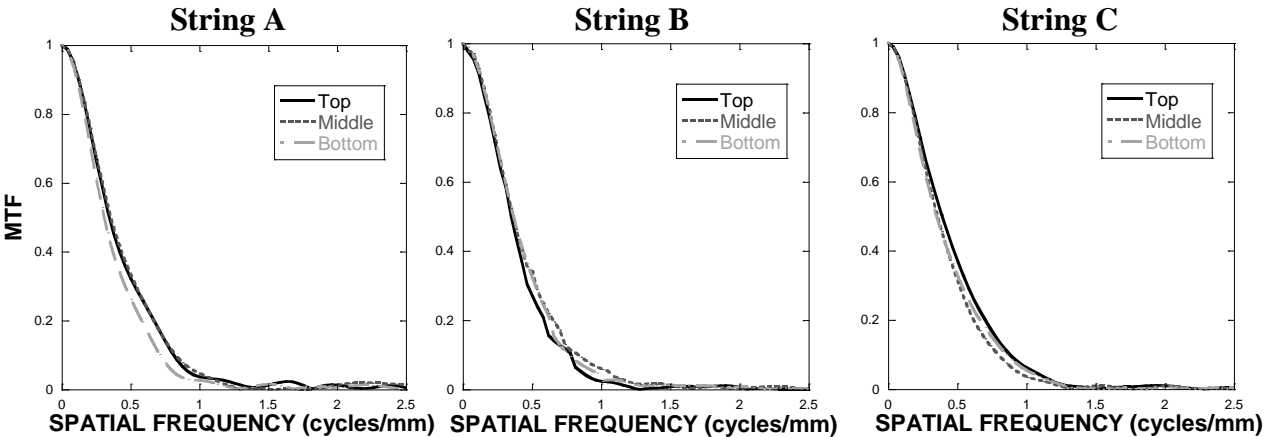


Figure 8: MTF evaluated at different positions along the length of the wire obtained from reconstructed images of a Saddle trajectory acquisition. Very slight variation among the different locations for each line is seen.

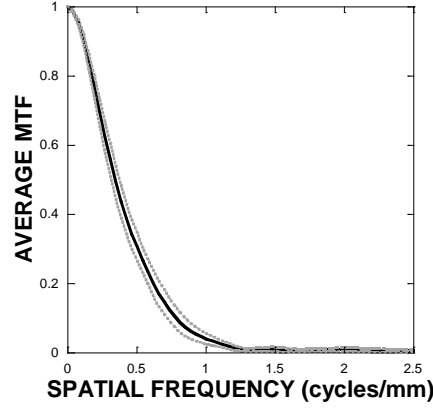


Figure 9: Average MTF (solid) measured at various parts for all three tungsten wires for Saddle orbit. Small standard deviation (dotted) from the mean illustrates the little variation among the measurements.

Previous study¹³ has shown significant streaking and distortion in images of a symmetric phantom obtained using VAOR orbit. Saddle orbit showed reduced artifacts due to complete sampling. However, streaking and distortion effects were not seen in the average MTF. Measured MTF of Wire A using VAOR orbit (Fig. 6, BOTTOM LEFT) showed more variation in different areas along the length of line than the measured MTF of Wire A using Saddle Orbit (Fig. 8, BOTTOM LEFT). RMSD between the top and middle part was calculated to be 0.009 and RMSD between middle and bottom part was 0.025. At 1 cycle per mm, the absolute difference of the measured MTF between top and middle is 0.010 while between the middle and bottom it is 0.014.

Keywords: MTF Measurement with Various Reconstruction Parameters

Using an accurate model that incorporates scatter, spatial resolution effects, etc., iterative reconstruction such as OSTR (ordered subsets transmission tomography) can converge to an optimal solution and improve image quality. Current study for computed mammotomography imaging of breast lesions has shown an optimal stopping point to be at the 10th iteration¹⁶. Beyond the 10th iteration, contrast continues to improve but along with a decrease in SNR.

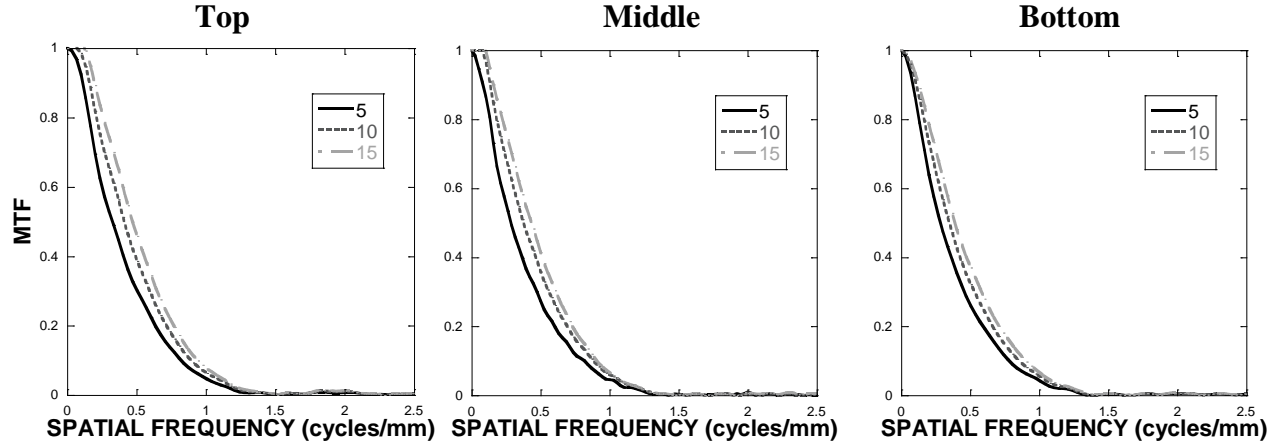


Figure 10: MTF measured at 5th, 10th, and 15th iteration images of a single tungsten wire (C) at various locations (Top, Middle, Bottom) for Saddle orbit. There is a resolution improvement between 5th and 10th iteration but slightly less of an increase at higher iterations.

A similar result was found by measuring the MTF at each iteration of the reconstructed image obtained using Saddle orbit. Fig. 10 shows the MTF at 5th, 10th, and 15th iteration along a single wire. At all three positions along a tungsten wire, there is a clear enhancement in MTF between the 5th and 10th iteration. However, a slight increase exists in MTF between the 10th and 15th iteration confirming that resolution and contrast will continue to improve at a slower rate beyond 10 iterations. Table 1 lists RMSD and absolute difference values for the top, middle, and bottom segment of Wire C at each of the three iterations. Both values show a higher increase from 5th to 10th than 10th to 15th. To preserve SNR, setting OSTR to run up to 10 iterations is enough to generate an ideal reconstructed image set.

Table1: RMSD and absolute difference (at 0.5 cycle/mm) values along top, middle, and bottom segment of tungsten wire C at 5th, 10th, and 15th iteration

	RMSD			ABSOLUTE DIFFERENCE		
	<i>TOP</i>	<i>MIDDLE</i>	<i>BOTTOM</i>	<i>TOP</i>	<i>MIDDLE</i>	<i>BOTTOM</i>
5TH TO 10TH	0.046	0.044	0.041	0.096	0.095	0.073
10TH TO 15TH	0.026	0.029	0.021	0.053	0.053	0.048

Due to limitations in processor speed and memory capacity, our current reconstruction code accommodates full projection images that are 4x4 binned from the full frame dataset and reconstructed at a limited grid size. Without these restrictions, our CmT system could generate reconstructed images with higher resolution as shown in Fig. 11. Projection images were binned to 2x2 and cropped to make an overall smaller subset of the projection data. As can be seen, MTF greatly improves with linear sampling by approximately a factor of 2.

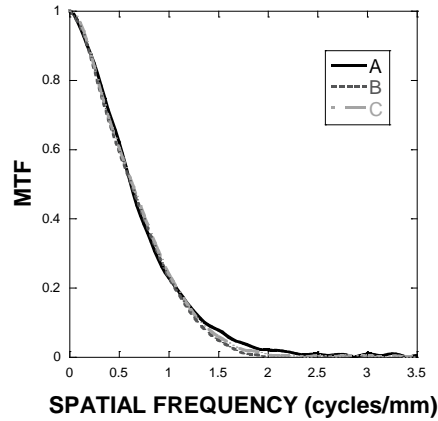


Figure 11: MTF measured in the middle of each of the three tungsten wires from projection images binned to 2x2 and cropped. MTF can increase by close to a factor of 2 without computer limitations. Reconstructions performed at 350x350x300 grid size and 254 micron pixel sizes.

Keywords: MTF Measurement in Different Media

The MTF was determined for the phantom placed in a uniform mineral oil-filled and water-filled breast phantom (Fig. 3, RIGHT). With the addition of a scatter component, a wire thickness of 125 μ m was the smallest diameter that could be clearly seen in the reconstructed images. For both cases, there is minimal difference in MTF at various locations along the length of each wire (Fig. 12). Due to contribution of scatter and the reconstruction process, MTFs measured in oil and water are expectedly slightly worse than what was measured in air.

One of the main advantages of using the Saddle orbit is to avoid physical features of the torso above a suspended breast and still be able to completely sample the breast volume. Even in scatter media, our CmT system is able to provide a fairly uniform 3D resolution in the breast volume of interest.

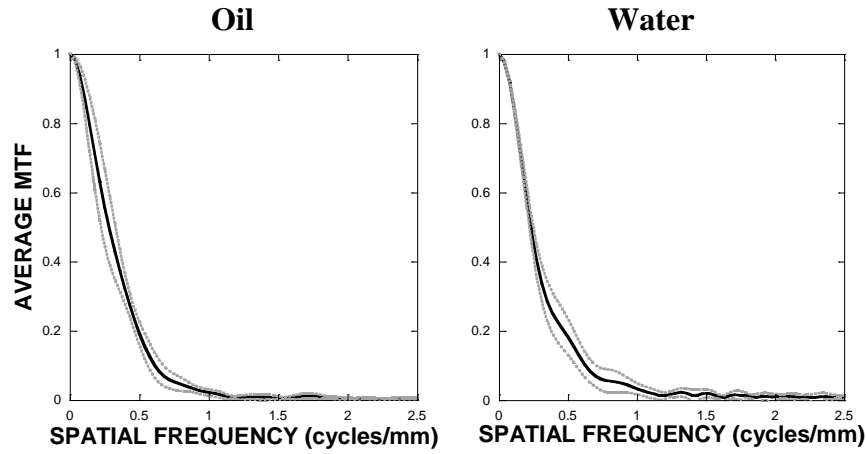


Figure 12: Average MTF Measurement in (LEFT) oil and (RIGHT) water at all three different locations of Wires A, B, and C. Mineral oil which is similar to glandular tissue in the breast has similar variation along different spatial frequencies. However, water which induces more scatter than mineral oil shows more variation at higher spatial frequencies.

4. CONCLUSION

In this work, we developed a novel phantom to measure the MTF in 3D for computed tomography. This phantom was tested on our computed mammotomography system using a quasi-monochromatic cone beam source, flat panel detector, and an iterative statistical reconstruction algorithm. Measurements with this phantom provide insight into resolution effects caused by system design, detector-source trajectories, reconstruction algorithms, and scatter. Our initial study shows that both VAOR and Saddle orbits do not yield large differences in resolution in a $\sim 8 \times 8 \times 8 \text{ cm}^3$ volume. This is somewhat counter-intuitive, and a more comprehensive frequency-space sampling study would be required to determine the reasons for this. The MTF can improve with increased reconstruction iterations but reach an optimal point where there is no great change in resolution and contrast. Limitations in processor speed and memory capacity also limit reaching finer reconstructed resolutions. Orbits, such as Saddle, that uniformly sample the breast volume of interest yield a uniform 3D resolution even in scattering media. In conclusion, this novel phantom can provide knowledge of 3D resolution of any imaging system, and thereby help improve performance characteristics of the system.

ACKNOWLEDGEMENTS

This work was supported by NIH R01-CA096821, and in part by DOD W81XWH-05-1-0280, and NIH EB001040-01.

REFERENCES

1. K. Rossman, "Point spread-function, line spread-function, and modulation transfer function", *Radiology* **93**, 257-272 (1969).
2. M.L. Giger and K. Doi, "Investigation of basic imaging properties in digital radiography. 1. Modulation transfer function", *Med. Phys.* **11** (3), 287-295 (1984).
3. E. Samei and M.J. Flynn, "A method for measuring the presampled MTF of digital radiographic systems using an edge test device", *Med. Phys.* **25** (1), 102-113 (1998).
4. P.B. Greer and T. van Doorn, "Evaluation of an algorithm for the assessment of the MTF using an edge method", *Med. Phys.* **27** (9), 2048-2059 (2000).
5. E. Buhr, S. Günther-Kohfahl, and U. Neitzel, "Accuracy of a simple method for deriving the presampled modulation transfer function of a digital radiographic system from an edge image", *Med. Phys.* **30** (9), 2323-2331 (2003).
6. H. Fujita, D. Tsai, T. Itoh et al., "A simple method for determining the modulation transfer function in digital radiography", *IEEE Trans. Med. Imag.* **11** (1), 34-39 (1992).
7. J.M. Boone, "Determination of the presampled MTF in computed tomography", *Med. Phys.* **28** (3), 356-360 (2001).
8. M.J. Flynn, D.A. Reimann, and S.M. Hames, "Measurement of noise and resolution in x-ray computed microtomograms", *1994 Proc. SPIE: Phys. of Med. Imag.* **2163**, 192-198 (1994).
9. D.A. Reimann, M.J. Flynn, and S.M. Hames, "Direct measurement of resolution in volumetric imaging systems", *1994 IEEE NSS/MIC Conference Record*, 1784-1787 (1994).

10. P. Madhav, C.N. Brzymialkiewicz, S.J. Cutler et al., "Characterizing the MTF in 3D for a Quantized SPECT Camera Having Arbitrary Trajectories Using a Novel Phantom", *2005 IEEE NSS/MIC Conference Record*, 1722-1726 (2005).
11. C.N. Archer, M.P. Tornai, J.E. Bowsher et al., "Implementation and initial characterization of acquisition orbits with a dedicated emission mammotomograph", *IEEE Trans. Nucl. Sci.* **50** (3), 413-420 (2003).
12. C.N. Brzymialkiewicz, M.P. Tornai, R.L. McKinley et al., "3D data acquisition sampling strategies for dedicated emission mammotomography for various breast sizes", *2004 IEEE NSS/MIC Conference Record*, 2596 - 2600 (2004).
13. R.L. McKinley, C.N. Brzymialkiewicz, P. Madhav et al., "Investigation of cone-beam acquisitions implemented using a novel dedicated mammotomography system with unique arbitrary orbit capability", *2005 Proc. SPIE: Phys. of Med. Imag.* **5745**, 609-617 (2005).
14. M.P. Tornai, R.L. McKinley, C.N. Brzymialkiewicz et al., "Design and development of a fully-3D dedicated x-ray computed mammotomography system", *2005 Proc. SPIE: Phys. of Med. Imag.* **5745** (1), 189-197 (2005).
15. Jae S Lim, *Two-Dimensional Signal and Image Processing*. (Prentice Hall, Englewood Cliffs, NJ, 1990).
16. R.L. McKinley and M.P. Tornai, "Preliminary investigation of dose for a dedicated mammotomography system", Presented at *2006 SPIE: Phys. of Med. Imag. Conference*, San Diego, California, 2006.

Appendix E

Coauthor

SPIE 2007 Medical Imaging Conference – presented by Dominic Crotty - San Diego, February, 2007.

Investigating Novel Patient Bed Designs for Use in a Hybrid Dual Modality Dedicated 3D Breast Imaging System

Dominic J. Crotty^{1,2}, Priti Madhav^{1,2}

Randolph L. McKinley¹, Martin P. Tornai^{1,2}

¹Department of Radiology, Duke University Medical Center, Durham, NC 27710

²Department of Biomedical Engineering, Duke University, Durham, NC 27708

ABSTRACT

A hybrid SPECT-CT system for dedicated 3D breast cancer imaging (mammothography) is in development. Using complex 3D imaging acquisition trajectories, the versatile integrated system will be capable of contouring and imaging an uncompressed breast suspended in a 3D volume located below a radio-opaque patient bed, providing co-registered volumetric anatomical and functional information. This study examines tradeoffs involved in the design of the patient bed to satisfy concomitant and competing technical and ergonomic requirements specific to this imaging paradigm. The complementary source-detector arrangement of the CT system is geometrically more restrictive than that of the single detector SPECT system. Additionally, the compact dimensions and size of the CT system components (primarily the x-ray tube) are key constraints on the bed design and so the focus is concentrated there. Using computer-aided design software, several design geometry options are examined to simultaneously consider and optimize the following parameters: image magnification, imaged breast volume, azimuthal imaging span, and patient comfort. Several CT system source to image distances are examined (55-80cm), as well as axial patient tilt up to 35°. An optimal patient bed design for a completely under-bed hybrid imaging system was determined. A 60cm SID, magnification factor of ~1.5, and patient bed angled at ~15° provided the optimal dimensions. Additional bed dimensions allow the CT projection beam to nearly entirely image the chest wall, however at the cost of reduced angular sampling for CT. Acquired x-ray mammothographic image data is used to assess the feasibility of this reduced angle acquisition approach.

Keywords: Mammothography, SPECT, CT, dual modality, flat panel detector, breast imaging, 3D

1. INTRODUCTION

Our lab has developed and optimized individual SPECT and CT systems dedicated to breast cancer imaging [1-5]. A combined dual modality imaging system using the individual systems has recently been assembled [6,7]. To further develop the system as a clinical imaging device, it is necessary to design a patient bed that simultaneously allows imaging close to the chest wall with both modalities and also provides the patient with physical comfort for the duration of the dual-modality procedure, which may take approximately 10 minutes for each breast.

The concept for this new combined imaging system includes a patient lying prone on the bed with her breast protruding down through a centered hole in the bed without compression. The imaging system acquires dual modality tomographic images of her breast beneath the bed using simple or complex 3-dimensional trajectories. This approach to dedicated breast imaging is also used in other similar imaging modalities [8-12], as well as commercially available breast MRI. By not using breast compression, tissues in the pendant breast are naturally spread farther apart and the breast is not distorted. For SPECT and CT imaging, the pendant breast hangs away from the torso of the prone patient, which should minimize both contamination of signals from the patient's torso and any scattered x-ray dose back into the torso.

The bed should avoid collision between the patient and imaging system whilst allowing data to be acquired by any arbitrary orbit within the 3-D hemispherical range of motion. Additionally, the ideal patient bed for prone imaging would maximize comfort for the patient while allowing for imaging 1-2cm into the chest wall of the patient. However, with the

current imaging system, these last two requirements are in competition with each other. Therefore, the challenge in designing this patient bed is to find the optimal operational range where patient comfort is adequate while allowing sufficient chest wall sampling.

2. MATERIALS AND METHODS

2.1 Equipment Used

The cone beam computed mammotomography system (CT) shown in Fig.1 [3-5] is composed of a rotating tungsten target x-ray source (model *Rad-94*, *Varian Medical Systems*, Salt Lake City, UT) housed in a protective housing (model *Sapphire*, *Varian Medical Systems*, Salt Lake City, UT) and a 20x25cm² field of view CsI(Tl)-based amorphous silicon digital x-ray detector (model *Paxscan 2520*, *Varian Medical Systems*, Salt Lake City, UT). A Ce 100th attenuating layer filter ($Z=58$, $\rho=6.77\text{g/cm}^3$, $K\text{-edge}=40.4\text{keV}$, *Santoku America, Inc.*, Tolleson, AZ) is used to shape the spectrum of the beam into a quasi-monochromatic beam yielding a mean energy of $\sim 36\text{keV}$ and FWHM of $\sim 15\%$ [13,14]. The source and detector are at a fixed 60cm source to image distance (SID). Important geometrical considerations include: (1) the dead-zone between the focal spot and the top of the tube housing for the x-ray source ($\sim 8\text{cm}$); (2) the dead-zone between the top of the active imaging plane and the detector housing ($\sim 4.5\text{cm}$) (see ahead to Fig. 3) ; (3) the width of the x-ray source housing of 46.5cm; (4) the detector housing width of $\sim 32\text{cm}$. Fig. 1 (TOP RIGHT) illustrates the CT system in a 3D trajectory around combined anthropomorphic torso and breast phantoms. Note that, unlike the SPECT system, the CT is currently restricted to imaging suspended phantoms and is unable to traverse a full 360° orbit below a standard, flat patient bed (Fig. 2). This indicates that the relatively large dead zones for the source and detector are the primary constraints on the design of the patient bed.

The SPECT system [1,2] uses a compact 16x20cm² field of view Cadmium Zinc Telluride (CZT) gamma camera (model *LumaGEM 3200STM*, *Gamma Medica, Inc.*, Northridge, CA) with 2.3x2.3x5mm³ discretized crystals, on a 2.5mm pitch. The gamma camera is placed on a laboratory jack that changes the radial distance from the camera face to the breast surface. This subsystem is further positioned on a goniometric cradle (model *BGM200PE*, *Newport Corp.*, Irvine, CA) which is itself on a motorized rotation stage (model *RV350CCHL*, *Newport Corp.*, Irvine, CA), thus allowing the SPECT system fully 3-D motion capability below the patient bed. This inherent flexibility to position anywhere in a hemispherical space, as well as the fact that the SPECT gamma camera's line of sight is determined by the front-end collimator and no conjugate or complementary sources/detectors are necessary, eases bed design constraints. Fig. 1 (top, left) illustrates the SPECT system imaging around and below a pendant breast phantom protruding through a hole in a pre-prototype patient bed. The radiopharmaceutical used in these experiments is ^{99m}Tc that emits 140keV gamma-ray photons.

Both systems have been integrated onto a common platform Fig. 1 (bottom). In the initial combined system, the CT and SPECT systems are secured to the same metal plate attached to a common rotation stage. While the SPECT system retains full 3-D motion, the CT system is fixed at a given source to image distance and polar tilt angle (both dimensions to be decided during the bed design process) and is otherwise restricted solely to azimuthal motion.

The final bed design will be attached to a positioning system (C830, *Biodex Medical Systems*, CA) (Fig. 2) that provides 5 motorized degrees of freedom. This robust bed system will allow positioning of the patient's breast relative to the imaging system once the patient is on board.

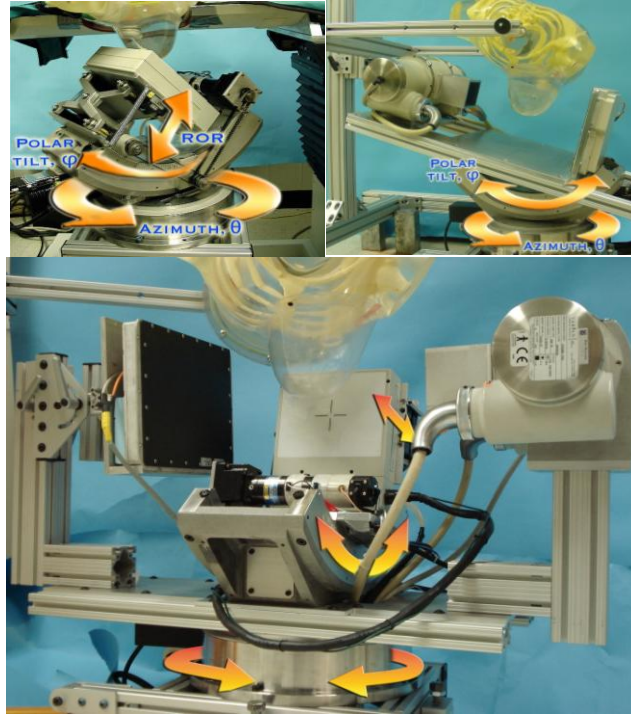


Figure 1. Photographs of the (TOP LEFT) individual SPECT and (TOP RIGHT) CT imaging systems and (BOTTOM) the integrated dual-modality system. Orange arrows indicate direction of sub-system movement. The SPECT system is capable of full 3-D motion in a hemispherical space, and the independent CT system is individually capable of 3-D motion, but in the combined, hybrid system, the CT sub-system is restricted solely to azimuthal motion.

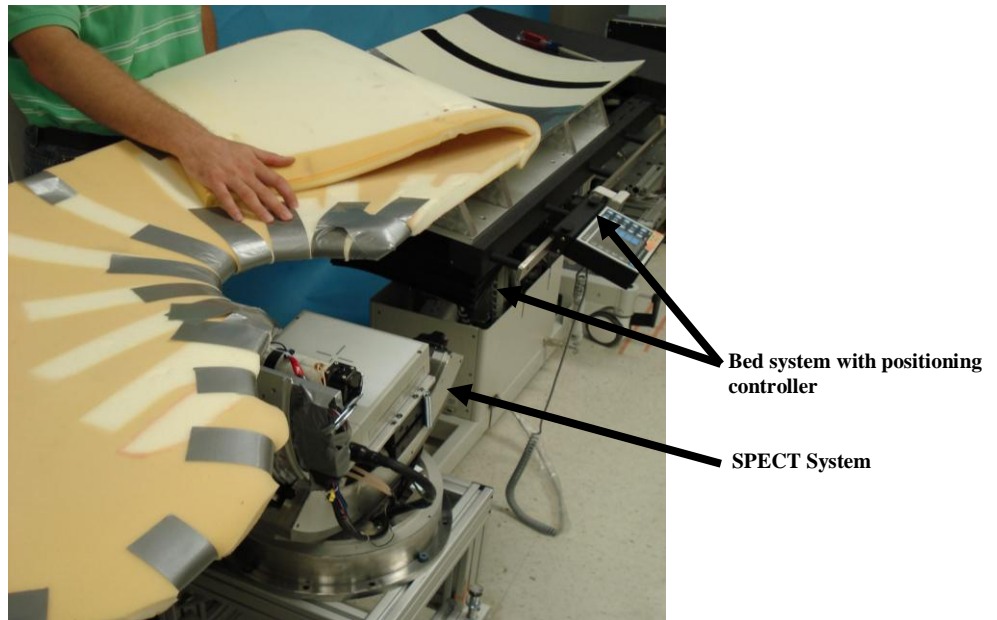


Figure 2. Photograph of an early prototype palette and motorized bed positioning system placed over the SPECT system. The modified patient bed shown in the image has been used for SPECT patient acquisition and will be replaced by the bed design discussed in this paper. The above bed is lined with a $\frac{1}{8}$ " lead shield to reduce emission contamination of the transmission image. Currently, the CT system is unable to traverse around this essentially flat bed due to geometrical constraints.

2.2 Bed Design Method

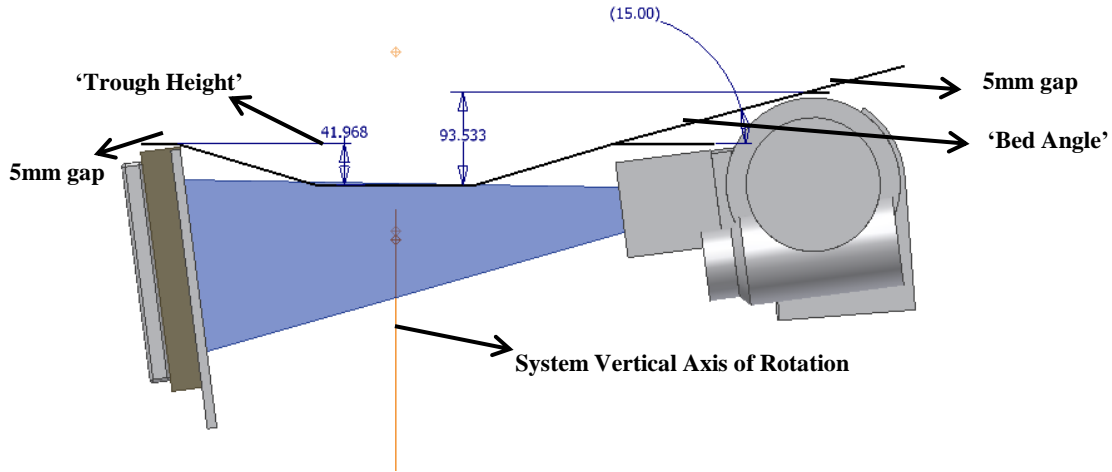


Figure 3. CAD modeled bed design of a 60cm SID and a 15° bed angle. Superimposed on the schematic is the outline of the bed, tailored to allow the source (at left) and detector (at right) to rotate about the noted vertical axis of rotation.

Initially, the x-ray tube, cone beam and detector were modeled at different SIDs (55-80cm) using computer aided design software (*Autodesk Inventor Professional R10*, Autodesk Inc., CA). For each iteration, a modeled large hemispherically shaped breast was placed at varying source to object distances, thus changing image magnification. The total breast volume imaged was calculated by the intersection of the cone beam with the breast, and any nipple truncation in the field of view was noted. A subset of SIDs (55-70cm) was then used to regenerate models of the CT system at varying polar tilt and bed angles (0-20°). Using the design criterion of limiting the gap between the top of the source and detector and the bottom of the bed to 5mm, a skeleton outline of possible bed designs was superimposed on the CT system for each source-detector setup. An image of one such design is shown in Fig. 3. The chest wall of the patient is assumed to begin adjacent to the bottom of the thin bed.

The trough depth was determined as the distance between the plane where the head is placed and the top plane of the x-ray cone beam above the system isocenter. Increased trough height and angle for the patient in the waist area are both assumed to increase patient discomfort and anecdotal evidence strongly suggests that increased patient discomfort leads to a subsequent increase in motion-induced image artifacts in reconstructed breast images.

The CAD models and the generated imaged breast volume and truncation data were used to choose the bed design that was judged to give the best compromise between the ability to image a large breast volume close to the chest wall of the patient, while possessing an acceptably small bed angle. A foam-based prototype design was assembled in the lab and tested by several volunteers.. The shape of the bed was found to be comfortable enough to proceed with the manufacture of a prototype of stainless steel. The bed palette was then integrated onto the positioning system.

2.3 Limited Angle Tomographic Data Acquisition

The combination of the relatively wide x-ray housing with the tiered bed design and its truncated trough height at the head restricts the ability of the system (at a fixed height of the bed above the ground) to rotate and maintain imaging close to the chest wall for a full 360°. In fact, the isoplanar azimuthal imaging range is closer to approximately 250°, as measured relative to the central x-ray axis.

Therefore, 5mm acrylic spheres were arranged in a cross pattern in a disc and used to investigate the impact on data reconstructed from limited tomographic acquisitions. The spheres were regularly spaced approximately 1cm apart in the shape of a cross (Fig. 4). Three such discs were stacked on each other, placed into a plastic anthropomorphic breast phantom and tomographically imaged in air using a full 360° of data at a CT source-detector system polar tilt of 7.5°, equal to the fixed tilt of the system in the integrated system. The discs were spaced so that the effect on the visibility could be observed for tissue near the chest wall and further down into the center of the image. A number of views

corresponding to the range of angles ($\sim 110^\circ$) limited by the bed design were removed from the projection data and reconstructed using an ordered subset transmission reconstruction method with 16 subsets and 5 iterations.



Figure 4. Photograph of the spherical cross pattern phantoms used to observe the effect of limited angle tomographic data acquisition.

3. RESULTS AND DISCUSSION

3.1 Bed Design

The physical dimensions and bilateral nature of the CT imaging system, specifically the large dead zones on both the tube and detector, form the major limiting factor in the design of the bed. This dictates that a tiered bed design is the only practicable solution to allow imaging close to the chest wall. Indeed, one published design for another CT-only system has a flexible support, depending on the patient's ability to bend their back and protrude their breast into the CT system FOV [9]. The approach here is therefore to design a shallow trough as part of the bed into which the patient extends her chest, with the bed also angled at the waist to increase patient comfort and to aid the patient in protruding her torso into the FOV. Additionally, the trough depth is reduced at the head side to improve patient comfort with minimal neck strain.

Figure 5 shows data generated from CAD models of various bed designs of the hemispherical breast volume imaged as a function of CT system source-to-object distance (SOD) and trough height versus bed angle under various system SIDs and SODs. Larger magnifications than 2X increase focal spot blur, truncate the nipple and decrease the imaged breast volume for the assumed detector size. Magnifications less than 1.6X have increased x-ray scatter. Additionally, trough height decreases as SID and bed tilt are simultaneously increased (Fig. 5, right), but increased bed tilt is assumed to correspond to patient discomfort, and a shorter SID is preferable for x-ray source power generation reasons. The ability of the bed design to facilitate imaging close to the chest wall can be visually judged by viewing the accurate CAD models. However, deciding on patient comfort *a priori* is a necessarily subjective decision on the part of the designer.

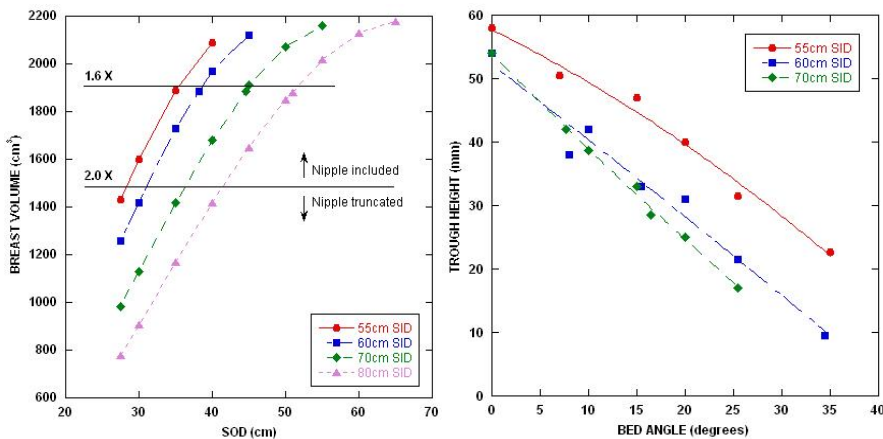


Figure 5. Plots of (LEFT) breast volume imaged versus source to isocenter distance and (RIGHT) trough height versus bed angle for various SIDs. For a 60cm SID and an image magnification of 1.6X, the complete breast volume imaged is $\sim 1900\text{mL}$ with a bed trough height of $\sim 36\text{mm}$.

Considering all the above geometric constraints, a prototype bed was designed (Fig. 6). 60cm was chosen to be the SID for the integrated CT system, with a 38cm source to isocenter distance, thus preserving the same magnification as the prototype 55cm SID system. A bed angle of 15° at the waist was chosen as this was judged to optimize the competing

requirements of chest wall imaging and patient comfort. This resulted in a ~4cm trough depth on the head side and a ~9cm trough depth on the waist side. The trough was octagonally shaped to increase the strength of the bed, provide some patient contouring and provide symmetry for either left or right breast imaging. Large panels were added to the sides of the bed to provide additional comfort and protection for the patient as the mechanical system rotates below her. It also protects the patient and imaging detectors from transmission source scatter and emission source contamination, respectively, for the systems underneath. Lastly, the angled panels increase strength along the bed axis, helping to ensure that the cantilevered bed design does not bend excessively when a larger patient climbs aboard.

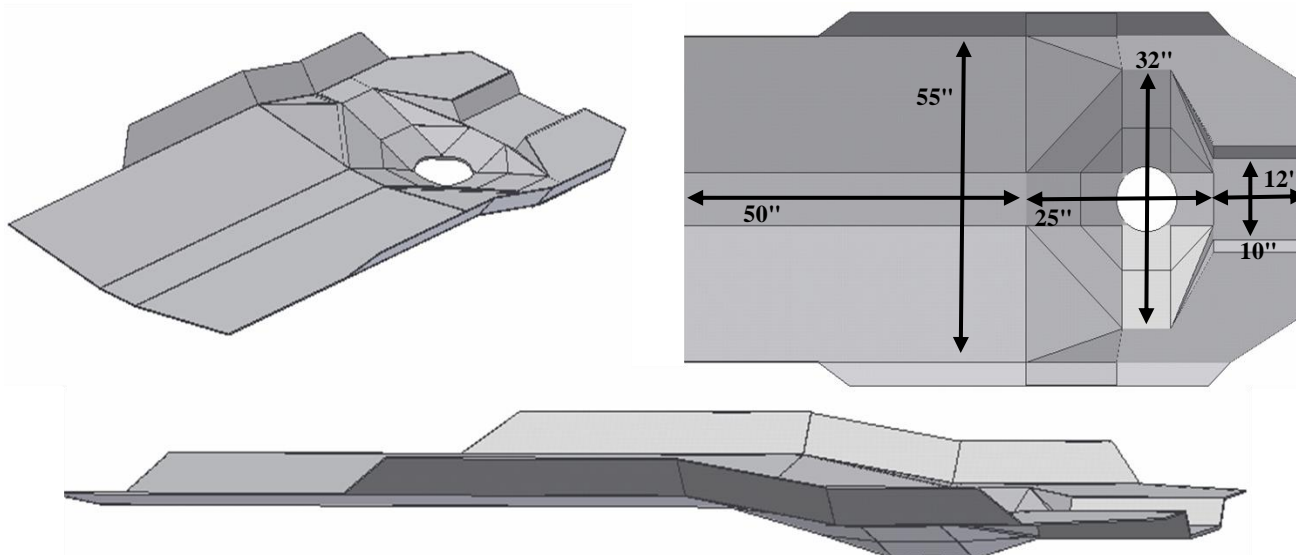


Figure 6. CAD model images of the designed bed from a (TOP LEFT) superior caudal oblique, (TOP RIGHT) superior, and (BOTTOM) lateral oblique perspectives. Notable is the angled octagon in the torso center, and the extended side panels. The bed is close to 55" wide, accommodating a wide variety of patient body types.

Figure 7 shows CAD models of the prototype bed with the CT and SPECT system FOVs superimposed. The proximity of the top plane of the x-ray beam to the chest wall of the patient is evident in the model. While the top plane of the beam intersects the bed, it is expected that the protruding chest of the patient will draw the breast more into the FOV and thus the chest wall will be partially intersected by the x-ray beam. The final 1/8" stainless steel bed has been manufactured and is illustrated above the integrated dual modality imaging system (Fig. 8).

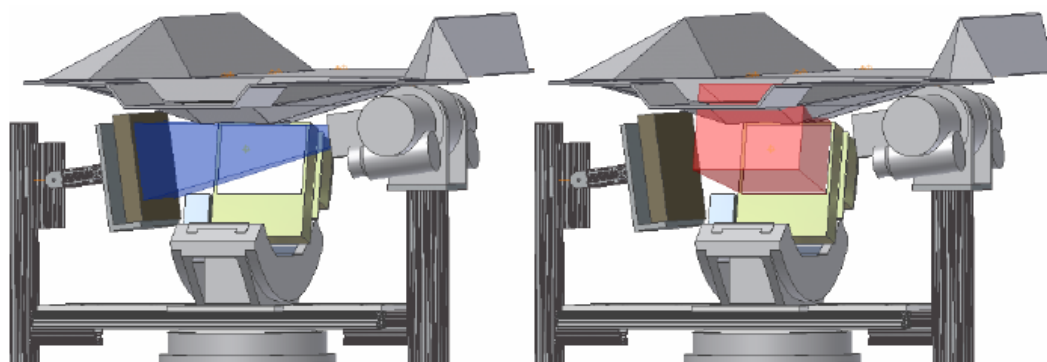


Figure 7. CAD model images of the bed with superimposed (LEFT) CT cone beam and (RIGHT) SPECT FOV. The cone beam intersects the chest wall. The SPECT FOV intersects the torso region of the patient but photons emanating from outside the breast volume of interest (except that volume directly above the hole) should be removed by additional 1/16" lead sheet lining the bed. The bed will be lined with a 1/16" lead sheet to form a graded absorber with the stainless steel bed. This combination will eliminate primary and scattered ^{99m}Tc photons outside of the breast volume of interest (namely, the rest of her body), and also eliminate scattered x-ray photons from breast to the torso of the patient.

Photographic images of the manufactured bed from different perspectives are shown (Fig. 8). A novel concept included in the manufactured bed is to design the inner octagonal section of the bed to be removable. This flexibility allows future iterations of the bed design to incorporate different materials with varying degrees of radioluminescence in the torso section

that may potentially allow the top plane of the x-ray cone beam to penetrate deeper into the chest wall. With the capability of the developed quasi-monochromatic beam used in this imaging system to drastically reduce dose delivered to the breast of the patient [15], penetrating the chest wall in this manner may be an acceptable option in future bed design iterations.

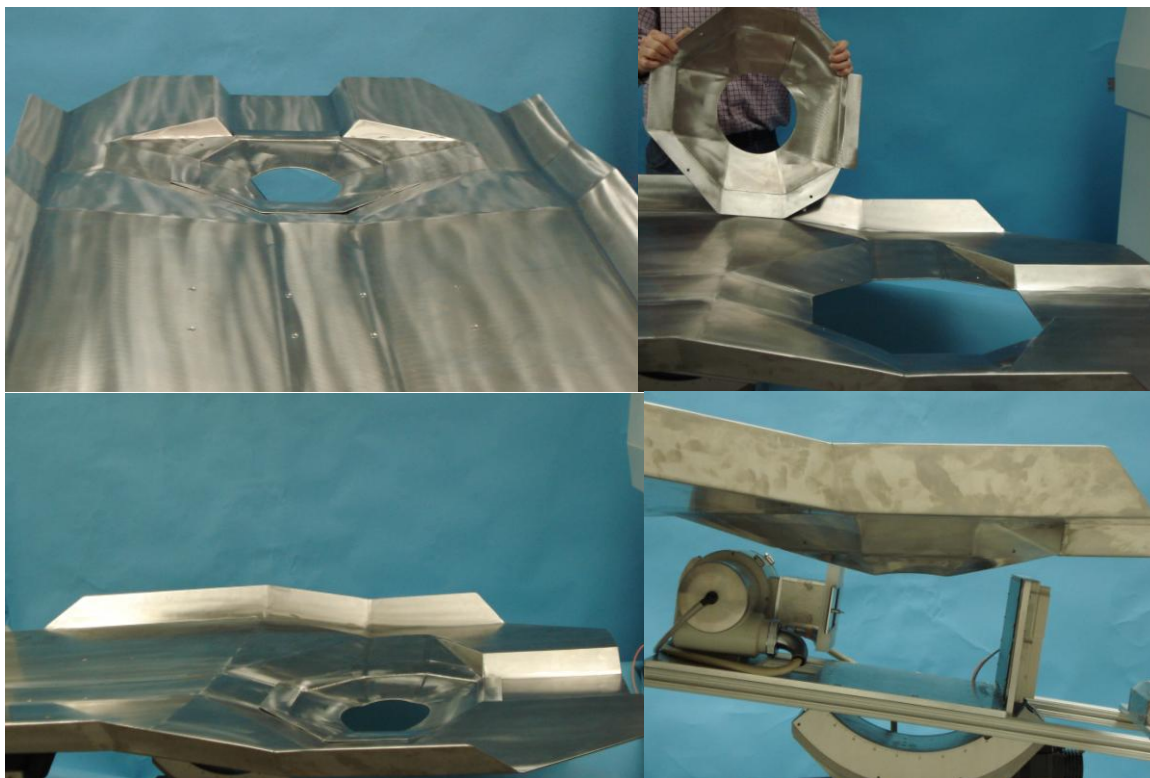


Figure 8. Photographs of the manufactured stainless steel bed from various perspectives. The multi-faceted nature of the bed is readily observed. Note also the (TOP, RIGHT) removable insert that can be replaced by a radiolucent material.

3.2 Limited Angle Tomography

The same sagittal plane slice of the spherical cross phantom in air, reconstructed using both a full and a limited number of acquisition angles is shown in Figure 9. The difference between the images is also presented. Profiles across each of the three indicated disc planes are shown superimposed for both data sets and difference profiles. Qualitatively, both the full and limited data set images have observable artifacts, more conspicuous as one moves from the image center to the upper edge. The streak artifacts are more readily observable in the limited data set than in the full data set, especially, the distortion in the uppermost level of spherical discs. Quantitatively, the profiles show differences of the order of 20% or more outside of the spherical regions indicating increased image distortion. Additional analysis of the data shows that this error is approximately 12% around the centroid of the spheres for the uppermost disc, reducing to close to zero when considering the spheres in the center of the detector. The artifacts are tell-tale signs of a lack of adequate sampling of the breast during data acquisition.

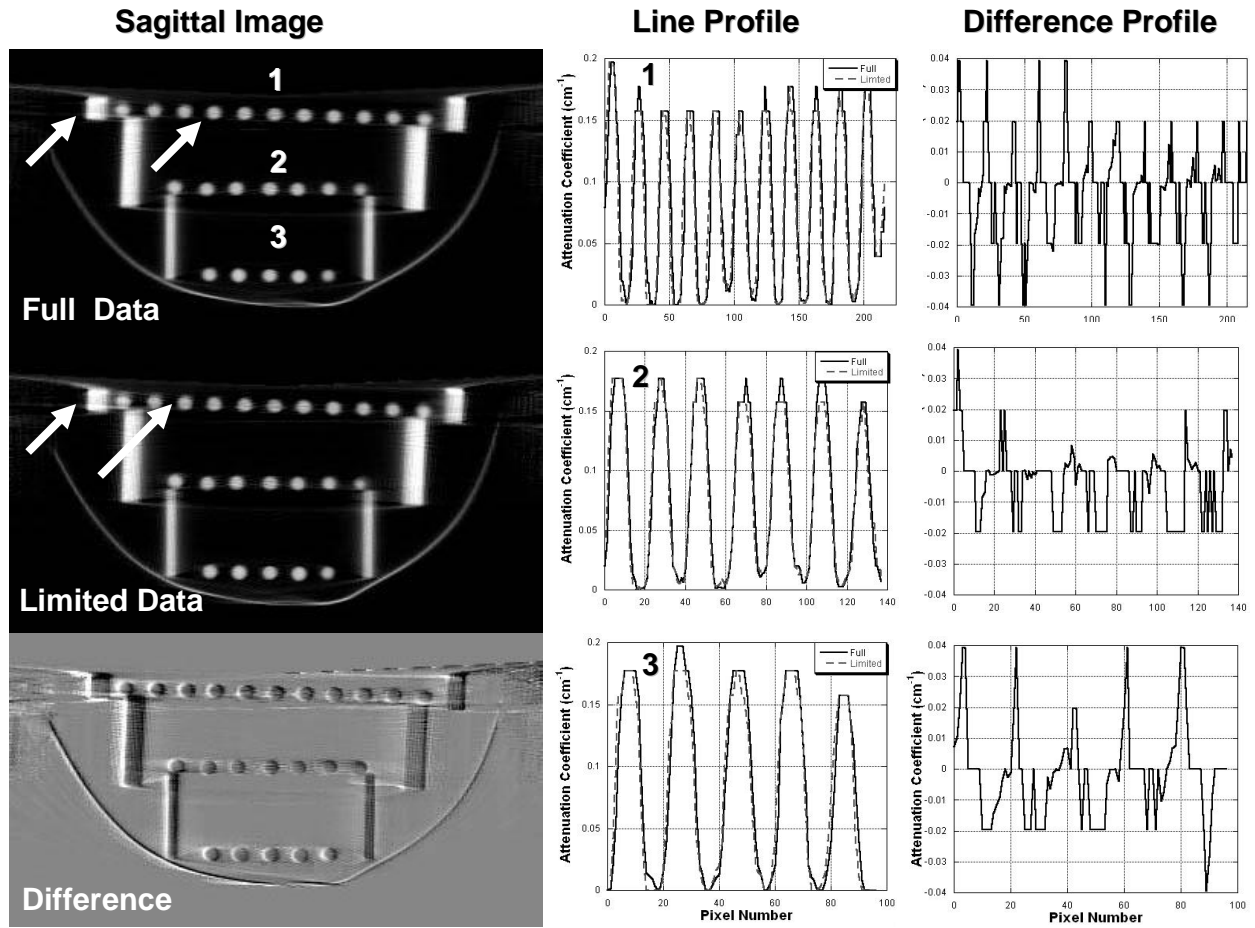


Figure 9. Reconstructed sagittal slice of the spherical disc phantom in air in a breast shaped cup from a (TOP LEFT) full 360 deg and (MIDDLE LEFT) limited azimuthal angle data set. (BOTTOM LEFT) is a difference image between the two. (CENTER COLUMN) Profiles across the imaged spheres from both data sets at each indicated disc plane. (RIGHT COLUMN) Profile of the difference in measured attenuation coefficients between a full and the limited data set across the same spheres. Streak and distortion artifacts are present in both images (at arrow tips) but are more apparent with the limited data set. The thick vertical lines are images of the acrylic cylindrical disc casings.

4. CONCLUSIONS

A custom-designed patient bed for prone imaging of a pendant, uncompressed breast has been developed. The bed is designed to concurrently consider patient comfort and satisfy the desire to image close to the chest wall. Primary design constraints included the physical dead-spaces due to the distance between the x-ray source focal spot and tube housing and the distance between the active edge of the x-ray detector plate and the edge of the detector housing.

The 1/8" stainless steel bed was manufactured and will be lined with 1/16" Pb sheet on the detector side and foam on the patient side. Preliminary studies with the imaging system components indicated that there was decreased emission contamination into the transmission images [16] and transmission contamination into the emission image [17], but this needs to be fully assessed with this fully assembled prototype bed.

Subsequent stages in the bed design will include a patient comfort study and further imaging studies using anthropomorphic phantoms and possibly patients to assess the efficacy of the design from both a comfort and imaging point of view. This is a preliminary design, the first step in what will likely be an iterative process as feedback from patient and imaging studies drive focused modifications to the design.

One major recognized design limitation of the current bed is the lack of ability to tilt the relatively large source and detector system. This inability compromises cone beam sampling of the pendant breast [5,7] and thus impacts the quality of reconstructed images. Reduced angular sampling caused by the limited angle of rotation available to the system also exacerbates the poorer image quality. Reconstructed images presented here exhibit obvious streak and distortion artifacts that are caused by a combination of insufficient polar and azimuthal sampling. It would seem that polar sampling plays a

larger role in the distortion as difference images of the same slice reconstructed with full and limited data sets tend to agree more closely over centroids of the acrylic spheres, and are in very close agreement when the sphere is located at the well-sampled center of the image. The full extent to which sampling limits the ability to detect lesions in breast or breast equivalent tissue for this patient bed setup was beyond the scope of this study, but is being investigated further [7]. In addition, future system designs may include x-ray imaging equipment with reduced geometric hindrance that will allow changes in bed design for the likely benefit of patient comfort. More importantly, the more compact equipment will permit the CT system to tilt and rotate to greater extents than currently possible. Greater source-detector positioning flexibility will help to more completely sample the breast pendant from a custom bed, and should lead to a reduction in image distortion.

ACKNOWLEDGEMENTS

This work is supported by NIH Grant R01-CA096821, DOD W81XWH-06-1-0791, and DOD W81XWH-05-1-0280.

Thanks to Barnes Metal Crafters (Wilson, NC) for their help and excellent skills in manufacturing the stainless steel bed.

REFERENCES

1. MP Tornai, JE Bowsher, CN Archer, J Peter, RJ Jaszczak, LR MacDonald, BE Patt, JS Iwanczyk. 2003. "A 3D Gantry Single Photon Emission Tomograph with Hemispherical Coverage for Dedicated Breast Imaging." *Nucl. Instr. Meth. Phys. Res. A*497(1):157-167.
2. C. N. Brzymialkiewicz, M. P. Tornai, R. L. McKinley, and J. E. Bowsher, "Evaluation of fully 3D emission mammotomography with a compact cadmium zinc telluride detector," *IEEE Trans. Med. Imag.*, vol. 24, pp. 868-877, 2005.
3. M. P. Tornai, R. L. McKinley, C. N. Brzymialkiewicz, P. Madhav, S. J. Cutler, D. J. Crotty, J. E. Bowsher, E. Samei, and C. E. Floyd, "Design and development of a fully-3D dedicated x-ray computed mammotomography system," *Proc. SPIE: Physics of Medical Imaging*, vol 5745 no. 1, pp. 189-197, 2005.
4. R. L. McKinley, M. P. Tornai, C. N. Brzymialkiewicz, P. Madhav, E. Samei, and J. E. Bowsher, "Analysis of a novel offset cone-beam transmission imaging system geometry for accommodating various breast sizes," Presented at the *2004 Workshop on the Nuclear Radiology of Breast Cancer*, Rome, Italy, 22 – 23 Oct. 2004, and published in *Medica Physica*, vol. XXI, pp. 46-53, 2006.
5. R. L. McKinley, C. N. Brzymialkiewicz, P. Madhav, and M. P. Tornai, "Investigation of cone-beam acquisitions implemented using a novel dedicated mammotomography system with unique arbitrary orbit capability," *Proc. SPIE: Physics of Medical Imaging*, vol. 5745, no. 1, pp. 609-617, 2005.
6. P. Madhav, D. J. Crotty, R. L. McKinley, M. P. Tornai, "Initial development of a dual-modality SPECT-CT system for dedicated mammotomography," presented at *IEEE Nuclear Science Symp. and Medical Imaging Conference*, San Diego, CA, 2006.
7. P. Madhav, DJ Crotty, RL McKinley, MP Tornai. "Evaluation of Lesion Distortion at Various CT System Tilts in the Development of a Hybrid System for Dedicated Mammotomography." Presented at *2007 SPIE Medical Imaging Meeting*, San Diego, CA, 17-22 Feb. 2007.
8. J. M. Boone, A. L. C. Kwan, J. A. Seibert, N. Shah, K. K. Lindfors, T.R. Nelson, "Technique factors and their relationship to radiation dose in pendant geometry breast CT," *Med. Phys.*, vol. 32(12), pp. 3767-3776, 2005.
9. J. M. Boone, A. Kwan, T. Nelson, N. Shah, G. Burkett, J. Seibert, K. Lindfors, G. Loos, "Performance assessment of a pendant-geometry CT scanner for breast cancer detection," *Proc. SPIE: Physics of Medical Imaging*, vol. 5745 no. 1, pp. 319-323, 2005.
10. S. Pani, R. Longo, D. Dreossi, F. Montanari, A. Olivo, F. Arfelli, A. Bergamaschi, P. Poropat, L. Rigon, F. Zanconati, L. Dalla Palma and Edoardo Castelli, "Breast tomography with synchrotron radiation: preliminary results," *Phys. Med. Biol.*, vol.49, pp. 1739-1754, 2004.
11. R. Ribeiro, C. Abreu, P. Almeida, F. Balau, P. Bordalo, N.C. Ferreira, S. Fetal, F. Fraga, P. Lecoq, M. Martins, N. Matela, R. Moura, C. Ortigao, L. Peralta, S. Ramos, P. Rato, P. Rodrigues, A.I. Santos, A. Trindade and J. Varel, "Breast imaging with a dedicated PEM," *Nucl. Instr. Meth. Phys. Res A*, vol. 527, pp 87-91, 2004.
12. R. Freifelder, J. Karp. Dedicated PET scanners for breast imaging. *Phys. Med. Biol.* vol. 42, pp. 2463-2480, 1997.

13. R. L. McKinley, M. P. Tornai, E. Samei, and M. L. Bradshaw, "Initial study of quasi-monochromatic beam performance for x-ray computed mammotomography," *IEEE Trans. Nucl. Sci.*, vol. 52, pp. 1243-1250, 2005.
14. D.J. Crotty, R. L. McKinley, M. P. Tornai, "Experimental spectral measurements of heavy k-edge filtered beams for x-ray computed mammotomography," *Phys. Med. Biol.* 52(3):603-616, 2007.
15. R. L. McKinley and M. P. Tornai, "Preliminary investigation of dose for a dedicated mammotomography system," *Proc. SPIE: Physics of Medical Imaging*, vol 6142, pp. 60-70, 2006.
16. D. J. Crotty, C. N. Brzymialkiewicz, R. L. McKinley, and M. P. Tornai. "Investigation of emission contamination in the transmission image of a dual modality computed mammotomography system," *Proc. SPIE: Physics of Medical Imaging*, vol 6142, pp. 1088-1098, 2006.
17. D. J. Crotty, C. N. Brzymialkiewicz, R. L. McKinley, and M. P. Tornai, "Optimizing orientation of SPECT and CT detectors through quantification of cross contamination in a dual modality mammotomography system," *IEEE Conference Record NSS/MIC*, pp. 1672-1676, 2005.

Appendix F

Coauthor

SPIE 2007 Medical Imaging Conference – presented by Priti Madhav - San Diego, February, 2007.

Evaluation of Lesion Distortion at Various CT System Tilts in the Development of a Hybrid System for Dedicated Mammotomography

Priti Madhav^{1,2}, Dominic J. Crotty^{1,2}, Randolph L. McKinley^{1,2}, Martin P. Tornai^{1,2}

¹ Department of Radiology, Duke University Medical Center, Durham, NC

² Department of Biomedical Engineering, Duke University, Durham, NC

ABSTRACT

A hybrid SPECT-CT system for dedicated 3D breast imaging (mammotomography) is currently under development. Each imaging system will be placed on top of a single rotation stage and moved in unison azimuthally, with the SPECT system additionally capable of polar and radial motions. In this initial prototype, the CT system will initially be positioned at a fixed polar tilt. Using a phantom with three tungsten wires, the MTF of the CT system was measured in 3D for different CT system tilts. A phantom with uniformly arranged 0.5cm diameter acrylic spheres was suspended in air in the CT field of view, and also placed at multiple locations and orientations inside an oil-filled breast phantom to evaluate the effect of CT system tilt on lesion visibility and distortion. Projection images were collected using various simple circular orbits with fixed polar tilts ranging between $\pm 15^\circ$, and complex 3D saddle trajectories including combined polar and azimuthal motions at maximum polar tilt angles. Reconstructions were performed using an iterative reconstruction algorithm on 4x4 binned projection images with 0.508mm³ voxels. There was minor variation in the MTF in the imaged volume for the CT system at all trajectories, potentially due to the use of an iterative reconstruction algorithm. Results from the spherical cross phantoms indicated that there was more reconstruction inaccuracy and geometric distortion in the reconstructed slices with simple circular orbits with fixed tilt in contrast to complex 3D trajectories. Line profiles further showed a cupping artifact in planes farther away from the flat plane of the x-ray cone beam placed at different tilts. However, this cupping artifact was not seen for images acquired with complex 3D trajectories. This indicated that cupping artifacts can also be caused by undersampled cone beam data. These findings generally indicate that despite insufficient sampling with the cone beam imaging geometry, it is possible to place the CT system at a stationary polar tilt with the CT tube positioned upward such that a patient can be comfortably placed above the system and allow complete sampling near the top of the pendant, uncompressed breast and chest wall. However, a complex 3D trajectory allows for more complete sampling of the entire image volume.

Keywords: computed tomography, tomography, mammotomography, breast imaging, transmission imaging, cone beam, dual –modality, orbits, iterative reconstruction, modulation transfer function (MTF)

1. INTRODUCTION

Over the past decade, dual-modality tomographic imaging systems have grown in popularity and offer great promise in the detection and staging of numerous cancerous diseases, monitoring and prediction of treatment therapies, and improving precision of surgical biopsies. The main benefit of simultaneously acquiring 3D transmission and emission data is in the ability to fuse the structural anatomical framework of an object obtained from a transmission image onto an emission image that illustrates the localization of the radioactive metabolic uptake (i.e. function) of a tumor. Additionally, the transmission data can be used to estimate an attenuation map of the object and can be applied to the emission data to compensate for photon attenuation and absorption by overlapping structures. It is expected that integrating complementary anatomical and functional information can lead to further improvement in visual quality and quantitative accuracy of radionuclide imaging over independent systems¹⁻⁵.

Our lab has been working on developing such a dual-modality single photon emission computed tomography (SPECT) and computed mammotomography (CmT) imaging system specifically dedicated to fully-3D breast imaging⁶⁻⁸. With the compact, high performance gamma camera of the SPECT system⁹ and novel quasi-monochromatic x-ray cone beam of the CmT system^{10, 11}, both systems have independently yielded visualization of small lesions in the breast, especially ones closer to the chest wall. The 3D motion positioning of each system allows the detector to be positioned anywhere about a pendant, uncompressed breast^{10, 12-14}. 3D acquisition trajectories have been implemented to contour the breast and image further into the breast by utilizing the system's azimuthal and polar tilting capabilities.

In its initial integration, the SPECT system retains its fully 3D positioning. However, the CmT system is at a fixed tilt angle and restricted to the 360° azimuthal direction around the vertical axis of a pendant breast. This limits the CmT system in imaging deep into the breast and axillary region, and introduces insufficient sampling which was previously shown by us to be overcome by using 3D complex acquisition trajectories¹². In this study, we describe the configuration of the dual-modality SPECT-CmT system and quantify the effects of spatial resolution and lesion distortion of the CmT system at different stationary tilts and 3D complex acquisition trajectories. It is necessary to find a stationary tilt that will provide sufficient information and allow maximal access to the patient's breast, and accommodate a custom patient bed that can fit above this compact hybrid system and shield the patient from scattered, low energy x-rays and photons, and maintain patient comfort¹⁵.

2. MATERIALS AND METHODS

Overview of the SPECT-CmT System

The first prototype compact dual-modality SPECT-CmT system was built (Fig. 1) to image a pendant uncompressed breast⁶. Both systems, using separate detectors to view an object in the common field-of-view (FOV), rest on top of a common rotation stage (model RV350CCHL, *Newport Corp.*, Irvine, CA) to allow an azimuthal rotation of 360° around the vertical axis of the breast. The SPECT system is placed at a fixed position such that it is 90° relative to the x-ray source-detector axis, and the center of rotation (COR) matches the COR of the CmT system. With both systems on the same gantry, the patient will not be required to move between the SPECT and CmT acquisitions. A customized patient bed, which will be placed above the hybrid system, is currently being designed such that it will maintain patient comfort and allow the imaging systems to contour the patient's breast¹⁵.

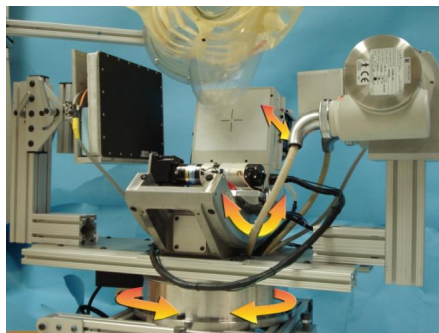


Figure 1: Photograph of the prototype dual-modality dedicated breast imaging tomographic system. The SPECT system (center) is placed orthogonally to the CmT tube (right) and digital flat-panel detector (left). The arrows illustrate system motions (azimuthal, polar, and radius of rotation). Note that the pendant breast is in a common FOV of each system.

Figure 2 shows a few images of the current dual-modality SPECT-CmT system rotating around a pendant uncompressed breast. As shown in the corresponding polar plot, the SPECT system has its fully 3D positioning capabilities while the CmT system remains at a fixed polar tilt as the system rotates 360° around the breast.

Along with the parallel beam imaging geometry of the SPECT system, the entire volume of the breast is in the FOV of both systems even at different cone beam CmT tilts. This is shown in the 3D CAD drawings of the SPECT-CmT system in Fig. 3. Additionally, in order to completely sample the entire volume of interest, the central ray of the CmT cone beam is laterally offset 5cm relative to the center of rotation¹¹.

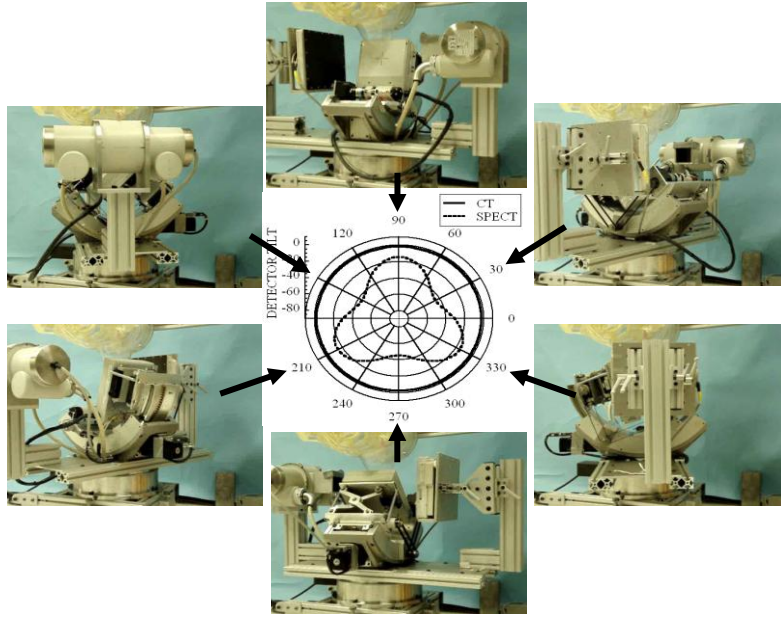


Figure 2: Photographs at different positions of the dual-modality system rotating around a pendant, uncompressed phantom breast and torso. Polar plot (center) is shown for the SPECT (3D PROJSINE orbit is dotted) and CmT systems (vertical axis of rotation [VAOR] orbit is solid circle).

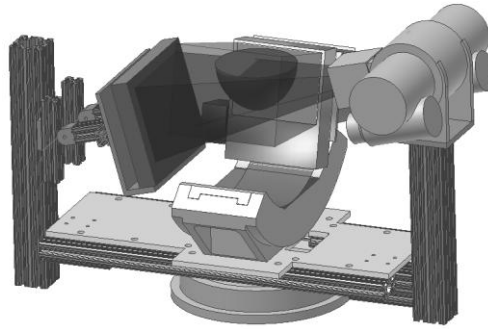


Figure 3: 3D CAD model of the SPECT-CmT system with a breast placed at the center of rotation of the system. The breast is in the FOV of both systems regardless of the tilt of the CmT system (-15 degrees shown in this diagram). This is shown with the intersection of both the parallel beam of the SPECT system and the cone beam of the CmT system.

SPECT System

Our current emission tomography system uses a compact $16 \times 20 \text{ cm}^2$ field of view Cadmium Zinc Telluride (CZT) gamma camera (model *LumaGEM 3200S*TM, *Gamma Medica, Inc.*, Northridge, CA) with discretized crystals, each $2.3 \times 2.3 \times 5 \text{ mm}^3$ on a 2.5mm pitch. Measured energy resolution of the gamma camera at 140keV is 6.7% FWHM and collimator sensitivity is 37.9cps/MBq¹³. Higher energy resolution is the primary reason of using the CZT camera over scintillators such as the NaI(Tl)-based cameras for the SPECT system. This system has a parallel-hole collimator with hexagonal holes (1.2mm hole size flat-to-flat, 0.2mm septa, and 25.4mm height). The camera is attached to a laboratory jack and a goniometric cradle (model BGM200PE, *Newport Corp.*, Irvine, CA) permitting various radius of rotations (RORs) and polar tilts (ϕ), respectively.

CmT System

Our existing cone beam transmission tomography system uses a rotating tungsten target x-ray source (model *Rad-94*, *Varian Medical Systems*, Salt Lake City, UT) with a 0.4/0.8mm focal size and 14° anode angle and a $20 \times 25 \text{ cm}^2$ FOV CsI(Tl)-based amorphous silicon digital x-ray detector (model *Paxscan 2520*, *Varian Medical Systems*, Salt Lake City, UT) with a grid size of 1920×1536 pixels and $127 \mu\text{m}$ pitch. Source and detector are secured to the same metal plate as the SPECT system. A custom built collimator is attached to the x-ray source to hold ultra-thick K-edge beam shaping filters to produce a quasi-monochromatic beam¹⁶. For these studies, a Ce 100^{th} attenuating value layer filter ($Z=58$, $\rho=6.77 \text{ g/cm}^3$, K-edge=40.4keV, *Santoku America, Inc.*, Tolleson, AZ) was used to yield a mean energy of $\sim 36 \text{ keV}$ and

FWHM of 15%. In the hybrid setup, the source-to-image distance (SID) was 60cm and source-to-object distance (SOD) was 38cm. The central ray of the CmT cone beam is laterally offset 5cm relative to the center of rotation to completely sample the entire volume of interest¹¹. Unlike the SPECT system, the CmT system is at a fixed tilt angle and restricted to only azimuthal motion.

Phantoms

The MTF in 3D was calculated using an MTF thin-wire phantom as previously described¹⁷ (Fig. 4, LEFT). Three tungsten wires of 508 μ m diameter and ~11cm length were positioned nearly orthogonal to each other within the cube such that they were visibly separable in their positions and did not touch each other near the center.

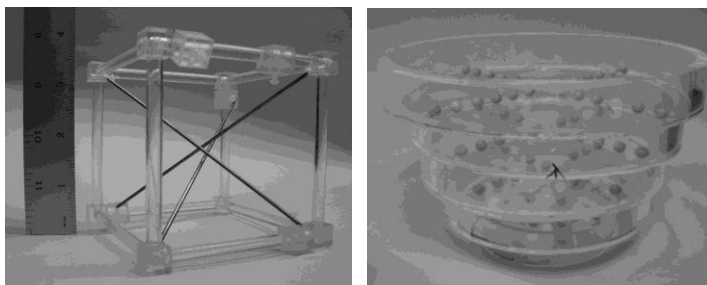


Figure 4: (LEFT) Photograph of the MTF phantom used to measure the MTF in 3D. (RIGHT) Photograph of the phantom with small spheres suspended on thin plastic sheets inside each circular band; each sphere is a 0.5cm diameter acrylic ball arranged in a cross pattern to measure lesion visualization at different planes in an image volume.

To measure the lesion visualization and distortion at different planes of the image volume, a phantom consisting of multiple circular acrylic bands of varying diameters and 2cm height were constructed (Fig. 4, RIGHT). Plastic wrap (“Saran”) with 0.5cm diameter acrylic balls arranged on a 1cm center-to-center pitch in a cross pattern using a jig was stretched and glued to the bottom of each circular frame. The completed frames could then be easily stacked and also immersed in liquids while retaining the distribution of spheres on a single plane.

Data Acquisition

For the MTF and lesion distortion evaluation experiments, the independent CmT system was used in its original goniometric configuration¹⁰⁻¹². In this setup, the source-to-image distance (SID) was 55cm and the source-to-object distance (SOD) was 35cm. Tube potential was set at 60kVp with a 1.25mAs exposure. MTF was measured by suspending the MTF phantom in air at the COR of the CmT system. Tilt effects were also evaluated by stacking the multiple spherical cross phantoms in a 1050mL breast phantom shell (nipple-to-chest distance of 11cm, medial-to-lateral distance of 17cm, and superior-inferior distance of 18cm). These measurements were taken in air and with the breast uniformly filled with mineral oil to provide different contrasts between the acrylic spheres and breast background. Mineral oil has an intrinsic density of 0.87 g/cm³ and acrylic has a density of 1.19 g/cm³.

Initial measurements were obtained using a simple circular trajectory at 0, ± 5 , ± 10 and ± 15 degree fixed polar tilts (Fig. 5, LEFT), and a saddle trajectory having +15 to -15 degree polar tilt (Fig. 5, RIGHT). Note that a negative polar tilt is defined as the x-ray source moving up (closer to the patient bed) and the detector moving down (closer to the ground). Projection images were collected every 1.5° through a 360° azimuthal acquisition for a total of 240 projections. Although the breast is truncated (as shown in the 3D CAD drawings), the spherical cross phantoms were placed in the breast such that they were in the center of the field-of-view and not truncated.

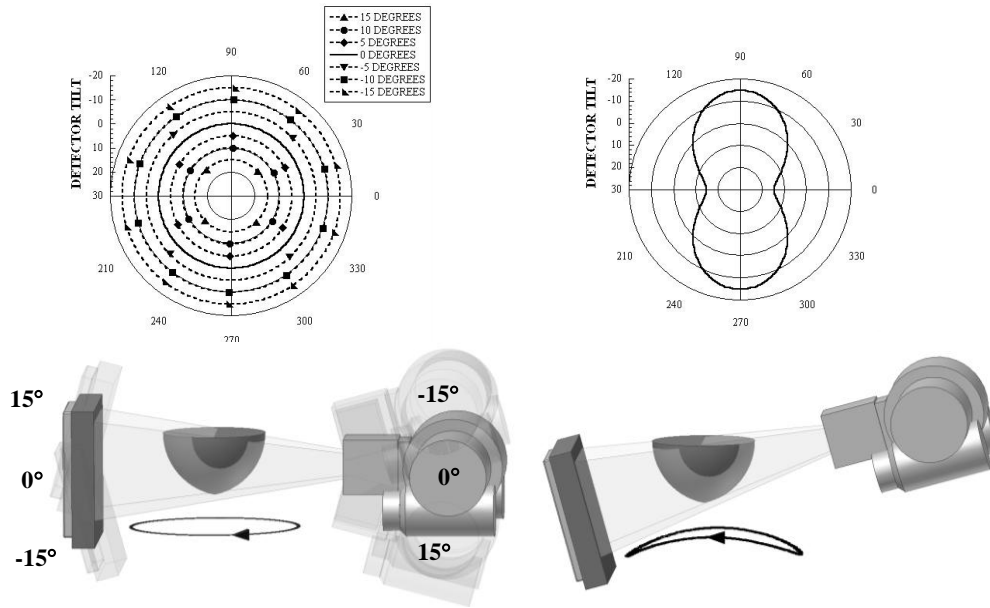


Figure 5: (TOP) Polar plots for (LEFT) simple circular trajectories at 0, ± 5 , ± 10 , and ± 15 degree fixed polar tilts and (RIGHT) 3D saddle trajectories. Polar tilt of the CmT system is defined by the radius of the circle, and azimuth angle is defined around the circumference of the circle. (BOTTOM) The 3D CAD drawings of the setup of the CmT system are shown to illustrate the location(s) of the system during the acquisition. Negative polar tilt is defined as the x-ray detector moving down (or x-ray source moving closer to the patient bed). The breast phantom is placed in the cone beam CmT's FOV, and is seen to be laterally truncated somewhat in the drawings. Dark circles underneath CAD drawings indicate polar displacement with changing azimuth.

Image Reconstruction

Image reconstruction was performed on the CmT projection images using a statistically based iterative, ray-driven ordered-subsets transmission algorithm (OSTR)^{10, 11, 16}. Projection images were corrected for gain and offset and binned to 4x4 pixels. Reconstruction parameters for the MTF acquisition were set to 10 iterations, 8 subsets, 350x350x384 reconstruction grid, and 508 μm^3 voxel size. Reconstruction parameters for the lesion distortion measurements were set to 5 iterations, 16 subsets, 350x350x384 reconstruction grid, and 508 μm^3 voxel size.

Data Analysis

Using an algorithm described previously¹⁷, reconstructed images of the MTF phantom were used to calculate the MTF at different locations along each of the three wires. The MTFs were compared among the different acquisition orbits.

Lesion visualization and distortion were observed using the reconstructed images of the circular discs phantom collected for all acquisition orbits. For each circular disc, line profiles were drawn over the lesions in the horizontal and vertical directions. For each circular disc placed in oil, the line profiles obtained through the spheres were fit to a Gaussian curve and fit parameters extracted. Although the full-width at half maximum (FWHM) only partially characterizes the spatial resolution, it can be useful in making comparisons among different acquisition techniques such as CmT system tilts. Another useful parameter was the sphere's centroid which could be compared to the known 1cm pitch on the original phantoms.

3. RESULTS AND DISCUSSION

MTF in 3D

As shown in Figure 6 and Table I, there was no significant difference between the MTFs. As shown previously¹⁷, the MTF does show improvement when the sampling rate is increased by binning the original projection images to 2x2 rather than 4x4. However, with the limitations in computer processor speed and memory, the current iterative reconstruction code can only handle 4x4 binned uncropped image sets and reconstruct to a limited grid size.

Since MTF measurements were taken using wires made of a highly attenuating material placed in air, there is a large difference in attenuation coefficients between the wire and background in the projection images. At each iteration, the nonlinear reconstruction algorithm maximizes this difference between pixel values and therefore a similar answer is obtained for all acquisition trajectories in just a few iterations. Thus, a similar study needs to be done to investigate the MTF when the phantom is instead placed in a scatter media (e.g. oil, water) such that there is not a large difference in attenuation values with tungsten and to add background noise.

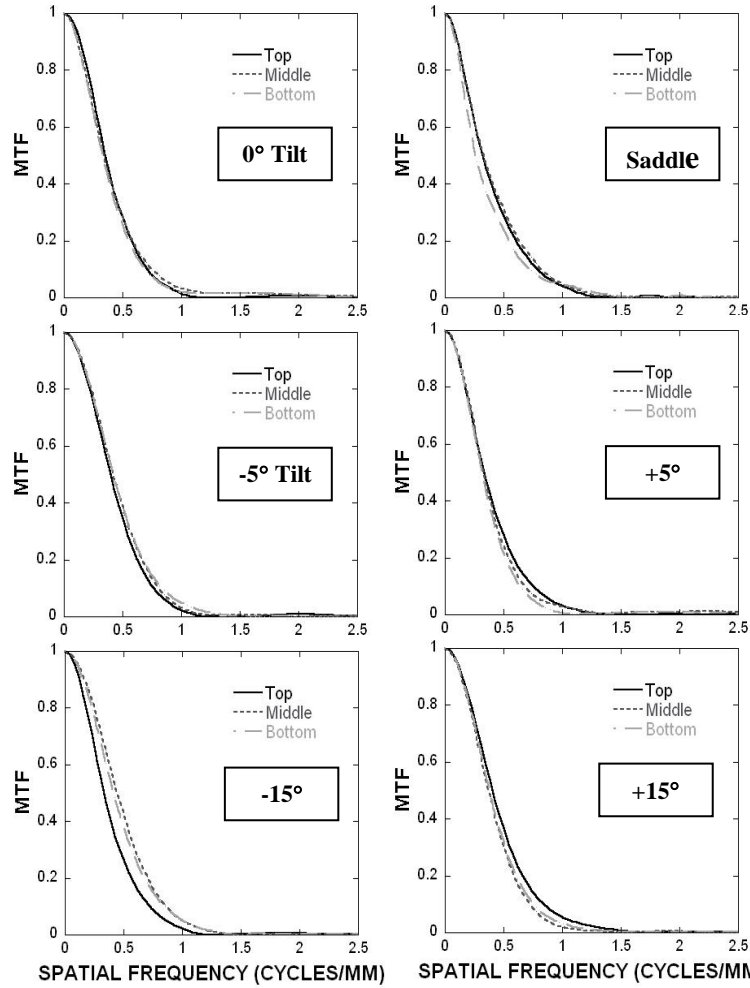


Figure 6: Measured MTF of the top, middle, and bottom part for Wire C for (TOP LEFT) 0, (MIDDLE) ± 5 , and (BOTTOM) ± 15 degrees and (TOP RIGHT) saddle trajectory

Table 1: RMSD values along the top, middle, and bottom segment of each of the three tungsten wires for various acquisition trajectories

	Wire A		Wire B		Wire C	
Orbits	Top-Middle	Middle-Bottom	Top-Middle	Middle-Bottom	Top-Middle	Middle-Bottom
-15	0.020	0.011	0.019	0.018	0.045	0.015
-5	0.007	0.023	0.021	0.016	0.015	0.006
0	0.011	0.012	0.014	0.026	0.015	0.012
5	0.014	0.025	0.018	0.013	0.014	0.014
15	0.014	0.011	0.017	0.023	0.010	0.008
Saddle	0.021	0.010	0.022	0.011	0.009	0.026

Lesion Visualization/Distortion

Lesion distortion was first measured in different coronal slices of the breast phantom by obtaining line profiles over the acrylic balls in each circular phantom disc. Profiles were drawn through the lesions in each of the three smallest circular discs placed closest to the nipple (Fig. 7). From these profiles, it is seen that there is not much difference between the profiles for the spherical cross phantoms regardless of which acquisition trajectory (fixed tilt or saddle) was used.

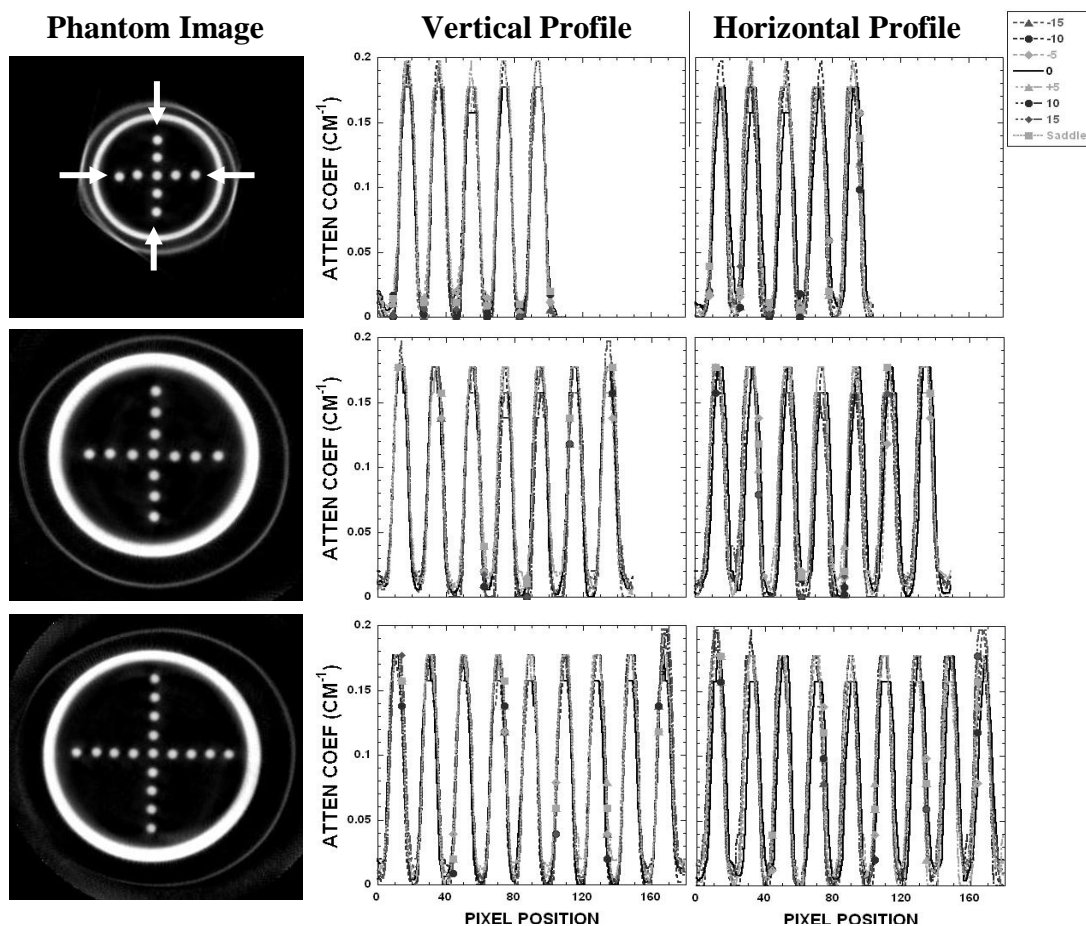


Figure 7: (LEFT) Reconstructed slices of the sphere phantoms acquired with saddle. (MIDDLE) Vertical and (RIGHT) horizontal profiles drawn through lesions at the level indicated by the white arrows in the top image plane.

By examining the reconstructed coronal slices at each of the circular discs, overlapping structures are apparent for reconstructed slices obtained using stationary polar tilt orbits (Fig. 8 and Fig. 9). Due to the failure to meet Tuy's data sufficiency condition in the polar direction for fixed tilt orbits¹⁸, reconstruction of slices for locations far away from the flat plane of the cone beam contains errors due to insufficient sampling. This can be best explained in the 3D drawings. As shown in Fig. 8, when the CT detector is down (closer to the ground) at a -10° tilt, the cone beam is relatively flat at the top. At this slice, there is nearly complete sampling where we can see all the lesions and no overlapping structures (Fig. 10). However, as we look at reconstructed slices closer to the nipple, overlapping structures become more noticeable. At this tilt, each ray of the cone beam intersects the phantom in a similar way regardless of the azimuthal source-detector location. Due to the insufficient polar sampling to "fill in" additional views of the object in the FOV, out of plane information is inaccurately superimposed on any single plane of interest. The same is true in the $+10^\circ$ tilt case, whereas the reconstruction inaccuracy occurs for slices that are reconstructed from divergent cone beam rays away from the flat plane at the bottom of the cone beam (Fig. 9). Reconstruction inaccuracy would generally increase with larger cone beam angles. In addition to reconstruction inaccuracy, geometric distortion also results with circular orbits¹². However, using the saddle trajectory, there is more complete polar sampling yielding far fewer noticeable artifacts in the reconstructed slices (Fig. 8 and Fig. 9, 3RD TO LEFT). This is confirmed by the line profiles through the images (Fig. 8 and Fig. 9, RIGHT). With 3D acquisition trajectories such as saddle, there is no single ray that looks at the phantom from exactly the same vantage, resulting in more complete sampling and removal of overlapping structures. Although more lesions can be clearly seen when the cone beam is flat near the top of the breast (i.e. -10° tilt), complex 3D trajectories allow for less distortion and more complete sampling (Fig. 10).

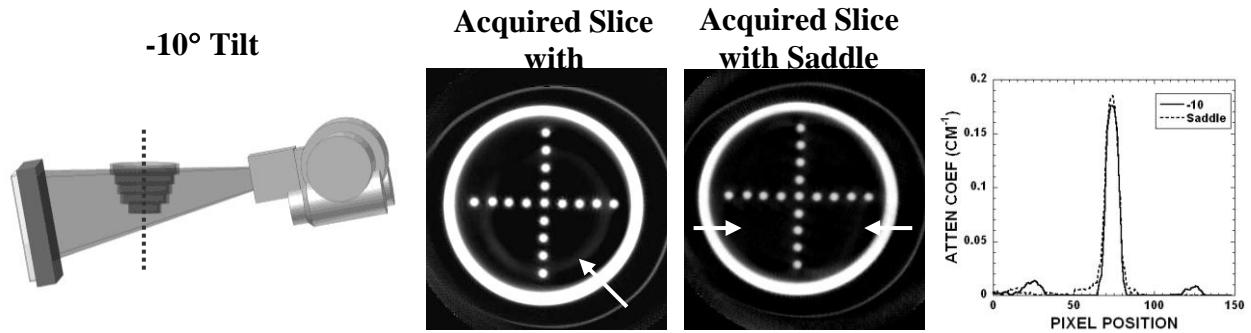


Figure 8: (LEFT) 3D CAD drawing of the setup of the -10° tilted orbit with a black dashed line indicating the vertical axis of rotation. (2ND TO LEFT) Reconstructed slice of the third smallest spherical cross phantom obtained with -10° tilted orbit. Arrow illustrates of an overlapped region (shown in arrow) due to sampling insufficiency acquired with a fixed polar tilt. (3RD TO LEFT) Reconstructed slice of the same phantom acquired with the saddle trajectory. No overlapped region is seen. (RIGHT) Line profile (shown in arrow on the Saddle slice) shows that there is some artifact in the slice acquired with the -10° tilt.

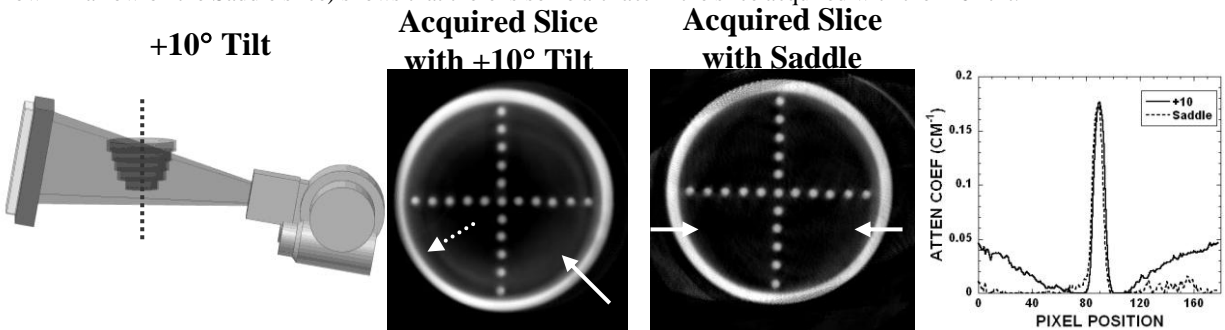


Figure 9: (LEFT) 3D CAD drawing of the setup of the $+10^\circ$ tilted orbit with a black dashed line indicating the vertical axis of rotation. (2ND TO LEFT) Reconstructed slice of the second largest spherical cross phantom obtained with -10° tilted orbit. Solid arrow illustrates an overlapped region due to sampling insufficiency acquired with a fixed polar tilt. Dotted arrow illustrates the geometric distortion of the acrylic frame. (3RD TO LEFT) Reconstructed slice of the same phantom acquired with the saddle trajectory. No overlapped region or geometric distortion is seen. (RIGHT) Line profile (shown in arrow on the Saddle slice) shows that there is some artifact in the slice acquired with $+10^\circ$ tilt.

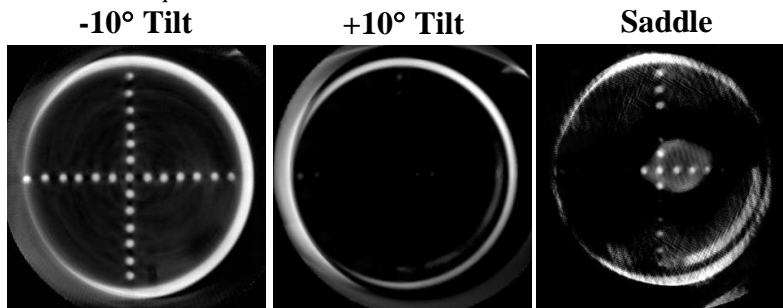


Figure 10: Reconstructed slice of the top spherical cross phantom acquired at (LEFT) -10° , (MIDDLE) $+10^\circ$ tilt, and (RIGHT) Saddle trajectory. As shown in the 3D CAD drawing, the top plane at the -10° tilt is more uniformly sampled. Even though more lesions are seen at the -10° tilt, 3D complex trajectories have less distortion and more complete sampling in the rest of the reconstruction volume.

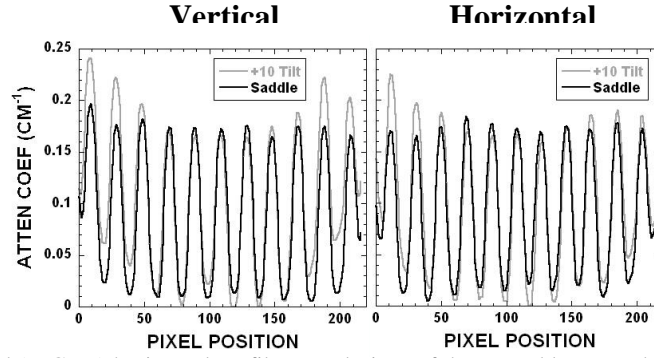


Figure 11: (LEFT) Vertical and (RIGHT) horizontal profiles over lesions of the second largest spherical cross phantom obtained with $+10^\circ$ tilt and saddle shown in Fig. 9. There is a cupping artifact seen with the fixed tilt orbit by observing the intensities from the edge towards the center, which could be mistaken as due to scatter. This is missing from the saddle acquired data due to its more sufficient sampling throughout the imaged volume.

Profiles drawn over the lesions of the second largest spherical cross phantom shown in Fig. 9 are shown in Fig. 11. Vertical and horizontal profiles show that the insufficient sampling from a fixed tilt orbit results in a cupping-type artifact, which could be mistaken for scatter or beam hardening. Since the spheres are virtually suspended in air on a thin plastic sheet, scatter is minimal in this experimental setup. Thus, any scatter correction applied to this region may “flatten” the response across the image, but would incorrectly account for the measured scatter response, which is really due to an artifact from insufficient sampling with a fixed cone beam source tilt.

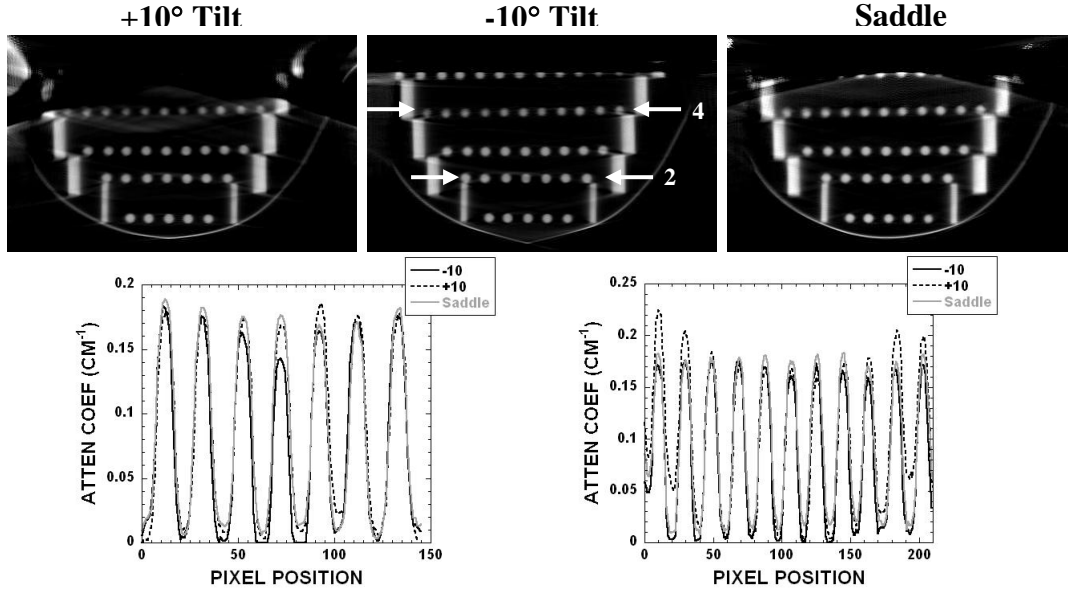


Figure 12: (TOP) Sagittal reconstructed slices of the spherical cross phantoms acquired with indicated trajectories. (BOTTOM) Profiles drawn through spherical cross phantom (BOTTOM LEFT) at level 2 (indicated in TOP MIDDLE image) and (BOTTOM RIGHT) at level 4. -10° tilt shows greater peak uniformity at the 4th level sphere phantom, while $+10^\circ$ tilt shows more uniformity at the 2nd level of the phantom. Saddle trajectory shows peak height uniformity along both cross phantoms.

Effects of sampling insufficiency were also seen in the reoriented sagittal slices of the data (Fig. 12). When the system is at a -10° tilt, there is better sampling at the top of the reconstructed volume rather than the bottom as seen by the uniformity of the peak heights of the profiles across the FOV. This is reversed for the $+10^\circ$ tilt, which again shows a similar cupping artifact as illustrated earlier in Fig. 11, which plane was located at an extreme of the cone beam. However, while the particular image shows artifacts at the top with a saddle trajectory, there is uniformity along the entire reconstructed volume for the indicated spheres.

In order to assess whether these phenomenon are visible in more solid objects, the breast containing the spheres was uniformly filled with mineral oil. Due to the physical distortion of the breast phantom when filling it with oil (i.e. the added weight), only the four smallest circular phantoms fit in the breast shell. Fig. 13 shows the reconstructed slices of the 3rd smallest circular phantom in the breast filled with oil measured with different trajectories. Horizontal profiles were drawn over the lesions (Fig. 14). Just as in the experiments in air, the negative tilt orbits showed more uniform sampling since this layer of the phantom was located closer to the flat part of the cone beam.

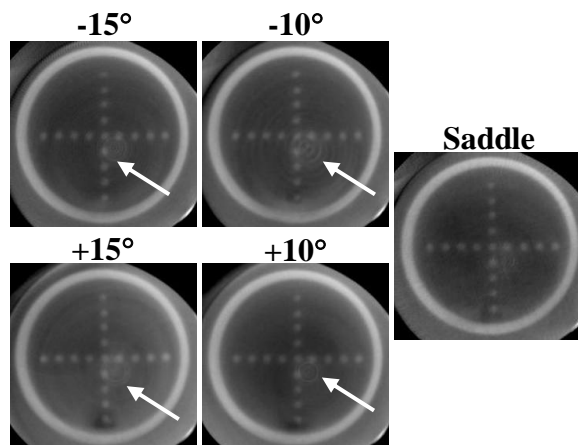


Figure 13: Reconstructed slices of spherical cross phantom in oil acquired at various acquisition trajectories as indicated. Images acquired with a stationary polar tilted, circular orbit had a circular ring (indicated by arrow) in some of the reconstructed slices. However, in the same slice for the saddle trajectory, there is no circular ring apparent.

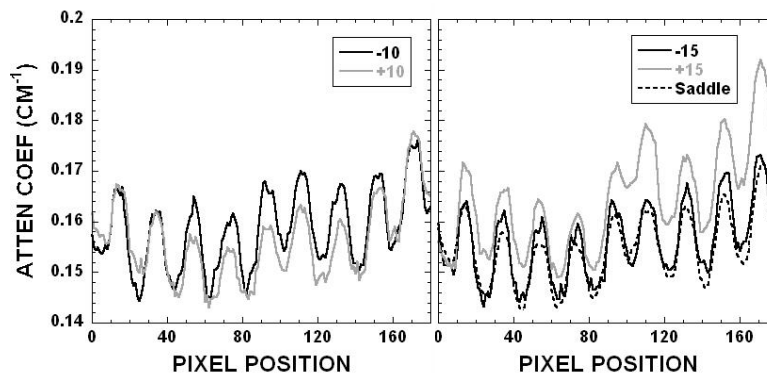


Figure 14: Horizontal profiles of (LEFT) $\pm 10^\circ$ and (RIGHT) $\pm 15^\circ$ tilts and saddle at the 3rd ring level from the nipple. Negative tilts and 3D complex trajectories show more uniform sampling.

When closely observing the reconstructed images for all trajectories, a circular ring appears in the reconstructed slices, except for the saddle trajectory (Fig. 13). Typically, such a circular ring in reconstructed images is caused by a bad pixel or series of them in the detector. We believe this is the case here for the fixed tilt orbits. However, the advantage of using a 3D complex trajectory such as saddle is that the same bad pixel does not always view the object from the same vantage, in contrast to simple circular orbits. Because of this, reconstructed images acquired with the saddle trajectory tend to not have these artifacts.

FWHM values were calculated for the outer lesions in the top sphere phantom (level 4). Some of these values are shown below (Fig. 15). Similar to the case shown in air, it is seen that the -10° has a smaller FWHM values (less spread) than rest of the orbit. At this slice, this specific orbit has more complete sampling since the rays are more towards the flat part of the cone beam as shown in the 3D CAD drawing in Fig. 8.

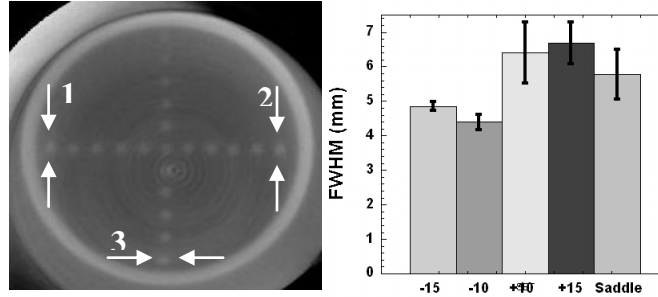


Figure 15: (LEFT) Reconstructed slices of the top spherical cross phantom in oil acquired at -10° acquisition tilt. FWHM values were determined over the lesions specified by the numbered arrows. (RIGHT) Mean FWHM values (in mm) over the lesions in the top circular phantom in oil. Standard deviation is shown in solid vertical bars.

4. CONCLUSIONS

Imaging with a dedicated dual-modality breast imaging tomographic system may help to improve identification and localization of lesions that is crucial for patient screening, diagnostics and therapeutic monitoring. In this work, we have demonstrated a prototype SPECT-CmT system that can provide volumetric fully-3D registered and fused breast images. This system can image an entire breast close to the chest wall to facilitate the detection and biopsy of small tumors without breast compression. This system has common emission (SPECT) and transmission (cone beam CT) FOVs that intersect each other, as opposed to being either on separate systems or linearly juxtaposed on separate gantries.

The CT component of the hybrid assembly was characterized for various system orientations and acquisition trajectories. Results of MTF evaluation in 3D show that there is little difference in the measured MTF throughout the volume regardless of the particular imaging geometry used. However, this may be due to the fact that an iterative algorithm is used to reconstruct the high contrast thin-line source data, after blurring the projection data by binning to 4×4 pixels.

Imaging results of plastic spheres suspended throughout the 3D breast volume and acquired using stationary polar tilted simple circular orbits demonstrated geometric distortions and reconstruction inaccuracies that manifest themselves as cupping artifacts. Slight blur was seen around the spheres near the edges of the FOV. Additional blur was progressively observed away from the flat plane of the cone beam, which had the more complete sampling using simple circular orbits and tilted source-detector angles. These artifacts are in addition to but are distinct from any scatter or beam hardening induced cupping artifacts, indicating that simple scatter correction algorithms present in some systems may overestimate the component, since the cupping artifact is a threefold feature in undersampled cone beam data. Cupping artifacts are thought to be comprised of: scatter, beam hardening and sampling. The latter two are intrinsically corrected for in our independent dedicated breast CT system since we use a quasi-monochromatic beam which virtually eliminates beam hardening^{10,16} and complex 3D sampling strategies to acquire more completely sampled cone beam projections of the breast as described previously^{11,12} and in this paper.

Currently in our prototype dual-modality system, the CmT component has a stationary tilt. Results indicate that by having the cone beam flat near the top of the breast allows for more complete sampling near the chest wall and more lesions can be clearly seen than for a completely sampled complex 3D trajectory. The drawback is that there are overlapping structures, geometric distortion, and incomplete sampling in the rest of the reconstruction volume. Therefore, for more distortion free images, use of complex 3D trajectories in imaging procedures having more complete sampling is suggested. The volume limitation issue of complex sampling may be ameliorated by lowering the object farther into the FOV, provided it is possible to do so. Specific design of a patient support apparatus is underway in our lab to try to accommodate this¹⁵.

ACKNOWLEDGEMENTS

This work was supported by NIH R01-CA096821, and in part by DOD W81XWH-06-1-0791, and DOD W81XWH-05-1-0280.

REFERENCES

- [1] P. D. Shreve, "Adding structure to function," *J Nucl Med* **41**, 1380-1382 (2000).
- [2] O. Israel, Z. Keidar, G. Iosilevsky, et al., "The fusion of anatomic and physiologic imaging in the management of patients with cancer," *Semin Nucl Med* **31**, 191-205 (2001).
- [3] T. F. Hany, H. C. Steinert, G. W. Goenes, A. Buck and G. K. vonSchulthess, "Improvement of diagnostic accuracy of PET imaging using an in-line PET-CT system - initial results," *Radiology* **225**, 575-581 (2002).
- [4] B. H. Hasegawa, K. H. Wong, K. Iwata, et al., "Dual-modality imaging of cancer with SPECT/CT," *Tech. Canc. Res. Treatment* **1**, 449-458 (2002).
- [5] O. Schillaci and G. Simonetti, "Fusion imaging in nuclear medicine: applications of dual-modality systems in oncology," *Cancer Biother Radiopharm* **19**, 1-10 (2004).
- [6] P. Madhav, D. J. Crotty, R. L. McKinley and M. P. Tornai, "Initial development of a dual-modality SPECT-CT system for dedicated mammotomography," 2006 IEEE Nucl Sci Symp & Med Imag Conf (2006).
- [7] D. J. Crotty, C. N. Brzymialkiewicz, R. L. McKinley and M. P. Tornai, "Optimizing orientation of SPECT and CT detectors through quantification of cross contamination in a dual modality mammotomography system," 2005 IEEE Nucl Sci Symp & Med Imag Conf **3**, 1672-1676 (2005).
- [8] D. J. Crotty, C. N. Brzymialkiewicz, R. L. McKinley and M. P. Tornai, "Investigation of emission contamination in the transmission image of a dual modality computed mammotomography system," 2006 Proc SPIE: Phys Med Imag **6142**, 664-674 (2006).
- [9] C. N. Brzymialkiewicz, M. P. Tornai, R. L. McKinley, S. J. Cutler and J. E. Bowsher, "Performance for dedicated emission mammotomography for various breast shapes and sizes," *Phys Med Biol* **51**, 5051-5064 (2006).
- [10] M. P. Tornai, R. L. McKinley, C. N. Brzymialkiewicz, et al., "Design and development of a fully-3D dedicated x-ray computed mammotomography system," 2005 Proc SPIE: Phys Med Imag **5745**, 189-197 (2005).
- [11] R. L. McKinley, M. P. Tornai, C. N. Brzymialkiewicz, et al., "Analysis of a novel offset cone-beam transmission imaging system geometry for accommodating various breast sizes," *Medica Physica* **XXI**, 46-53 (2006).
- [12] R. L. McKinley, C. N. Brzymialkiewicz, P. Madhav and M. P. Tornai, "Investigation of cone-beam acquisitions implemented using a novel dedicated mammotomography system with unique arbitrary orbit capability," 2005 Proc SPIE: Phys Med Imag **5745**, 609-617 (2005).
- [13] C. N. Brzymialkiewicz, M. P. Tornai, R. L. McKinley and J. E. Bowsher, "Evaluation of fully 3D emission mammotomography with a compact cadmium zinc telluride detector," *IEEE Trans. Med. Imag.* **24**, 868-877 (2005).
- [14] C. N. Brzymialkiewicz, R. L. McKinley and M. P. Tornai, "Towards patient imaging with dedicated emission mammotomography," 2005 IEEE Nucl Sci Symp & Med Imag Conf **3**, 1519-1523 (2005).
- [15] D. J. Crotty, P. Madhav, R. L. McKinley and M. P. Tornai, "Patient bed design for an integrated SPECT-CT dedicated mammotomography system," Presented at the 2006 Workshop on the Nuclear Radiology of Breast Cancer, San Diego, CA, 4-5 Nov. 2006, and published in 2006 IEEE Nuclear Science Symposium & Medical Imaging Conference Record.
- [16] R. L. McKinley, M. P. Tornai, E. Samei and M. L. Bradshaw, "Initial study of quasi-monochromatic beam performance for x-ray computed mammotomography," *IEEE Trans. Nucl. Sci.* **52**, 1243-1250 (2005).
- [17] P. Madhav, R. L. McKinley, E. Samei, J. E. Bowsher and M. P. Tornai, "A novel method to characterize the MTF in 3D for computed mammotomography," 2006 SPIE Med Imag Conf **6142**, (2006).
- [18] H. K. Tuy, "An inversion formula for cone-beam reconstruction," *SIAM J. Appl. Math.* **43**, 546-552 (1983).

Appendix G

Coauthor

SPIE 2006 Medical Imaging Conference – presented by Dominic Crotty - San Diego, February, 2006.

Investigation of Emission Contamination in the Transmission Image of a Dual Modality Computed Mammotomography System

Dominic J. Crotty^{1,2}, Caryl N. Bryzmialkiewicz^{1,2},
Randolph L. McKinley^{1,2}, Martin P. Tornai^{1,2}.

¹Department of Radiology, Duke University Medical Center, Durham, 27710 NC

²Department of Biomedical Engineering, Duke University, Durham, 27710 NC

ABSTRACT

A dual modality SPECT/CT computed mammotomography (CmT) system for dedicated functional/structural breast imaging is under development. In simultaneous, dual-modality imaging, contamination of the transmission (x-ray) image by emission photons from the uncompressed, pendant breast and torso is an important consideration in the design of hybrid imaging hardware. The lack of a collimator on the transmission image detector implies increased geometric efficiency of primary and scattered emission photons from the breast and neighboring torso region that potentially increase transmission image noise. This study investigates the nature and extent of this cross contamination. Projection and tomographic x-ray images are obtained with and without emission activity in a realistic anthropomorphic torso and various breast phantoms, and also with and without lead shielding on the torso for a variety of x-ray exposure times. Results for emission-source contamination of transmission images are quantified in terms of a mean and standard deviation of regions of interest. There was an observed trend of increased contamination with increasing emission radioactivity in the projection images when the x-ray detector was located immediately beneath the torso phantom, but no discernible effect when the detector was lateral to (and beneath) the torso. Torso shielding mitigated this contamination somewhat. Indeed, in reconstructed CmT data, there was both a decrease in SNR and concomitant decrease in mean attenuation coefficient with increasing emission radioactivity contamination. These results are consistent with the expected increased noise due to a uniform emission irradiation of the detector and hence the resulting apparent increase in detected x-ray transmission events (which yield a lower reconstructed attenuation coefficient value). Despite the emission contamination in both projection and reconstructed images, the contamination is uncorrelated, and indeed no reconstruction artifacts were observed under the various measured conditions. This indicates that a simple contamination correction may be possible to the projection data prior to reconstruction.

This work is supported by NIH grant R01-CA96821, and partly by DOD grants DAMD17-03-1-0558 and W81XWH-05-1-0280.

Keywords: Emission contamination, mammotomography, SPECT, CT, dual modality, flat panel detector

2. INTRODUCTION

The development of a compact, hybrid, dual-modality single photon emission computed tomograph and x-ray computed tomograph (SPECT/CT) for Computed mammoTomography (CmT), or dedicated breast imaging, has been previously described [1-3]. The CmT system is intended to be capable of independently enabling an essentially infinite number of orbital trajectories within a 3D hemispherical space around the patient's pendant, uncompressed breast for both the emission (SPECT) and transmission (x-ray CT) sub-systems. One of the consequences of using a dual-modality system is the potential for contamination of the image of one modality by the direct or scattered components of the other system's input [4,5]. This is also called cross-talk. In a recent previous study, we have investigated the cross-talk of the transmission signal from the quasi-monochromatic x-ray CmT system into the emission images [6]. We found that while there is definitely spatially dependent transmission contamination in the emission window due to the high x-ray flux (>1Mcps) relative to the lower detected emission events (~1kcps), both the offset cone beam breast imaging geometry used in our x-ray CmT implementation [2,3] and that energy windowing is employed for emission imaging virtually eliminated cross-talk to a <0.5% effect.

The purpose of this study is to quantify the observed contamination in the transmission-source CT image due to primary or scattered photons emitted from the patient's breast and torso region which are intended for the SPECT system. For

dual-modality imaging which yields both 3D functional and anatomical images, it is expected that a patient will be injected with a tracer quantity of a radiolabeled pharmaceutical and then will be scanned with one of several scenarios: (1) true simultaneous nuclear emission and x-ray transmission imaging; (2) interleaved emission then transmission (or vice versa) sequenced imaging; or (3) sequential transmission imaging during radiopharmaceutical uptake followed by emission imaging [7]. In our overall system design, the patient is expected to lie prone on a radio-opaque table specifically designed to expose one breast into both systems' fields of view (FOVs) while also shielding the rest of the patient from cross contamination and hence increased radiation dose [1-3].

In these studies, realistic breast and torso phantoms are filled with aqueous radiation and expose the x-ray detector in various orientations relative to the phantoms. The emission source used is ^{99m}Tc , a metastable isotope of ^{99}Tc that decays to its ground state by emitting a photon of approximately 140keV energy. Due to scatter in the phantoms, however, this discrete emission becomes a non-uniformly distributed energy spectrum of emitted photons described by the Klein-Nishina distribution probability and more simple Compton kinematics; it is these photons with a distributed spectral quality that can be incident on the uncollimated and otherwise unshielded digital flat panel CT detector. While the detector efficiency at 140keV is relatively low (<20%), it increases substantially as the energy of the incident photons decrease, up to nearly 100% efficiency at low energies. It is, therefore, reasonable to expect some level of transmission image contamination based on the known presence of radioisotope in the breast and torso phantoms.

Another factor that may impact the observed contamination is the physical position and orientation of the flat panel, digital x-ray detector relative to that of the patient. In describing a simple or complex x-ray CmT trajectory around the pendant breast, the relative position of the x-ray detector to the breast and torso regions of the patient will vary; thus, the observed contamination is likewise expected to vary.

2. MATERIALS AND METHODS

2.1 Equipment Used

Transmission source x-rays were generated using a *Rad-94* rotating tungsten x-ray source (*Varian Medical Systems*, Salt Lake City, UT). An non-conventional extrinsic 0.508 mm thick layer of Ce ($Z=58$, $\rho=6.657\text{ g/cm}^3$, $K\text{-edge}=40.44\text{keV}$, *Santoku America, Inc.*, Tolleson, AZ) metal filter material was placed in front of the source, providing a 100th value attenuating layer measured at a tube potential of 60kVp and yielding a quasi-monochromatic x-ray spectrum with mean energy $\sim 35\text{keV}$ and FWTM <30%. The x-ray detector is a 600 μm thick CsI(Tl)-TFT digital flat panel x-ray detector, model Paxscan 2520, (*Varian Medical Systems*, Salt Lake City, UT), with a 20x25cm² FOV and 1920x1536 pixels, 127 μm on a side. The intrinsic detection efficiency of this CsI detector for 140keV gammas is $\sim 19\%$. The design of the CmT imaging system has a compact source to image (SID) distance of 55cm, and the pendant breast of the patient is at the source to object distance (SOD) of 35cm. In practice, the chest-nipple axis of the patient will be placed laterally offset relative to the center of rotation for a half-cone beam type acquisition. In this study, the center of the breast was offset by 5cm. This laterally offset geometry requires a 360 $^\circ$ acquisition to completely sample the breast volume of interest. The radionuclide emission source investigated is ^{99m}Tc (140.6keV gamma ray), since this radionuclide is labeled to several functional breast cancer imaging compounds.

Three custom breast phantoms (*Radiology Support Devices*, Newport Beach, CA) were attached to a filled anthropomorphic torso. The breast phantom volumes were 325, 1060 and 1700 mL, representing small, medium and large sized breasts [8], respectively. The torso phantom provides a realistic non-uniform distribution and scatter medium for the radioactivity in the patient's chest and enables a more accurate quantification of the contamination likely to be seen in a clinical setting. In one set of experiments, a 1/4" thick lead plate covering a majority of the torso phantom is fastened to its chest to simulate the shielding anticipated by a radio-opaque patient bed.

2.2 Experimental Procedures

Both single projection and tomographic images which were then reconstructed were obtained to observe any effects on image quality (characteristics) due to the emission contamination. Projection data sets were acquired using each of the three breast phantoms, and CmT data was additionally obtained with a custom designed 3D orbit about the medium sized (1060ml) breast only.

The following three torso conditions were imaged in this study: (1) no radioactivity in the breast and torso region (or cold breast, cold torso = CBCT), which simulates a patient who has not been injected with a radiotracer for molecular imaging; (2) radioactivity in the breast but no radioactivity in the torso (or hot breast, cold torso = HBCT), which represents the ideally shielded patient, or one with an ideally localizing radiotracer, for both emission and transmission scans; and, (3) radioactivity in both the breast and torso (or hot breast, hot torso = HBHT), which simulates the worst case scenario of having a radiopharmaceutical injected patient and no bed shielding. An additional condition tested with the 1060mL breast was with tailored shielding attached to and covering a majority of the torso to mimic the intended bed shielding during a scan (or HBHT with Shielding = HBHTS).

Initial CBCT images of the breast and torso phantoms were used as baseline (control) images against which any contamination was measured. Radioactivity was then added to the breast via catheter, while keeping the torso phantom 'cold' to estimate contamination seen from the breast region alone. Radioactivity containing dye (to visually determine if there was adequate mixing) was also added to the torso in a similar way with a catheter. Absolute activity concentration ratios in the breast and torso region were $0.33\mu\text{Ci/mL}$, regardless of breast size, and are based on previously determined clinical uptake with $^{99\text{m}}\text{Tc}$ labeled radiotracers [9]. The imaging setup for the three breasts attached to the torso phantom and for the 1060mL breast with added lead shielding is shown in Figure 1.

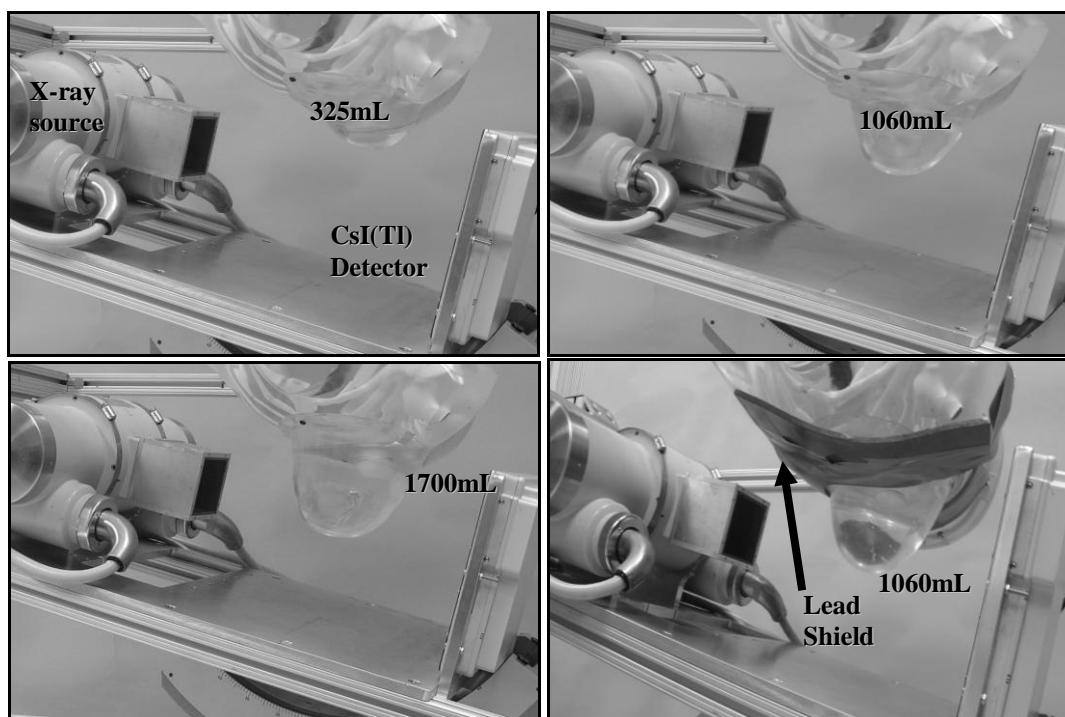


Figure 1. Images of the torso and various sized breast phantoms suspended into the CmT system field of view. The lead shield attached to the torso and 1060mL breast combination is also shown.

Images were acquired with the detector in two positions (Figures 2 and 3), with the detector in positions A (lateral to the phantom) and B (medial-inferior to the phantom), respectively. The positions are offset approximately 90° from each other. Projection images were acquired using the same x-ray exposure that is currently used for each CmT projection image acquired with this imaging system. Although the level of x-ray exposure remained constant (i.e. constant mAs), the breast was imaged using three tube exposure times, 40ms, 100ms and 250ms, to investigate the effect of exposure times on any contamination. The breast-torso combination was suspended in the field of view of the detector to the point where it was possible to image the anterior chest wall area of the torso phantom. Ten successive exposures were then acquired at each x-ray exposure time.

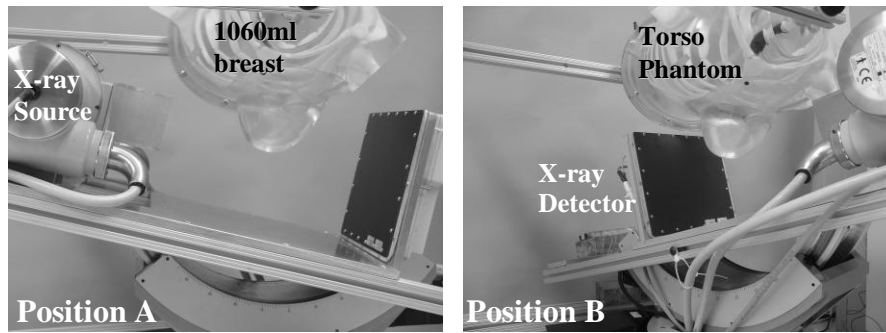


Figure 2. The x-ray system imaging the breast and torso phantoms in Positions A, medial-lateral to the torso, and B, in a superior-oblique vantage with respect to the torso, where the x-ray detector is immediately underneath the torso.

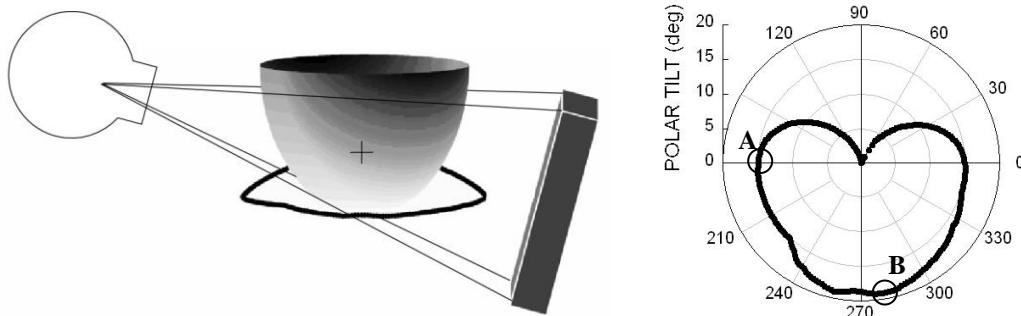


Figure 3. (Left) Perspective illustration of the x-ray detector traversing the custom-made 3D orbit (black “ring”) used to collect CT data of the 1060mL breast, along with (Right) a polar plot of the same orbit. In the polar plot, the circumferential direction indicates azimuthal change, and the radius indicates tilting in a polar direction. Points A and B, near the open circles, represent locations for the contamination measurements, and correspond to the vantages shown in Fig. 2.

To acquire CmT data, a custom 3D image acquisition orbit was generated with varying azimuthal and polar tilt angles that allowed close contouring and adequate sampling of the pendant 1060ml breast volume (Figure 3). CT data was acquired under the three conditions of radioactivity described above, with the control data being breast and torso without added radioactivity. The collected projection data was reconstructed in our standard way, using an iterative statistically based ordered subsets transmission algorithm described elsewhere [10]. Using the device control parameters which enable the 3D arbitrary orbit, as well as other pixel shifting, uniformity and line corrections, the projection data was reconstructed with 10 iterations and 8 subsets.

2.3 Image Analysis

To analyze projection images, four regions of interest (ROIs) were drawn (as shown in Figure 4 with the 1060ml breast) and the mean and standard deviation pixel value of each ROI obtained. Two ROIs were drawn inside the breast region (B #1, #2) and two in the background region (BG #1, #2), combined into two breast-background ROI pairs. One ROI pair (#1) was drawn closest to the top of the detector since this region was thought to see the largest emission contamination when the detector is placed below the torso region, as in position B. The other ROI pair (#2) investigates contamination closer to the nipple. Comparisons were made between mean and standard deviation values to identify trends in contamination with changing radioactivity levels/conditions in the breast and torso.

A standard deviation image was generated for each breast size from the multiple projection images taken under each radioactivity condition. This image was examined for any obvious areas of contamination caused by emission contamination.

The reconstructed CmT data was similarly analyzed, with an ROI drawn inside the breast volume in two orthogonal view planes, coronal and transverse. A signal to noise ratio (SNR) was calculated for each view under each of the three radioactivity conditions.

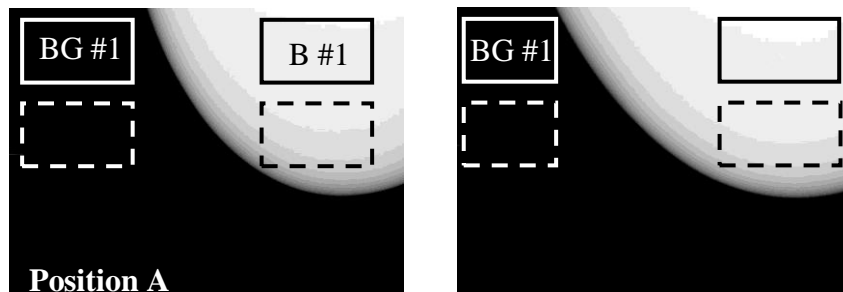


Figure 4. Projection images of the 1060mL breast phantom in positions A and B (see Fig. 2) with the placement of the breast and background ROIs superimposed on the images. For the image gray scales, dark means high exposure (pixel value), and lighter means less exposure.

3. RESULTS AND DISCUSSION

The level of observed contamination in the transmission image is expected to vary both with variations in the orientation of the imaging detector relative to the patient's body and in the exposure length of the transmission image. Image contamination is expected to be maximal when the detector is located directly below the torso of the patient (position B) and minimal in when located lateral to the patient (position A). Additionally, with the total x-ray flux kept constant so that breast dose would be at or below that of dual view x-ray mammography, a longer exposure time is expected to generate increased image contamination since proportionally more emission source decays can impact the imaging detector. However, since the count rate of the emitted radiation incident on the CmT detector is relatively small compared to that of the instantaneous x-ray flux, emission contamination may in fact be difficult or impossible to observe.

3.1 Projection Images: Position A

Figure 5 shows single sample images of each breast in position A. Projection images of the three breasts under all radioactivity conditions show very little variation, even when the image is tightly windowed. Figures 6, 7 and 8 show quantitative plots of mean and standard deviation values for both ROIs tested in the 325, 1060 and 1700mL breasts, respectively.

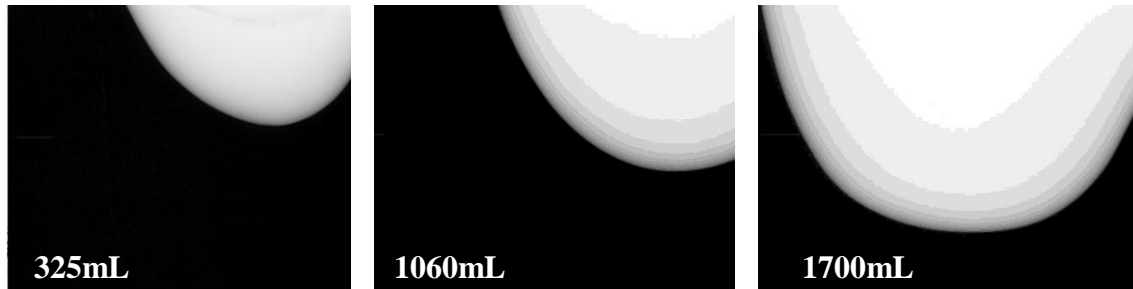


Figure 5. Sample projections of the three breasts acquired in position A. X-ray exposure is kept constant at 2.5mAs. For the image gray scales, dark means high exposure (pixel value), and lighter means less exposure.

Mean pixel values for either the breast or background ROIs do not indicate any clearly discernable trend in image contamination with a change in radioactivity of the breast when looking across all breast sizes. Indeed, values for the background ROIs are generally flat across the three states of radioactivity along with a similar absolute mean value across each breast size. Although there are clear differences between the mean breast ROIs from regions #1 (posterior breast) and #2 (anterior breast, near nipple), this can be easily explained by the increased x-ray penetration nearer the nipple where the breast is thinner. So, ROI #1 and #2 should not be compared with each other, per se, as compared across similar ROIs for the various breast and torso and exposure window configurations; in the latter case, no clear systematic trends are evident.

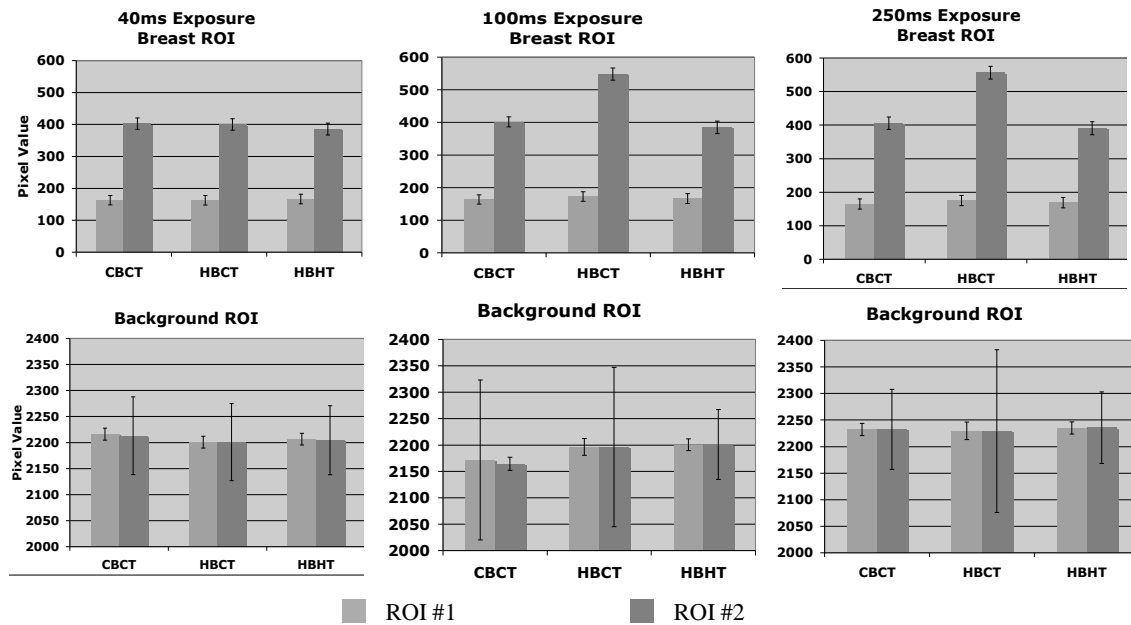


Figure 6. 325mL breast in Position A: mean and standard deviation (error bars) ROI pixel values for the breast and background obtained from the projection images. Note scale differences between breast and background ROI values.

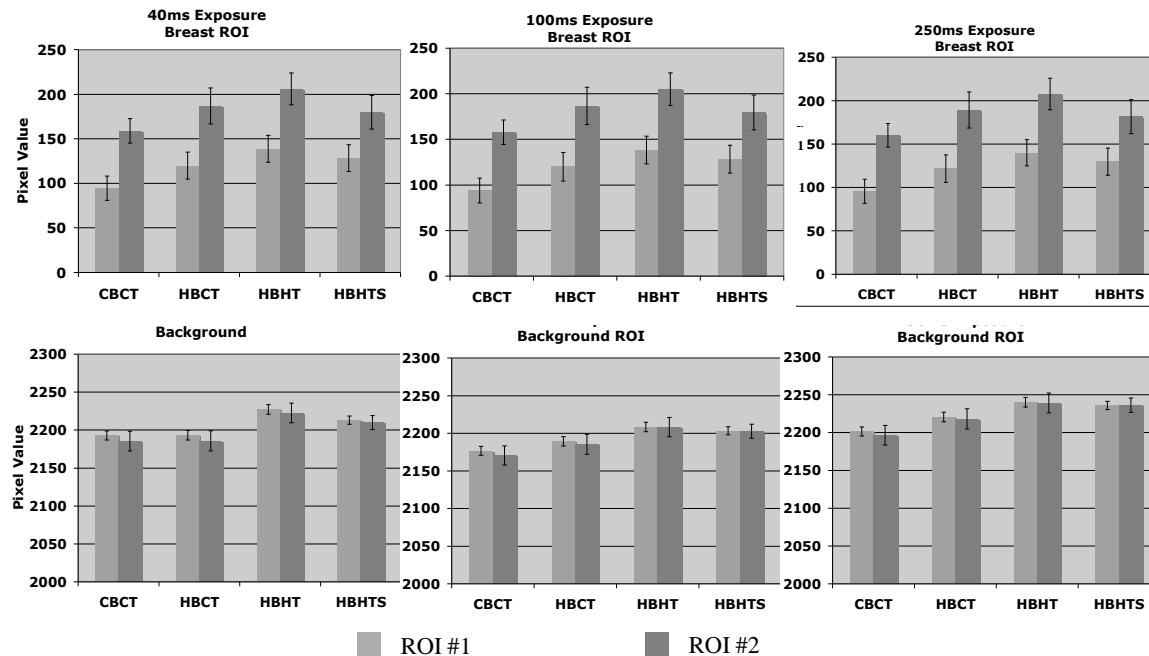
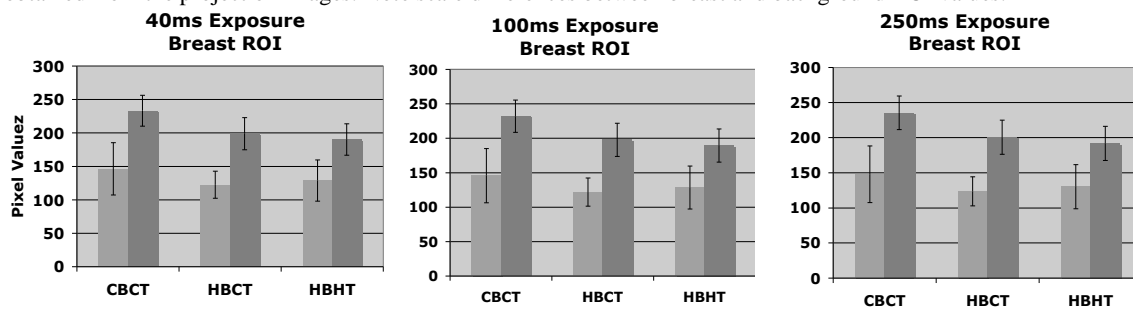


Figure 7. 1060mL breast in Position A: mean and standard deviation (error bars) ROI pixel values for the breast and background obtained from the projection images. Note scale differences between breast and background ROI values.



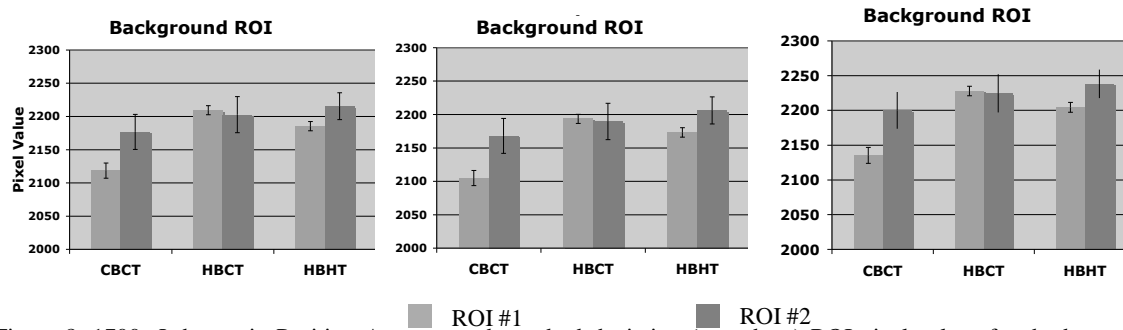


Figure 8. 1700mL breast in Position A: mean and standard deviation (error bars) ROI pixel values for the breast and background obtained from the projection images. Note scale differences between breast and background ROI values.

Additionally, there does not appear to be a variation in the mean values along with the greater than doubling of exposure times. While the x-ray flux is expected to be constant (equal mAs was used), one would expect that doubling the exposure time would allow a greater emission contamination on the transmission detector, but none is clearly evident. Extrapolating emission count rates from the breast only, across all energies measured with the SPECT system for emission imaging [9] to this current transmission detector scenario, there should be an approximate event rate density at the detector face of ~ 80 cps/cm².

Mean ROI pixel values for the 1060mL breast indicate increased image contamination with increasing levels of radioactivity. ROI values rise to a maximum for the unshielded HBHT case but slightly reduce when the torso is shielded, following an otherwise expected pattern of image contamination. Background and breast ROI values follow similar trends to each other.

One possible explanation for lack of systematic effects seen with the arrangement in position A is that, relative to the patient and x-ray source, the image detector is geometrically oriented in such a way as to limit the effect that emitted contamination has on the image compared to the x-ray flux. In this orientation therefore, it is possible that the effect of emission contamination is masked by that of the x-ray flux and subsumed by the intrinsic variations in source flux and intrinsic detector efficiencies.

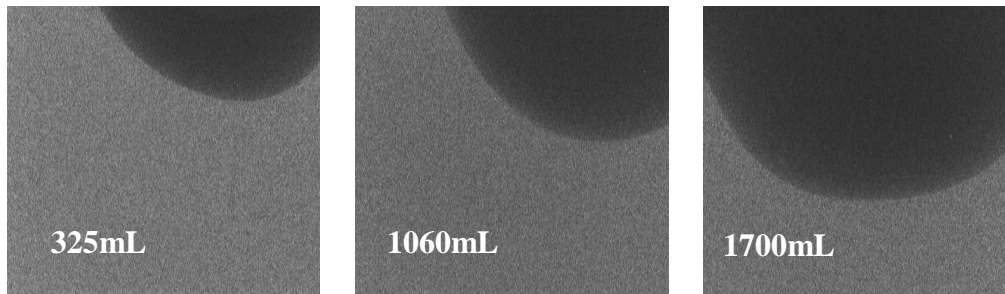


Figure 9. Standard deviation images of the three breasts. The breast images exhibit no spatially-dependent noise due to emission contamination. For the image gray scales, dark means high standard deviation, and lighter means less.

Standard deviation images of the 325, 1060 and 1700mL in position A are shown in Figure 9. As the images have a very uniform texture across the breast and background regions, it is reasonable to conclude that if there is indeed any contamination in the transmission image it does not appear to be spatially dependent emission contamination but rather is uniformly distributed across the entire image surface.

3.2 Projection Images: Position B

Shown in Figures 10 and 11 are the results of the mean and standard deviation ROI pixel values for the 1060 and 1700mL breasts in position B. In the current configuration, it was not physically possible to position the 325mL breast in the detector FOV in this position. In addition, it was also not possible to make adequate measurements with the lead shielding attached to the torso (HBHTS configuration) with the 1060mL breast in this position.

The results for both breasts in this Position B indicate that emission contamination affects the mean detected events, and thus may indeed play a role in tomographic transmission image formation. There is a systematic pattern of increasing mean ROI pixel value with increasing amounts and location (first in breast, then torso background regions) of radioactivity in the phantom.

The increases in ROI values are more apparent in the breast ROIs, but are also present to a lesser degree in the background ROIs. One possible explanation is that any incremental differences, e.g. those due to a uniform irradiation of the CmT detector plane, will be more clearly observable when a region has a low mean value. This is indeed the case for ROIs in the breast, which otherwise attenuates the x-ray flux, compared with the shine-by regions on the detector. Moreover, that there are relatively stable differences between ROI #1 and #2 in the background region, similar to the results for Position A, indicates that there is more likely a uniform distribution of contamination events rather than a position bias, such as from the torso which is situated directly above the detector in this Position B configuration.

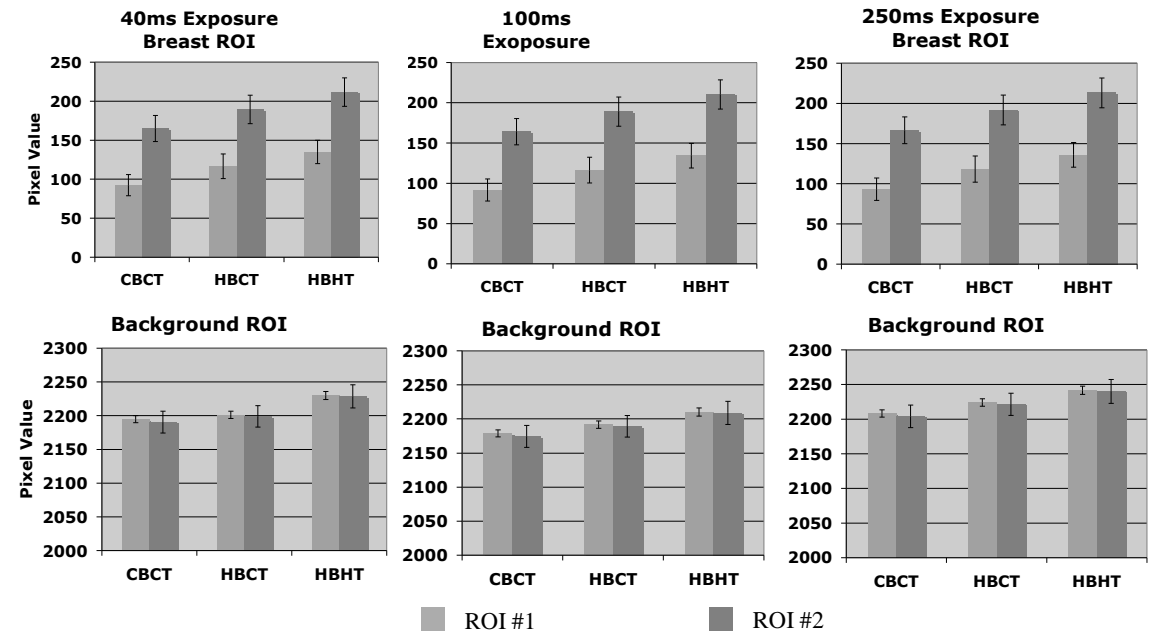


Figure 10. 1060mL breast, position B. Mean and standard deviation (error bars) ROI pixel values for the breast and background obtained from the projection images. Note scale differences between breast and background ROI values.

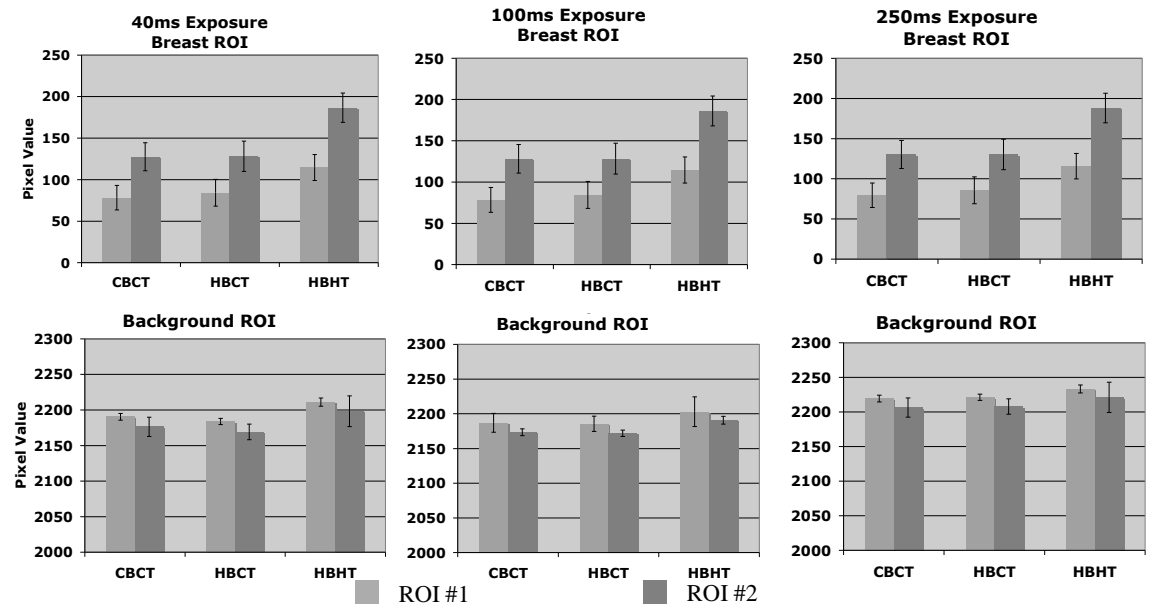


Figure 11. 1700mL breast, position B. Mean and standard deviation (error bars) ROI pixel values for the breast and background obtained from the projection images. Note scale differences between breast and background ROI values.

3.3 3D Reconstructed CmT Data

Transverse and coronal images of the 3D reconstructed 1060mL breast under various conditions containing radioactivity are shown in Figure 12. Images at each orientation are obtained from the same slice of the respective reconstruction, approximately midway into the imaged breast volume. SNR figures are also included in the images with the approximate position of the ROI superimposed on the first image. Signal is calculated as the mean of the ROI, and the noise is the standard deviation of the ROI.

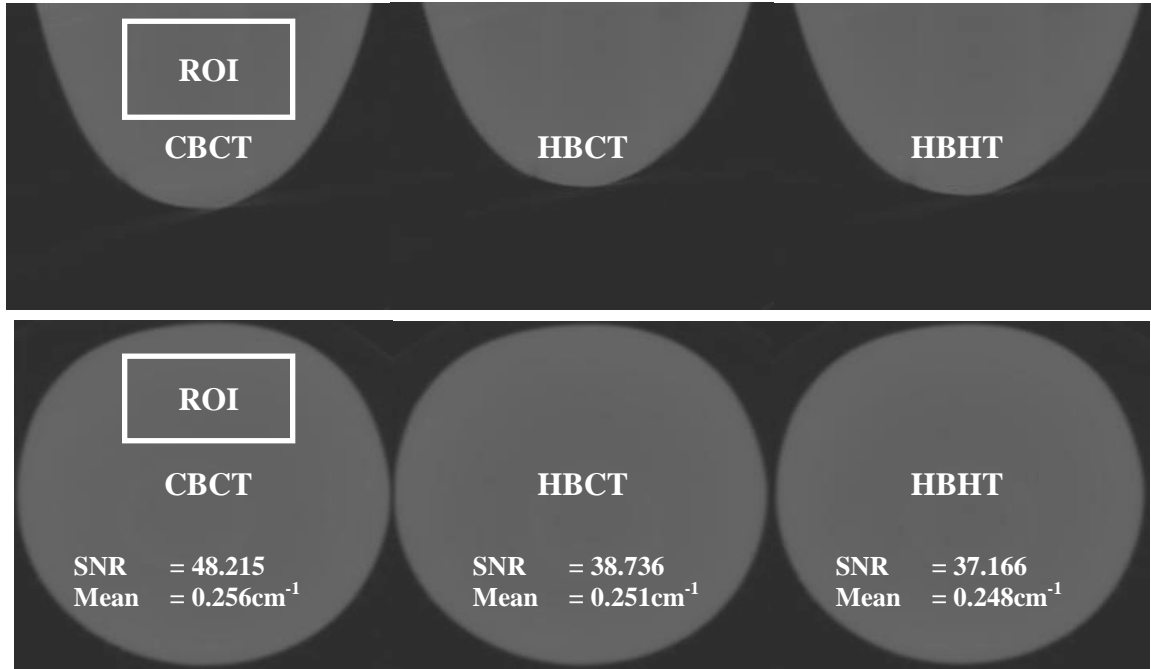


Figure 12. Reconstructed CmT data of the 1060mL breast. (Top) Transverse and (Bottom) coronal slices are shown with breast ROIs, SNRs and mean pixel values (attenuation coefficients) superimposed on the images.

The ROI SNR values decrease with increasing radioactivity in the breast and torso region. Taking the CBCT data as the true mean value, we see a large drop in SNR for the HBCT case in the coronal and transverse images. However, there is a smaller relative decrease in SNR values with greater emission activity in the HBHT case. Note also that there is a small decrease in the effective reconstructed attenuation coefficient (“mean” value in the ROIs) with increasing activity. The absolute attenuation coefficient of water with this beam technique is 0.2786cm^{-1} . These trends are consistent with the earlier observation (from the projections in Position B) that there are indeed events added to the projection images along with increased emission radioactivity added to the torso and breast phantoms. That is, small but increased detected events which are uniformly added in projection space will increase the apparent noise quality of an image, hence lower the SNR. Additionally, these increased events will positively add to the mean detected events and yield lower effective attenuation coefficients. Despite this emission contamination and increased image noise, there are no obvious systematic reconstruction artifacts in these images. This corroborates the notion that emission contamination among projection images is uncorrelated.

4. CONCLUSIONS

Results from projection images acquired with the flat panel x-ray detector lateral to a torso phantom containing radioactivity indicate that the intrinsic noise of the imaging system dominates any image noise introduced by emission contamination photons. When the flat panel detector is placed beneath the radioactive torso, emission photons impact longitudinally along the $600\mu\text{m}$ thick CsI(Tl) detector face, and the effective thickness of the detector increases, thus increasing overall detector efficiency. A systematic increase in emission contamination was noted with the detector in this position for all breast measured sizes. In the case when lead shielding was used between the torso and flat panel detector, decreased contamination was observed, indicating that a patient support palette that is somewhat radio-opaque would be useful for hybrid emission-transmission imaging.

Additionally, reconstructed CmT image data acquired with the medium sized breast and torso phantoms indicates a definite pattern of increasing image contamination with increasing radioactivity in those regions. Though there is a noticeable change in image SNR and measured effective attenuation coefficients, the effect on lesion contrast was not explicitly tested in this study and remains to be investigated. Given that this small change in attenuation coefficient is consistent with changes already present in CmT lesion imaging with our system [11], it remains to be seen if there will be any negative effect on lesion detectability with increased emission contamination. Results of this study indicate that contamination of the transmission image by photons emitted from the breast and torso regions in this dual modality setup is a factor in transmission image generation. Despite the emission contamination in both projection and reconstructed images, the contamination is uncorrelated, and indeed no reconstruction artifacts were observed under the various measured conditions. This indicates that, especially for quantitative CmT imaging, a simple contamination correction may be possible to the projection data prior to reconstruction.

REFERENCES

1. M.P. Tornai, J.E. Bowsher, C.N. Archer, R.J. Jaszczak. "Feasibility of Application Specific Emission and Transmission Tomography (ASETT) of the Breast." *J. Nucl. Med.* **42** (5), 12P (2002).
2. M.L. Bradshaw, R.L. McKinley, E. Samei, C.N. Archer, M.P. Tornai. "Initial X-ray Design Considerations for Application Specific Emission and Transmission Tomography (ASETT) of the Breast." *J. Nucl. Med.*, **44** (5), 287P (2003).
3. R.L. McKinley, M.P. Tornai, E. Samei, M.L. Bradshaw. "Development of an Optimal X-ray Beam for Dual-Mode Emission and Transmission Mammothomography." *Nucl. Instr. Meth. Phys. Res.*, **A527** (1), 102-109 (2004).
4. W.H. Wong, H. Li, J. Uribe, H. Baghaei, Y. Wang, S. Yokoyama. "Feasibility of a high-speed gamma-camera design using the high-yield-pileup-event-recovery method." *J. Nucl. Med.*, **44** (5), 24-32 (2001).
5. J. Yang, J.T. Kuikka, K. Jaatinen, E. Lansimies, L. Patomaki. "A novel method of scatter correction using a single isotope for simultaneous emission and transmission data." *Nucl. Med. Comms.*, **18** (11), 1071-6 (1997).
6. D.J. Crotty, C.N. Brzymialkiewicz, R.L. McKinley, M.P. Tornai. "Optimizing Orientation of SPECT and Cone Beam CT Detectors Through Quantification of Cross Contamination in a Dual Modality Mammothomography System." *IEEE Conf. Rec. Nucl. Sci. Symp. & Med. Imag. Conf.* 1672-1676 (2005).
7. B.H. Hasegawa, K.H. Wong, W.C. Barber, A.B. Hwang, A.E. Sakdinawat, M. Ramaswamy, D.C. Price, R.A. Hawkins. "Dualmodality imaging of cancer with SPECT/CT". *Tech. Canc. Res. Treatment*. **1**(6) 449-458 (2002).
8. M.P. Tornai, R.L. McKinley, C.N. Brzymialkiewicz, S.J. Cutler, D.J. Crotty. "Anthropomorphic Breast Phantoms for Preclinical Imaging Evaluation with Transmission or Emission Imaging." *Proc. SPIE: Physiology, Function, and Structure from Medical Images*, **5746**(2):825-834 (2005).
9. C.N. Brzymialkiewicz, M.P. Tornai, R.L. McKinley, J.E. Bowsher. "Evaluation of Fully 3D Emission Mammothomography with a Compact Cadmium Zinc Telluride Detector." *IEEE Trans. Med. Imag.* **MI-24**(7):868-877 (2005).
10. R.L. McKinley, C.N. Brzymialkiewicz, P. Madhav, M.P. Tornai. "Investigation of Cone-Beam Acquisitions Implemented Using a Novel Dedicated Mammothomography System with Unique Arbitrary Orbit Capability." *Proc. SPIE: Physics of Medical Imaging*, **5745**(1):609-617 (2005).
11. RL McKinley, MP Tornai. "Preliminary Investigation of Dose for a Dedicated Mammothomography System." Presented at the 2006 *SPIE Medical Imaging Conference*, 11-17 Feb. 2006, San Diego, CA, and submitted to *Proc. SPIE: Physics of Medical Imaging* (2006).

Appendix H

Coauthor

SPIE 2006 Medical Imaging Conference – presented by Dominic Crotty - San Diego, February, 2006.

Experimental Spectral Measurements of Heavy K-edge Filtered Beams for X-ray Computed Mammotomography

Dominic J. Crotty^{1,2}, Randolph L. McKinley^{1,2}, Martin P. Tornai^{1,2}

¹ Department of Radiology, Duke University Medical Center, Durham, NC 27710

² Department of Biomedical Engineering, Duke University, Durham, NC 27710

ABSTRACT

A compact, dual modality computed mammotomography (CmT) and single photon emission computed tomography (SPECT) system for dedicated 3D breast imaging is in development. The CmT component utilizes novel, heavy K-edge filtration to practicably narrow the energy spectrum of the cone-shaped x-ray beam incident on the patient's pendant, uncompressed breast. This quasi-monochromatic beam in CmT is expected to improve discrimination of tissue with very similar attenuation coefficients while restraining dose levels to below that of existing dual view mammography. Our previous extensive simulation studies showed the optimal energy range that provides maximum dose efficiency for a 50/50 adipose/glandular breast is in the 35-40keV range. This current study aims to experimentally validate previous simulation results. Here, experimental pre-breast and post-breast collimated x-ray beam spectral measurements are made under tube operating voltages between 40-100kVp using filter materials from Z=13-74, with K-edge values spanning that of Ce (K=40.4keV), and using different attenuating thicknesses of filter material, approximately equivalent to the 200th and 500th attenuating value layer (VL) thickness. Ce-filtered post breast spectra for 8cm to 18cm breasts are measured for a range of breast adipose/glandular compositions. Evaluated figures of merit include mean beam energy, spectral full-width at tenth-maximum, beam hardening and dose for the range of breast sizes. Measurements are shown to corroborate the simulations, and both indicate that for a given dose a 200th VL of Ce filtration may have the most optimal performance in the dedicated mammotomography paradigm.

This work is supported by NIH grant R01-CA096821, and partly by DOD grant W81XWH-05-1-0280.

Keywords: Filter, mammotomography, CT, quasi-monochromatic beam, beam hardening, K-edge

1. INTRODUCTION

A compact, versatile, computed mammotomography (CmT) system dedicated for breast cancer imaging is in development and has been previously described elsewhere [1-3]. This CmT system will ultimately be integrated with a single photon emission computed tomography (SPECT) system on a single, maneuverable gantry to produce a dual-modality dedicated breast imaging system that provides superior structural and functional information to be used in the detection of breast cancer. Previous simulation-based studies from our lab examined the feasibility, benefits and potential operating parameters of using a novel CmT beam filtration scheme using the K-edge of the filter material to produce a cone-beam shaped, near monochromatic x-ray spectrum [3,4]. To allow for full CmT imaging of the breast at dose levels equivalent to those of standard dual-view mammography, the mean energy of the incident x-ray beam needs to be increased. Prior studies, simulating a pure monochromatic x-ray beam imaging an uncompressed 15cm breast of 50-50% adipose-glandular composition with a 5cm embedded lesion, indicated that dose efficiency is optimized when using a beam with a mean energy between 35-40keV. The purpose of this paper is to validate results of those earlier simulation studies, compare measured spectra between several different filter materials, some common and others more novel metals for x-ray imaging, and additionally demonstrate the practicability of implementing the heavy K-edge filtration scheme in our system.

In addition to reducing absolute dose delivered to the patient and maximizing dose efficiency, the value of a quasi-monochromatic beam for 3D breast imaging lies in its anticipated ability to separate tissues with closely matching attenuation coefficients, thus allowing for improved discrimination between low-contrast objects (1-2% difference) like cancerous tissue and surrounding normal breast tissue [5]. Patients for whom 2-D x-ray mammography has proven to be inconclusive, such as those with large and mammographically dense breasts, may thus receive earlier and improved detection of tumors that might otherwise progress untreated.

2. EXPERIMENTAL METHODS

Spectral Measurement Equipment

Transmission source x-rays were generated using a *Rad-94* rotating tungsten ($C_p=138 \text{ J/kg}^\circ\text{C}$) x-ray source (*Varian Medical Systems*, Salt Lake City, UT) as shown in Fig. 1, with nominal Al intrinsic filtration. An x-ray generator, model CPX160 (*Electromed Inc.*, Montreal, PQ), provides the voltage required by the x-ray source. The maximum power output is 60kW for a tube potential range of 40 to 150kVp and a current range of 10-800mA. The design of the CmT imaging system has a compact source to image (SID) distance of only 55cm, and the pendant breast of the patient is centered at the source to object distance (SOD) of 35cm from the x-ray tube focal spot [1].

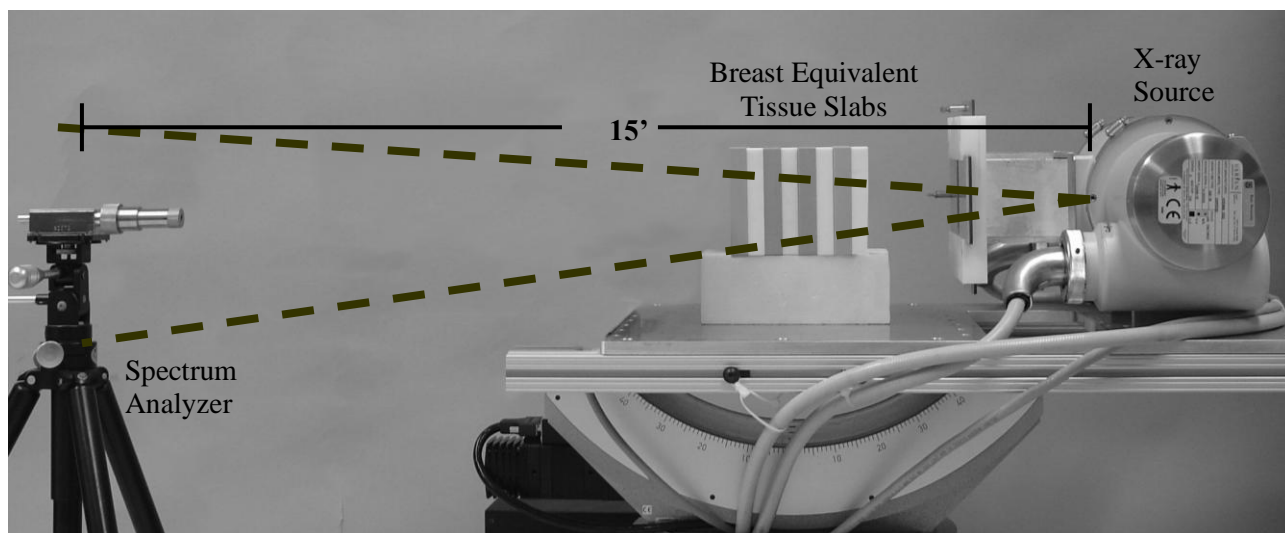


Figure 1. Experimental setup showing the x-ray source and partially collimated cone beam passing through slabs of breast (resting on styrofoam) equivalent tissue towards the spectrum analyzer. Note, the actual separation between the x-ray source focal spot and detector window is approximately 15 feet. For several measurements, the breast slabs were removed.

The CsI(Tl) *Paxscan 2520* (*Varian Medical Systems*, Salt Lake City, UT) imaging detector normally used for CmT was removed from the x-ray beam path. The spectrum analyzer is a *XR-100T-CdTe* high performance x-ray and gamma ray detector (*Amptek Inc.*, Bedford, MA.) with a 3 x 3 x 1mm cadmium telluride (CdTe) detector mounted on a thermoelectric cooler, possessing a typical noise resolution of <1.2keV full width at half maximum (FWHM). Calibration was carried out using an ^{125}I source with observable 27, 31 and 35keV peaks. The incident x-ray flux to the detector can be modified by placing collimated tungsten apertures of various diameters (25 μm – 2000 μm) in front of the thin beryllium detector window. This ensures that the observed count rate for a given x-ray pulse lay well below the maximum rate (20kcps) of the detector. To additionally reduce the flux incident on the detector face and thus avoid saturating the acquisition electronics, the detector was placed approximately 15 feet away from the x-ray focal spot. Other means to reduce the incident flux are being investigated [6]. Targeting the detector to the x-ray tube anode was accomplished visually using a pinhole laser inserted into the detector collimator housing, and adjusting the direction of until the laser shone directly onto the anode. Additional adjustments were made to try and ensure the detector face lay along the central ray of the incident x-ray beam, as slight misalignments can lead to reduced detection of source flux. To account for geometric misalignments, hence loss in observed flux (i.e detected x-ray event quanta), the integral measured spectra are normalized to the simulated exposure of the tube for the purposes of analysis. Studies with a RadCal exposure meter (*model 1515*, *RadCal Corp*, Monrovia, CA) have previously confirmed that the measured exposure at isocenter is equivalent to simulation derived exposure values. This discrepancy between the exposure determined from the integral measured spectrum at 15' and the exposure measured at isocenter is also partially due to the ~20% beam attenuation in air, given the large separation distance between source and spectrum analyzer.

Simulation Code

X-ray cone beam spectra were simulated using *xSpect*, a simulation code developed at Henry Ford Health Systems (Detroit, MI) and based on a semi-empirical x-ray generation model. This has been described in detail elsewhere [4]. Scatter-free spectra were simulated from a tungsten target having nominal intrinsic oil and aluminum filtration with tube potentials ranging from 40 to 100kVp in 20kV increments. Also simulated were filtered x-ray beam spectra produced using filters of various materials and attenuation value layer (VL) thicknesses shown in the Table I, and described below.

While there are several outputs from an *Xspect* simulation including the incident and (scatter free) transmitted energy spectra, exposure, signal over a lesion, noise, etc., absorbed dose was not an explicit *Xpsect* output parameter. Thus, the absorbed dose was calculated for a 50% adipose/50% glandular breast composition based on Monte Carlo derived dose conversion tables for our specific CmT geometry provided by Boone [8]. Dose tables included 50/50 breast composition for breast sizes ranging from 10 to 18cm (including a 0.5cm thick skin layer), with dose coefficients in units of microGy/10⁶ photons/mm² in 1keV increments. These coefficients are therefore normalized to a fixed number of photons and can be used together with *Xspect* derived and measured (see next section) spectral data (in units of photons or detected counts/mm²/keV) to calculate glandular dose. Glandular dose is derived based on the assumption that glandular tissue dose is the most important consideration in assessing ionizing radiation risk to the patient.

TABLE I. Filter materials and thicknesses used to acquire pre breast spectra

Elemental Filter	Z	Purity (%)	Density (g/cm ³)	K-edge Energy (keV)	200thVL (mm)	500thVL (mm)
Aluminum ^a	13	97.9	2.70	1.56	23.96	30.62
Copper ^b	29	99.9	8.92	8.98	1.02	1.03
Silver ^b	47	99.998	10.49	25.51	0.3	0.4
Cerium ^c	58	99.9	6.89	40.44	0.71	0.91
Neodymium ^c	60	99.9	6.80	43.57	0.7	0.93
Europium ^c	63	99.9	5.24	48.52	1.00	1.25
Tungsten ^b	74	99.95	19.25	69.53	0.20	0.25

a. 6061 Aluminum

b. Alfa Aesar, Ward Hill, MA.

c. Santoku America Inc., Tolleson, AZ.

Pre-Breast Spectral Acquisitions: Intrinsic Filter Measurements

Pre-breast spectra were acquired using the 7 different filter materials detailed in Table I according to the setup in Figure 1, without the breast slabs along the beam path. Aluminum and copper are filter materials commonly used for beam filtration in commercial x-ray systems and have relatively low K-edges compared to the other tested filter materials. Silver has a K-edge that is near that of Molybdenum and Rhodium, two materials most commonly used in standard x-ray mammography. Cerium has a K-edge at an energy previously shown to have advantageous characteristics for dedicated breast CmT [3,4]; two other rare earth metals with similar K-edge energies, Europium and Neodymium are included as practical alternatives to Cerium. Tungsten, another common filter material, with a K-edge higher than that of Cerium, is also included for the purposes of comparison, similar to Aluminum and Copper.

The individual filter thicknesses correspond approximately to the 200th and 500th attenuation value layer (VL) of filter material. These attenuating value layer thicknesses are energy dependent and the specific thicknesses were determined using *xSpect* with a tube operating voltage of 60kVp. This tube voltage was chosen since it lies in a relatively smooth region of the attenuation coefficient curves of all of the above materials, away from any K-edge discontinuities that might otherwise bias the resultant material thicknesses. Practical limitations in obtaining exact metal thicknesses mean the values in Table I are the closest approximation to the stated attenuation value layers. The particular VL figures were chosen by considering tube heating effects, where a 500th VL represents the upper limit of filter material thickness for this system under expected clinical operating conditions. The 200th VL filter then represents one possible filter thickness for practical daily clinical use.

Four separate x-ray tube operating voltages, from 40 to 100kVp, in 20kV increments were investigated. These operating voltages span a range that includes the low voltage more typical of current x-ray mammography, to a higher tube voltage that could provide higher mean beam energies and higher overall flux. To standardize flux, a constant x-ray source exposure of 0.4mAs was used for these pre-breast spectral studies.

At each voltage setting and for each filter material and thickness, the collimated x-ray source was exposed multiple times until approximately 100 detected counts were present in the peak of the detected spectrum. Comparisons between different filter materials were then possible by normalizing the number of exposures and the aperture diameter in front of the spectrum analyzer.

Absorbed dose for breast sizes ranging from 10-18cm were calculated using previously generated tables of dose. Measured and simulated spectra were exposure normalized as described above. Trends in absorbed dose as a function of filter material were then estimated.

Post-Breast Spectral Measurements: Effect of Breast Thickness and Composition

The effect on the filtered x-ray spectrum after it passes through breast materials of varying densities and thicknesses was also measured. It is this beam that impinges on the flat-panel imaging detector, so determining and hence optimizing the characteristics of this post-breast beam are paramount to ensuring the best possible image. Based on the overall results of the first measurement section of this study, Cerium was chosen as the filter material to further test here. Earlier studies for CmT led us to conclude Cerium as a near-ideal filter, and the results of the current study further corroborate these conclusions.

Stacks of breast tissue equivalent plates, each 2.0cm thick (*CIRS Inc.*, Norfolk, VA) having either 100% glandular or 100% adipose composition (ICRU-44 specifications) were centered at the system isocenter (35cm from the focal spot) to represent uncompressed breasts of various thicknesses and densities in the beam path. Figure 1 shows a 16cm breast equivalent tissue setup with the center of the breast placed at the isocenter of the CmT system. The total number of equivalent breast material slabs was varied to create breast tissue of thickness ranging from 8 to 18cm. These two breast diameters bound the majority of breast sizes seen clinically, and results for breast diameters outside this range could be extrapolated from those investigated here. Composition of breast material along the beam path was also varied to span the range of possible breast tissue densities, from 100% glandular to 50-50% glandular-adipose tissue and 100% adipose tissue.

Cerium filters of thickness approximately equivalent to a 200th and 500th VL along with an unfiltered beam, were used with this setup. Tube operating voltages spanned 40 to 80kVp in 20kV increments. In order to get higher count rates through the breast, larger x-ray exposures, ranging from 1.6 and 10mAs, were used in this section compared with the earlier intrinsic filter measurements. In this section of the study, the detector was exposed to 100 pulses of the x-ray source in order to normalize the spectra.

Quantitative Analysis

Common figures of merit (FOMs) for both pre- and post-breast spectra used previously [4] are mean beam energy and full width at tenth-maximum (FWTM). Mean beam energy is calculated using the first moment, or weighted mean of the spectral distribution of the x-ray beam.

The FWTM is used to indicate the degree of monochromaticity of the x-ray beam incident on the breast in the FOV of the x-ray system. Although FWHM is the traditionally cited metric for spectral resolution, this may neglect the presence of other features (e.g. a low intensity, yet broad energy distribution) that could otherwise bias the spectral broadening. For example, while a traditional mammography spectrum may have sharp (i.e. narrow FWHM) characteristic x-rays, their integral intensity is usually less than the integral intensity of the broader underlying bremsstrahlung spectrum from the same tube. Thus, a higher overall degree of monochromaticity could be expected with a spectrum having a lower FWTM metric.

Additionally, the FOM calculated in the second section of the study was an index of beam hardening, calculated as the ratio of weighted mean energies of the pre- and post-breast x-ray beams. Although image processing techniques can minimize the image effects of beam hardening (seen as cupping in CT images), these artifacts may still reduce intrinsic image quality. While an alternative approach is to model the energy spectrum during the reconstruction process [8], our overall approach to CT is to use a quasi-monochromatic beam for minimal beam hardening with the added benefit of potentially reduced dose to the object.

3. RESULTS AND DISCUSSION

3.1 Pre Breast Spectra

Figure 2 shows a variety of simulated and measured spectra for a 60kVp x-ray beam without any filter (0th VL) and with an equivalent 200th and 500th VL Cerium-filtered beam. The plots illustrate the dramatic change in spectral quality when ultra-thick K-edge filtering is used. The most obvious visual characteristic is the increasing monochromaticity of the filtered beam compared to the more polychromatic, unfiltered beam most clearly seen in the superimposed simulation curves. The effect of the ultra thick filter is to eliminate lower energy photons with the higher energy photons eliminated by the K-edge absorption. Consequently the mean filtered beam energy is concentrated around the K-edge of the filter material.

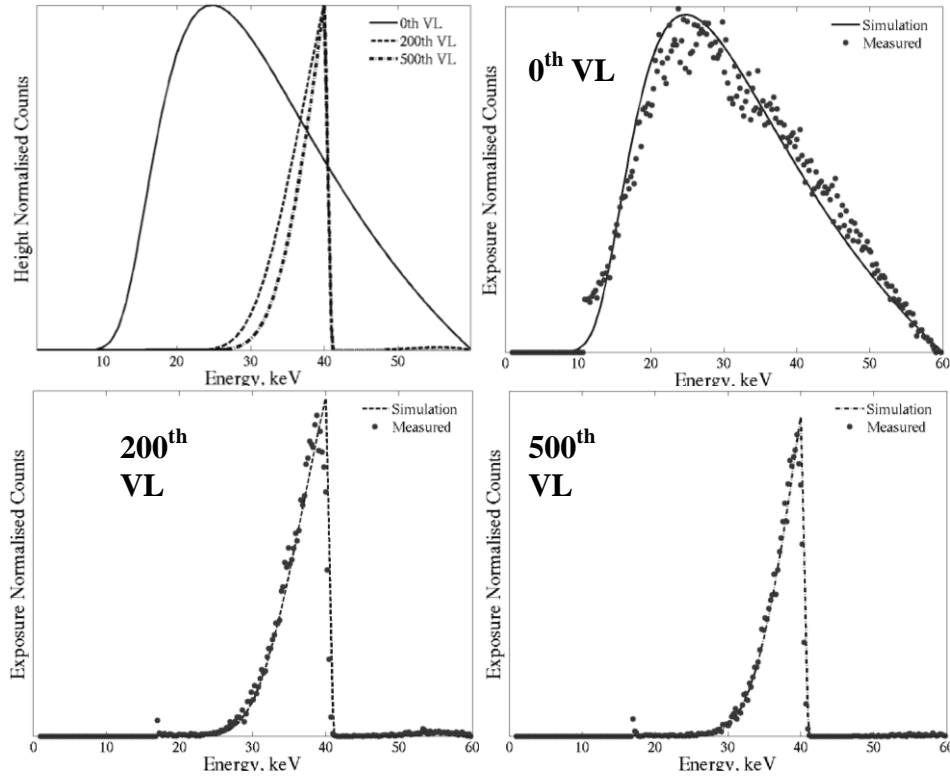


Figure 2. Plots of simulated and measured spectra at 60kVp for 0th VL (unfiltered beam), 200th VL and 500th VL filtered spectra showing increased monochromaticity as the filtration increases

In the current study, both 200th and 500th VL filtered beams were investigated and data collected for both. While acquiring spectra, however, it was determined that tube heating potentially biases the decision against routine use of the 500th VL filter for frequent CmT acquisitions. Henceforth, the emphasis in presented results will be on the 200th VL filter.

Figure 3 illustrates the simulated and experimental results of using a 200th VL Cerium filter on the raw x-ray beam at three tube operating voltages: 40, 60 and 80kVp. Visual agreement of experimental and simulated data is excellent. Comparing the filtered beams at 60 and 80kVp, the excess high-energy photons at the higher operating voltage gives a bimodal quality to the spectrum and this degrades the monochromatic nature of the x-ray beam. While for computed tomography a higher voltage on an unfiltered beam may be preferable for minimizing dose to the patient, these resulting high energy photons may reduced object contrast. With the use of heavy K-edge filtration, too high a tube operating voltage (i.e. 80kVp) leads to a bimodal spectrum which may similarly lower object contrast as an unfiltered beam. Therefore, to preserve a narrow energy band, an operating tube voltage of 60kVp may be preferred.

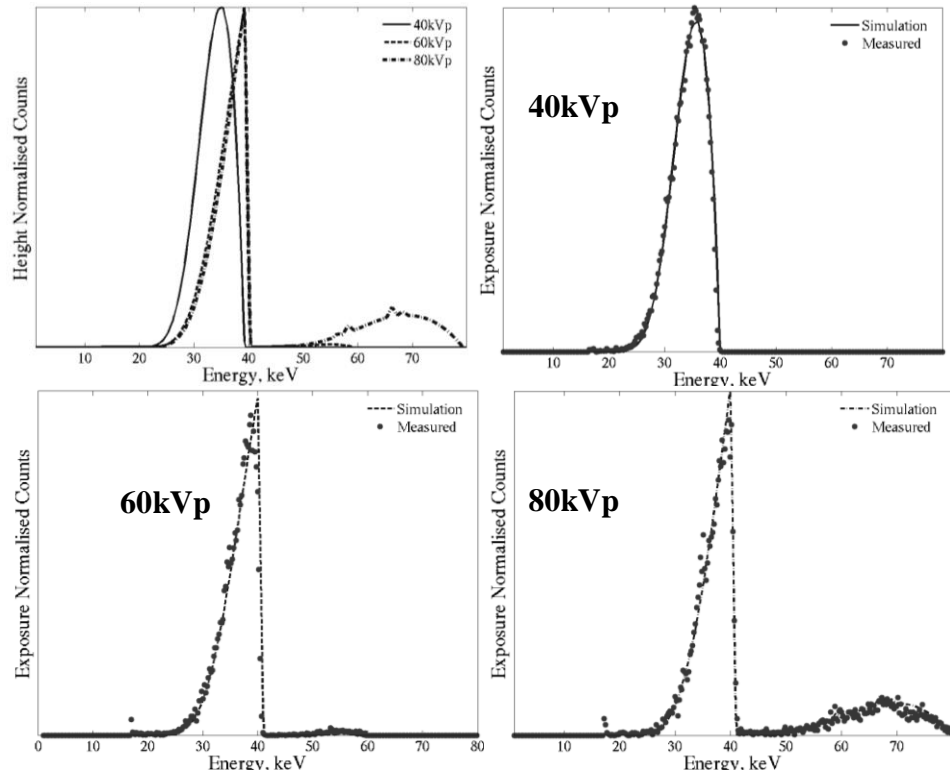


Figure 3. Plots of simulated and measured 200th VL Ce filtered spectra for 40, 60 and 80kVp spectra showing changes in spectral quality as the tube voltage increases up to 60kVp.

Figure 4 is a comparison plot of pre-breast spectra acquired using all 7 filters in the study at a tube voltage of 60kVp and a filter thickness approximately equivalent to 200th VL (Table I). A sharp cutoff is evident in detected photons at energies higher than the K-edges of the respective lanthanide filters, leading to more quasi-monochromatic spectra when compared to the filter materials with both lower and higher K-edge energies.

A comparison of simulated and measured average pre-breast beam energy as a function of atomic number of the filter material is shown in Figure 5 for noted combinations of a 200th and 500th VL filtered beam at 60 and 80kVp. At 60kVp, the mean beam energy for the Cerium filter with either a 200th or 500th VL lies directly in the range of beam energies for optimum dose efficiency described in the introduction. Since this optimum dose efficiency region is affected by breast and lesion size (more so than by breast composition), other lanthanide metals such as Europium and Neodymium may also be appropriate for dedicated breast CmT as alternatives to Cerium for larger breasted women.

A comparison of FWTM results for each of the measured and simulated pre-breast filter materials are plotted in Figure 6 for a 200thVL attenuation layer and tube voltages of 60 and 80kVp. Agreement between measured and simulated data is quite close for most filter materials. Error is greatest where the effect of low energy noise on the data is most pronounced, as seen in Fig 5. At 60kVp, the highest degree of monochromaticity i.e. lowest FWTM, is seen for the Cerium filter where the effect of the K-edge is to essentially eliminates photons beyond 40keV. At the higher tube voltage of 80kVp, the effect of the Cerium K-edge is reduced and allows some higher energy photons break through, as seen in the 80kVp spectrum illustrated in Figure 3, thus broadening the Cerium spectrum. It may be that Neodymium is a better choice of filter material to generate a more stable quasi-monochromatic spectrum for a broader range of tube operating and breast composition conditions.

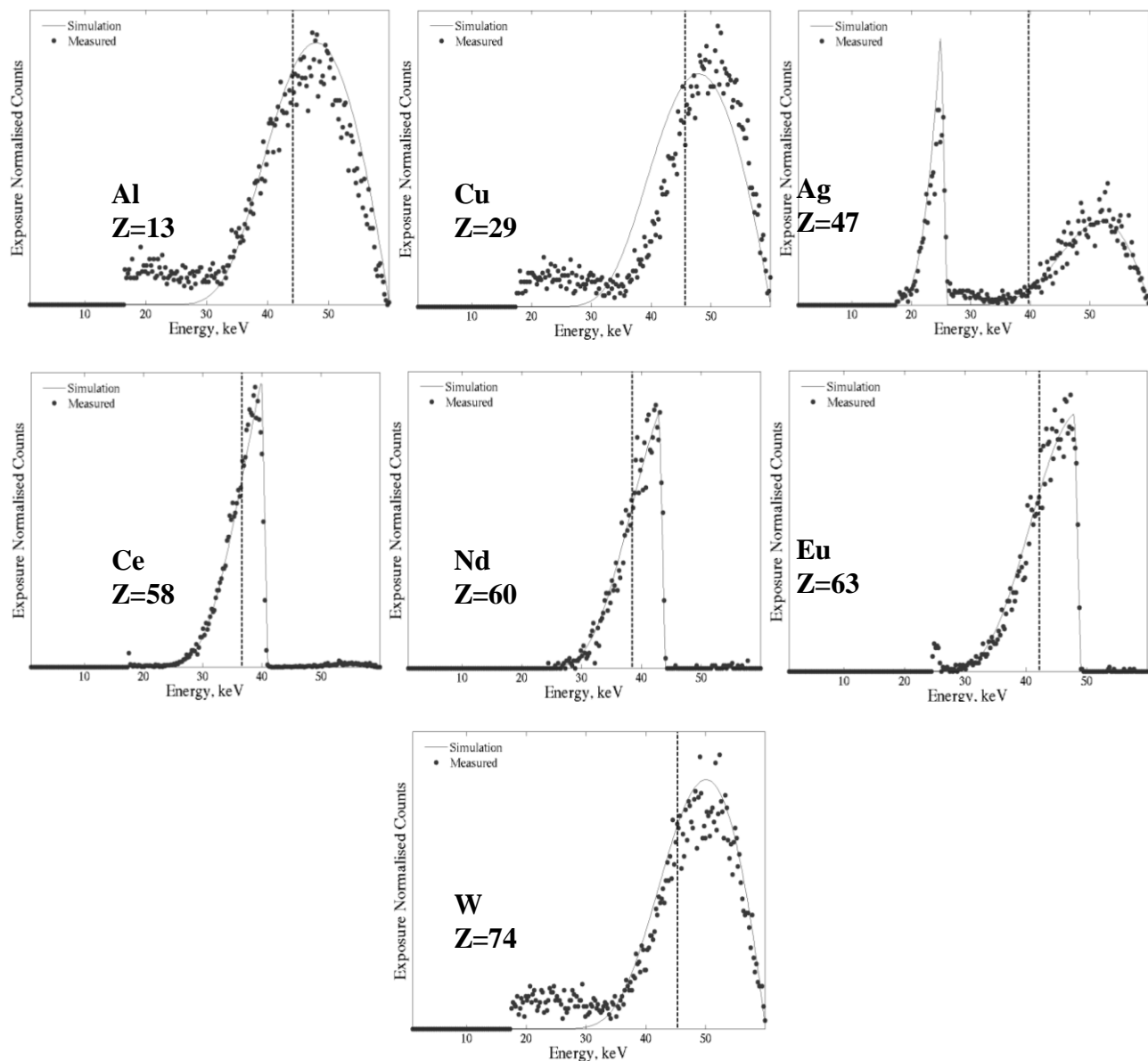


Figure 4. Exposure normalized pre-breast measured spectra with various filters superimposed with simulated spectra. Spectra are acquired at 60kVp and 200thVL. The mean beam energy for each filter is illustrated with a vertical dashed line.

A plot of absorbed dose (in μGy) for a range of breast thicknesses from 10cm to 18cm are shown in Figure 7 for all filters used in the first section of this study. The plots are from data with a tube voltage of 60kVp at a filter thickness of 200th VL. Cerium is shown to have the lowest dose for breasts of all thicknesses under these particular conditions. Since the simulations are set up for identical mAs and this implies equal image SNR, one can infer that the dose efficiency (SNR^2/Dose) inherent in this setup is a maximum across these breast sizes with the use of a Cerium filter.

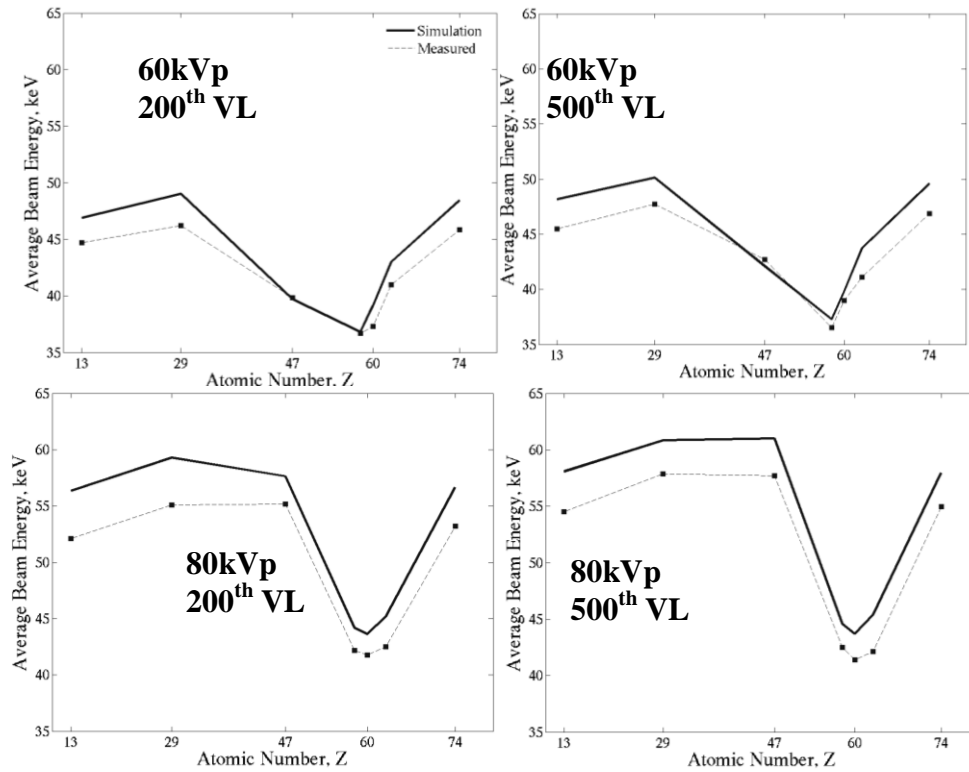


Figure 5. Simulated (lines) and measured (broken line with data points) weighted average beam energy for pre breast filters at given atomic numbers for various listed conditions.

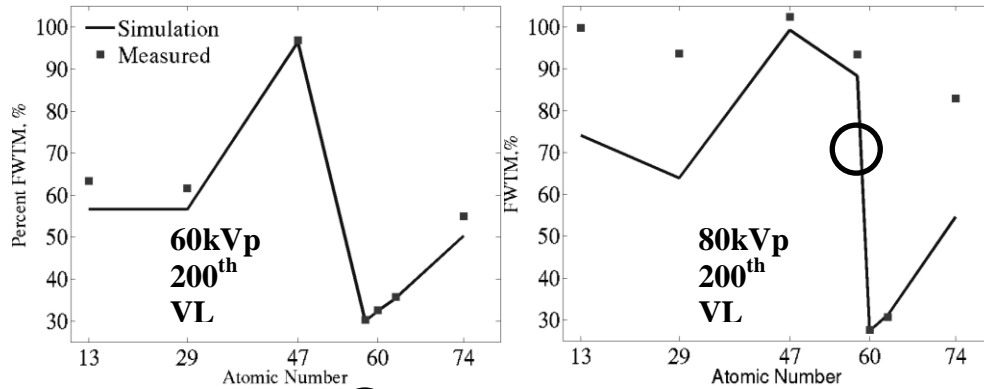


Figure 6. Measured and simulated FWTM values plotted as a function of atomic number of the filter materials. Cerium (circled), $Z=58$, exhibits the minimum FWTM of this set of metals at 60kVp but, due to the breakthrough shown in Figure 3, has much greater spectral broadening at 80kVp indicating, for example, that Neodymium may be a better choice of filter material if the tube is operated at this higher voltage.

3.2 Post-Breast Results

Figure 8 shows exposure-normalized unfiltered and 200th VL filtered pre- and post- breast measured spectra at 60kVp along with *xSpect*-generated spectra for a 16cm breast of 100% glandular composition. Though the unfiltered spectra are generally noisy due to the broad spectrum and exposure normalization, overall agreement is good between measured and simulated data. Note the dramatic change in average energy, indicated by straight lines on the plots, of the post-breast beam for the unfiltered beam as opposed to the relatively minor change for the heavily filtered beam

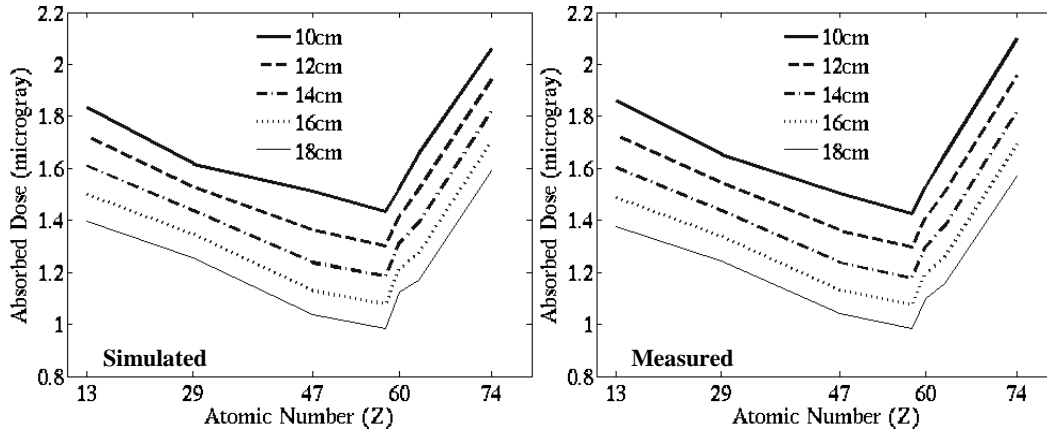


Figure 7. Plots of dose calculated from exposure normalized simulated and measured energy spectra for filters operating at 60kVp and 200th VL for a range of breast sizes from 10-18cm with a 50-50% Adipose-Glandular breast tissue composition. Trends illustrate a minimum in absorbed dose for heavy K-edge filtration with Cerium.

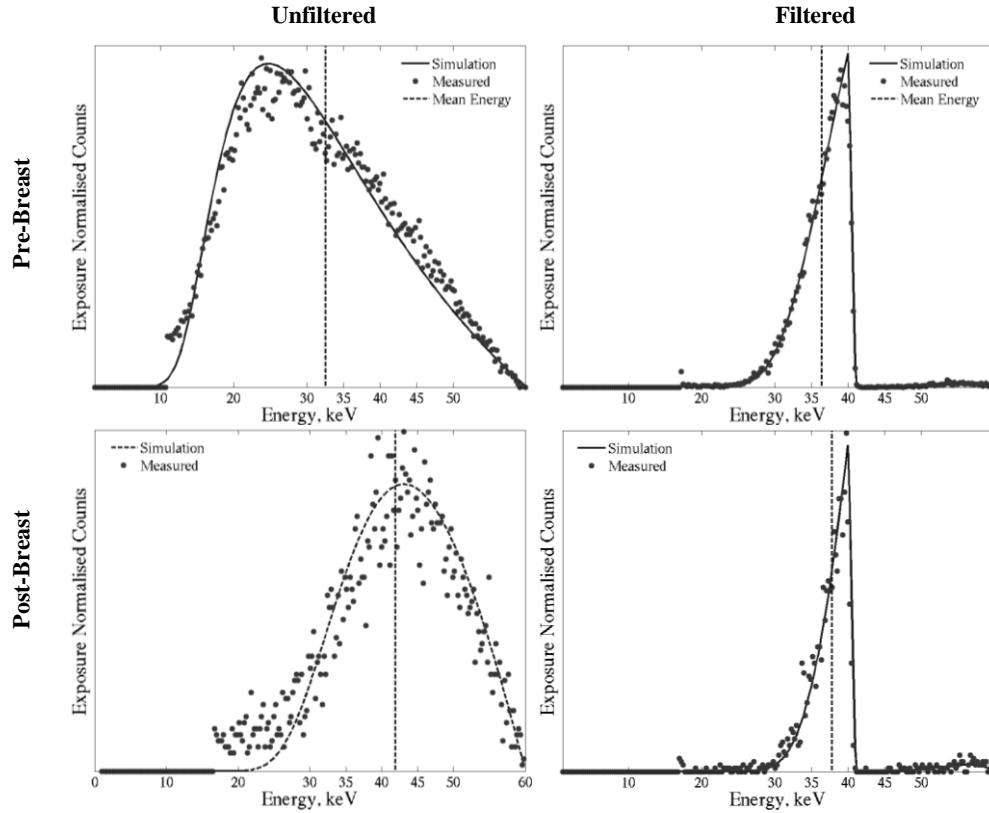


Figure 8. Simulated and measured spectra for pre-breast (top row) and post-breast (bottom row) unfiltered (left column) and 200th VL Ce filtered (right column) beam through a 16cm thick breast of 100% glandular composition. Vertical dashed line indicates the weighted mean beam energy.

The shift in mean beam energy of the pre- and post- breast spectrum for the unfiltered beam also shows a high degree of beam hardening (Fig. 8). Table II lists minimum and maximum degrees of measured beam hardening in the study across all breast compositions and thicknesses under all operating voltages and filter thicknesses. In general, beam hardening is seen to increase, i.e. worsen, with increasing thickness of breast tissue and also with increasing glandular composition. Results are best for the thickest filter, but the proportional improvement between the 500th and 200th VL filter is dwarfed by the improvement between the 200th VL and the unfiltered beam. While a small beam hardening emphasizes the improvement in beam quality, a corresponding improvement in image quality might be expected when a filtered, quasi-monochromatic beam is used in a dedicated breast CmT imaging system.

Table II Measured Beam Hardening at 60kVp across all experimental setups.

Breast Thickness	Beam Attenuation Value Layer								
	Unfiltered			200 th VL			500 th VL		
	% Glandular Tissue			% Glandular Tissue			% Glandular Tissue		
	0	50	100	0	50	100	0	50	100
8cm	19.1	17.5	14.2	3.	1.34	3.99	0.98	1.41	1.25
12cm	17.0	20.0	22.7	1.78	2.35	2.68	0.74	1.11	1.42
16cm	19.6	23.0	25.8	2.25	2.78	3.71	0.86	1.12	1.82
18cm	20.1	24.4	26.1	2.18	2.70	4.44	0.78	1.09	1.95

Finally, spectral broadening of the post-breast spectrum for a 16cm thick breast across all breast densities at a tube voltage of 60 and 80kVp are shown in Figure 9. At 60kVp, there is a threefold improvement or reduction in spectral broadening for a 200th VL beam as compared to the unfiltered beam, indicating much greater monochromaticity in the beam now incident on the imaging detector. Improvement in FWTM figures for 80kVp are not as pronounced, reinforcing the suggestion that higher voltages may not be ideal for routine tube operation. The difference between measured and simulated values is most pronounced for the unfiltered beam, where noise in the measured beam spectra is highest. Though measured results in the 80kVp case follow simulated results less closely, the trend in results is the same.

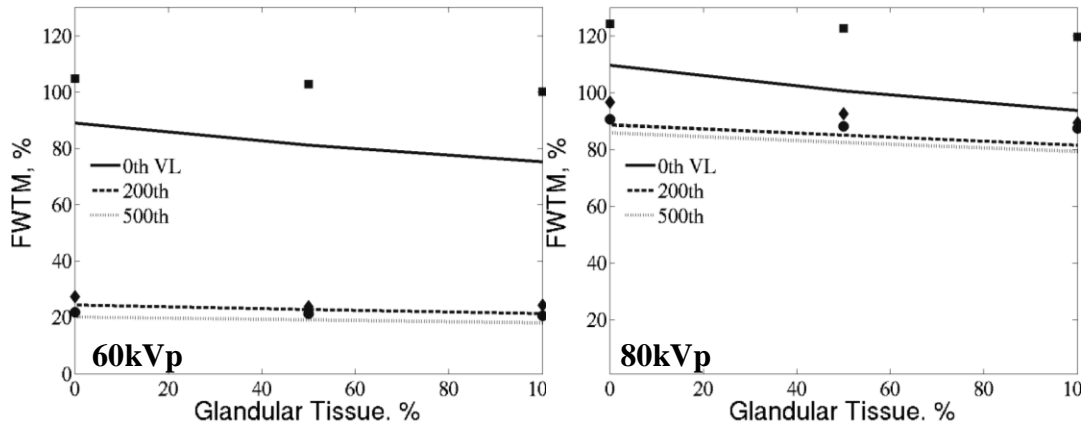


Figure 9 Simulated (lines) and measured (data points) FWTM at 60 and 80kVp for 16cm breasts of varying density for 0th VL (unfiltered beam), 200th VL and 500th VL Cerium filtration. The key for measured data is indicated on Figure 9(b).

4. CONCLUSION

In this study, quasi-monochromatic x-ray cone beam spectra generated using ultra-thick K-edge filtration were experimentally measured and compared to simulated scatter-free spectra under otherwise equivalent conditions. Pre-breast and post-breast spectra were acquired using various filter materials and under various operating conditions that mimic those seen clinically for 8-18cm thicknesses of uncompressed breast equivalent material. Agreement between measured and simulated data is overall excellent, leading to the conclusions that we can confidently simulate beam characteristics when trying to optimize our further, down-stream imaging simulations, and also that our non-traditional heavily filtered x-ray spectra are practicable for use in dedicated breast tomography (computed mammatomography or CmT). Indeed, these types of quasi-monochromatic beams, under different optimization conditions, might also be useful for other dedicated x-ray imaging approaches, such as breast tomosynthesis and small animal imaging. Comparisons of spectral FOMs generally showed quite a large improvement for ultra-thick filtered beams over spectra generated solely with intrinsic beam filtration. Using a rotating tungsten anode tube with high heat capacity, it has been possible to

implement such an ultra-thick filtration scheme in our lab without undue distress on the prototype CmT system [1,3,9,10]. One of the major advantages of using the filtration scheme is the reduction in absorbed dose to the breast of the patient in breast CmT. Other experimental studies have shown improvements in dose and exposure efficiency for the quasi-monochromatic cone-beam paradigm implemented here [9] and trends in absorbed dose highlighted in this study further corroborate those results. Further ongoing investigations are examining the possibility, with the aid of this quasi-monochromatic beam and other system features, of reducing cumulative dose to the breast for fully 3D computed mammotomography down to a fraction of that absorbed during dual-view mammography [10].

REFERENCES

1. M.P. Tornai, R.L. McKinley, C. N. Brzymialkiewicz, P. Madhav, S.J. Cutler, D.J. Crotty, J.E. Bowsher, E. Samei, C.E. Floyd. "Design and Development of a Fully-3D Dedicated X-ray Computed Mammotomography System." *Proc. SPIE: Physics of Medical Imaging*, **5745** (1), 189-197 (2005).
2. M.L. Bradshaw, R.L. McKinley, E. Samei, C.N. Archer, M.P. Tornai. "Initial X-ray Design Considerations for Application Specific Emission and Transmission Tomography (ASETT) of the Breast." *J. Nucl. Med.*, **44** (5), 287, (2003).
3. R.L. McKinley, M.P. Tornai, E. Samei, M.L. Bradshaw. "Development of an Optimal X-ray Beam for Dual-Mode Emission and Transmission Mammotomography." *Nucl. Instr. Meth. Phys. Res.*, **A 527** (1-2), 102-109 (2004).
4. R.L. McKinley, M.P. Tornai, E. Samei, M.L. Bradshaw. "Simulation Study of a Quasi-Monochromatic Beam for X-ray Computed Tomography." *Med. Phys.* **31** (4), 800-813 (2004).
5. G.R. Hammerstein, D.W. Miller, D.R. White, M.E. Masterson, H.Q. Woodard, J.S. Laughlin. "Absorbed radiation dose in mammography". *Radiology*. **130**, 485-491 (1979).
6. K. Maeda, M. Matsumoto, A. Taniguchi. "Compton-Scattering Measurement of Diagnostic X-ray Spectrum Using a High-Resolution Schottky CdTe Detector". *Med. Phys.* **32** (6), 1542-1547, (2005).
7. J. Boone. UC Davis Medical Center, Sacramento, CA (private correspondence).
8. B. De Man, J. Nuyts, P. Dupont, G. Marchal, P. Suetens. "An Iterative Maximum-Likelihood Polychromatic Algorithm for CT". *IEEE Trans. Med. Imaging*, **20** (10), 999-1008, (2001).
9. M.P. Tornai, R.L. McKinley, E. Samei, C.E. Floyd, M.L. Bradshaw. "Effects of Uncompressed Breast Composition and Thickness on Image Quality Using a Quasi-Monochromatic Beam for X-ray Computed Mammotomography". *Proc. 7th Int. Workshop Digit. Mammography*, Dovetail Publishing, Inc. 46-55 (2005).
10. R.L. McKinley, M.P. Tornai. "Preliminary Investigation of Dose for a Dedicated Mammotomography System." Presented at the *2006 SPIE Medical Imaging Conference*, 11-17 Feb. 2006, San Diego, CA, and to be published in *Proc. SPIE: Physics of Medical Imaging* (2006).